8-19-2013 12:00 AM

Numerical Modeling of Solidification Process and Prediction of Mechanical Properties in Magnesium Alloys

Mehdi Farrokhnejad
The University of Western Ontario

Supervisor
Anthony G. Straatman
The University of Western Ontario Joint Supervisor
Jeffrey T. Wood
The University of Western Ontario

Graduate Program in Mechanical and Materials Engineering
A thesis submitted in partial fulfillment of the requirements for the degree in Doctor of Philosophy

Recommended Citation

Farrokhnejad, Mehdi, "Numerical Modeling of Solidification Process and Prediction of Mechanical Properties in Magnesium Alloys" (2013). *Electronic Thesis and Dissertation Repository*. 1459.
https://ir.lib.uwo.ca/etd/1459

NUMERICAL MODELING OF SOLIDIFICATION PROCESS AND PREDICTION OF MECHANICAL PROPERTIES IN MAGNESIUM ALLOYS

(Thesis format: Integrated Article)

by

MEHDI FARROKHNEJAD

Graduate Program in Mechanical and Materials Engineering

A thesis submitted in partial fulfillment
of the requirements for the degree of
Doctor of Philosophy

The School of Graduate and Postdoctoral Studies
The University of Western Ontario
London, Ontario, Canada

Abstract

A formulation used to simulate the solidification process of magnesium alloys is developed based upon the volume averaged finite volume method on unstructured collocated grids. To derive equations, a non-zero volume fraction gradient has been considered and resulting additional terms are well reasoned. For discretization the most modern approximations for gradient and hessians are used and novelties outlined. Structure-properties correlations are incorporated into the in-house code and the proposed formulation is tested for a wedge-shaped magnesium alloy casting. While the results of this study show a good agreement with the previously reported experimental data, it was concluded that a better understanding of the boundary condition that existed during the experiment would result in a more agreeable result.

A variety of boundary conditions are considered at the mold-casting interface to replicate the existing conditions during the casting process. The predicted cooling rates and experimental correlations are used to predict the local grain size and average yield strength. The grain size and thickness of the skin and core regions are taken into account to modify the local yield strength. Results are compared to previously reported experimental data. The outcome of this comparison emphasizes the importance of the influence of cooling rate on the mechanical properties of castings. The effect of different boundary conditions, which resulted in variation of the cooling rates, various grain sizes and, hence, various yield strengths are studied and discussed.

It is concluded that the formulation and the numerical treatment presented in this work can be used as an excellent framework to capture the key features of the solidification process, and also provides sufficient microstructural information for estimating the local mechanical properties of die-cast components.

Keywords

Solidification modeling, Magnesium alloys, Phase change modeling, Wedge casting, Die-Casting modeling, Volume-Averaged technique, Finite Volume Method, Unstructured grid, Collocated grid.

Co-Authorship Statement

There are two journal papers included in this thesis work both of which the first author is the author of this thesis as well. The other two authors on these articles are the supervisors. The papers are constructed and written by the first author, however, the supervisors provided editorial and scientific support on the content of the papers.

Acknowledgments

I would like to express my deepest gratitude to my supervisors, Profs. A.G. Straatman and J.T. Wood, for the guidance provided throughout my research, their constructive criticism, many valuable suggestions and continuous support.

This project was partially funded by AUTO21 Network of Centers of Excellence, an automotive research and development program that focuses on issues relating to the auto industry in the 21st century, and Meridian Lightweight Technologies Inc. I would like to thank the aforementioned parties for providing educational and financial support.

Finally, I take the opportunity to thank my family and friends for their support and interest throughout this research. I am quite sure that I could not have brought this work to this degree of completion without their sustained encouragement.

Table of Contents

List of Tables

List of Figures

List of Appendices

Nomenclature

a	active coefficient in discretized equation
A	area,m^2
b	body force
Cp_k	specific heat of constituent *k*, J/KgK
d	grain size in Hall-Petch equation
f_k	volume fraction of constituent *k*
$\vec{g}$	gravity vector
h_k	sensible enthalpy of constituent *k*
h_{sl}	interfacial heat transfer coefficient, w/m^{2}K
k	Hall-Petch slope on a plot of true stress, σ , versus $d^{1/2}$
k_k	thermal conductivity of constituent *k* , w/mK
k_P	partition coefficient
$k_{eff,k}$	effective thermal conductivity of constituent *k,* w/m^{2}K
L_{ls}	latent heat of fusion, KJ/Kg
Le	Lewis number
m	iteration number
$\dot{m}'''_{jk}$	mass exchange of phase *k* at the *jk* interface
$\dot{m}$	mass flux, kg/s
$\hat{n}$	unit normal vector
R	cooling rate
R_{ip}	parameter for inverse distance interpolations
$\Delta\vec{R}_{ip}$	displacement vector from $\vec{x}_p + R_{ip}\vec{x}_{ip}$ to $\vec{x}_{ip}$
$\vec{s}$	displacement vector from *P* to *nb*
S'''	volumetric source term
t	time, s
t_s	local solidification time, s
T_{ref}	reference temperature, K
T_k	temperature of constituent *k*
T_{mlt}	melting temperature of alloy, K
T_{sol}	solidus temperature of alloy, K
T_{Eut}	eutectic temperature of alloy, K
T_{liq}	liquidus temperature of alloy, K
$\hat{\vec{u}}$	advecting velocity, m/s
$\tilde{\vec{u}}$	pseudo-velocity, m/s
$\vec{v}_k$	velocity vector of constituent *k*
$\vec{v}_I$	interfacial velocity, m/s

V_k	volume of constituent in REV
V	volume of REV
$\vec{x}$	position vector
$\langle\ \rangle$	denotes extrinsic volume average
$\langle\ \rangle^k$	denotes intrinsic volume average with respect to constituent *k*

Greek Symbols

σ	yield or flow strength
δ_t	skin thickness fraction
ω	parameter for inverse distance interpolations
α	weighting factor
β	volumetric thermal expansion, k^{-1}
μ	dynamic viscosity, kg/ms
$\partial\Omega_P$	denotes a surface bounding a control volume
Ω_P	denotes the dimension of a control volume
Γ	diffusion coefficient
$\sigma_\circ$	intercept stress
φ_k, ψ_k	generic field variable for constituent *k*
$\hat{\varphi}_k$	fluctuating component of the constituent field variable
γ	blending factor
κ	morphology factor
ρ_k	density of constituent, kg/m^3

Subscripts and Superscript

ip	quantity evaluated at or associated with an integration point
nb	quantity evaluated at or associated with a neighboring control volume
k	$k \in \left\{ l(liquid), s(solid), m(mixture) \right\}$
p	quantity evaluated at or associated with a particular control volume

Chapter 1

1 Introduction and Background

Automakers are concentrating on reducing car weight and limiting exhaust emissions due to legislative requirements for safer and cleaner vehicles. A 15% weight reduction improves fuel efficiency by at least 10%, reducing gasoline consumption by 10 billion gallons and saving $US27 billion/year at the current pump prices of $2.7/gal. Moreover, 10 billion gallons in fuel reduction would reduce CO_2 emissions by 200 billion lb[1].

Light metal alloys, particularly magnesium-aluminum (Mg-Al) alloys, due to their low density and excellent specific stiffness and strength, offer a significant reduction in mass compared with traditional metals. Advancements in the Canadian Mg-Al alloy die-casting technology industry would allow for a competitive global advantage in an increasingly fuel-efficient market.

High pressure die casting (HPDC), which is the most common process for the production of Mg-Al components, is prone to the development of defects such as knit lines and micropores that lead to the local degradation of mechanical properties. The non-equilibrium nature of rapid solidification that exists in HPDC makes the understanding and analysis of these processes extremely difficult. As a result, die-casters are constrained to design components assuming lower-than-actual mechanical properties which, in-turn, results in larger-than-necessary, heavier and more costly parts, limiting the use of Mg-Al alloys in the auto industry and decreasing their competitiveness. Enhancing control over the as-cast microstructure and reducing product development time by enabling realistic prediction of actual local microstructure and mechanical properties will allow for the optimization of section thickness for mass and cost reduction.

A research program funded by the AUTO21 Network of Centres of Excellence and Meridian Lightweight Technologies Inc. has, since its inception in 2001, been focused on filling the gaps in the process-structure-properties relationships for HPDC of commercial Mg alloys such as AM60B. Work-to-date has resulted in identification of the casting features that affect microstructural features as well as mechanical properties that are influenced by microstructural features. Via a combination of experiments and utilization of commercial software, structure-property and process-structure relationships that can be used to predict these behaviors have been developed [2-6].

Computational tools not only provide assistance for a faster understanding of the effect of variations of variables during the process but also shorten the prototyping sequence for newly developed alloys and improve the die designs. Although the most advanced existing industry-standard software, such as MAGMASOFT and ProCAST, are capable of predicting some of the features of the casting, they are not yet able to accurately predict all of them [7], hence, a high rate of scrap is still produced.

The work described in this thesis is focused on further developing the understanding of the solidification process, the prediction of microstructure, and the implementation of previously established structure-property relationships into an in-house numerical code beneficial to the Canadian magnesium die-cast industry. In particular, an advanced Computational Fluid Dynamics (CFD) code using a finite volume approach for the simulation of solidification of Mg-Al alloys, with novelties in the volume averaged formulation that led to a better prediction of cooling rates, and therefore, grain size and mechanical properties (yield strength), than those from existing commercial software is developed.

The remainder of this chapter is an overview and background of some of the concepts and terminologies that are not reviewed in the subsequent chapters but which are required to better understand the physics of the casting process.

1.1 Magnesium and Magnesium Alloys

Magnesium (Mg) with atomic number and weight of 12 and 24.32, respectively, and a density of about 1.7 g/cm^3, occupies a place in Group II of the Periodic Table and it may be referred to as the lightest of typical divalent metals. Pure magnesium is relatively weak and easy to deform. Typically, sand-cast pure magnesium has a tensile strength of approximately 90 MPa, yield strength of 21 MPa, and an elongation to fracture of approximately 2-12% [8]. Alloying can greatly improve the mechanical properties of magnesium.

AM60B or AZ91 and other aluminum-magnesium alloys, in which aluminum is the primary alloying element, show excellent properties such as low-density, high specific stiffness and strength, which makes them great candidates for making structural components in industries such as automotive where significant reduction in mass and manufacturing labour cost are critical.

Table 1 indicates how alloying increases the mechanical properties of pure magnesium without significantly increasing the density. For example, with only a 3.2% increase in the density of AM60B, 1.8 g/cm^3, compared to pure magnesium, there is an increase of 150% in tensile strength and an increase of about 520% in yield strength [8].

It is worth mentioning that in this particular alloy, in addition to Al, other elements such as Manganese (Mn), Zinc (Zn) and Silicon (Si) are added to the pure Mg to improve its corrosion resistance, strength at room temperature and creep resistance, respectively [9,10]. Copper also can be found as an impurity in the AM60B alloy and should be eliminated due to its negative influence on mechanical strength and corrosion resistance [3].

Table 1-1: The effect of Aluminum on the mechanical properties of Mg [2]

Metal or Alloy	% Aluminum	Ultimate Tensile Strength (MPa)	Yield Strength (MPa)	Elongation to fracture (%)
Pure Mg	0	90	21	12
AM60B	5.5-6.5	225	130	8
AZ91	8.3-9.7	240	160	3

1.2 Terminologies and Fundamentals

A solid or liquid *phase* refers to a portion of the system where the properties and composition of the material are homogeneous and which is physically distinct from other parts of the system. Liquids take the shape of their container and are essentially incompressible, whereas solids retain their original shape unless an external force deforms them. A *crystalline material* is one in which the atoms are located in a repeating or periodic array over large atomic distance. *Lattice* is a term used in the context of crystal structure and it means a three dimensional array of points coinciding with atom positions. In the crystal structure, small groups of atoms form a repetitive pattern, which are called *unit cells* [11]. Magnesium crystalizes in the hexagonal close packed (h.c.p) structure, Fig. 1-1. However, the axial ratio, c/a =1.6236, does not exactly correspond with the close packing of spheres, for which it is 1.633 [12].

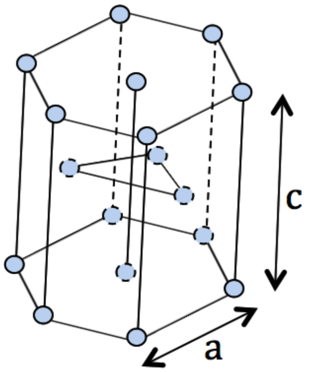

Figure 1-1: The hexagonal close-packed crystal structure

Point defects are where an atom is missing or is in an irregular place in the lattice structure. *Diffusion*, which is the phenomenon of material transport by atomic motion, occurs when there is a point defect in the solid structure and the atom has sufficient energy to break bonds with its neighbouring atoms and cause lattice distortion. Diffusion flux is defined as the mass or number of atoms diffusing through and perpendicular to a unit cross-sectional area of solid per unit of time. Fick’s second law is used to predict how diffusion causes the concentration to change with time:

$$\frac{\partial C}{\partial t} = \frac{\partial}{\partial x}\left(D\frac{\partial C}{\partial x}\right) \tag{1-1}$$

where C is the concentration and D is called the diffusion coefficient. The magnitude of the diffusion coefficient is indicative of the rate at which atoms diffuse. This coefficient is highly influenced by temperature and increases exponentially with increasing temperature. The solution to Fick's second law for specific boundary conditions is available in literature [11]. For a semi-infinite solid in which the surface concentration is held constant one can obtain a solution as follows:

$$\frac{C_x - C\big|_{t=0}}{C\big|_{t>0}^{Surface} - C\big|_{t=0}} = 1 - erf\left(\frac{x}{2\sqrt{Dt}}\right) \tag{1-2}$$

where C_x represents concentration at depth x after time t. $erf(x/2\sqrt{Dt})$ is the Gaussian error function, values of which are available in mathematical tables for various $x/2\sqrt{Dt}$ values. This solution is demonstrating that the concentration at any depth is a function of $x/\sqrt{Dt}$ and can be determined at any time and position if a correct boundary condition is available [11]. Also, it is stating that diffusion takes time, meaning that if there is insufficient time for diffusion, the distance over which diffusion can happen reduces accordingly.

1.3 Diffusion Length Scale

Diffusion length scale is defined by square root of product of solidification time and diffusivity. It is a measure of the distance over which a property of interest can propagate. Most of metallic systems have a thermal diffusivity, α, of the order of 10^{-6} to 10^{-5}. For the sake of discussion let's assume that $\alpha_s = \alpha_l = 10^{-5}[\frac{m^2}{s}]$.

Table 1-2: Shows diffusion length scale for different cooling rates

Length of Diffusion	**R=1000K/s**	**R=1K/s**
Heat	1.34 mm	42 mm
Solute in solid	0.134 μm	4.2 μm
Solute in liquid	13.4 μm	420 μm

Also the diffusion coefficient for the similar systems can be approximated in the order of $D_s \approx 10^{-13}$ and $D_l \approx 10^{-9} [m^2 / s]$. Knowing that the solidification time is defined as the ratio of the freezing range and cooling rate, one can measure how much heat or solute propagates into a material based on the existing cooling rate in the process of casting. For example, for a cooling rate between 1K/s and 1000 K/s and a freezing range of 180 K the data shown in Table 1-1 can be obtained. While these numbers should be compared to the length scales present in the solidification process, in general, it can be said that heat propagates faster than solute, and also, solute diffusion in the liquid is often complete compared to the solid for the low cooling rates.

1.4 Driving Force for Solidification

The study of phase transformation involves how one or more phases in the system of study, i.e. an alloy, change into a new phase or mixture of phases. The main reason why the transformation occurs is because the initial state of the alloy is unstable relative to the final state. The measurement of the relative stability of a system at constant temperature and pressure is determined by the Gibbs free energy (G) and is defined as [13]:

$$G = H - TS \tag{1-3}$$

where T is the absolute temperature, S is the entropy and H is the enthalpy of the system. Enthalpy is a measure of the heat content of the system and is defined as:

$$H = U + PV \tag{1-4}$$

where U is the internal energy, P is the pressure and V is the volume of the system. The internal energy of the system is the total kinetic and potential energies of the atoms within the system. If a transformation occurs, the heat that is absorbed or evolved will depend on the internal energy of the system and changes in the volume of the system. The term PV for solid and liquids does not change significantly compared to U and this means that $H \approx U$ [13].

From thermodynamics it is well known that for a closed system that is at constant temperature and pressure, the system will be in stable equilibrium if it has the lowest possible value of Gibbs free energy, i.e. $dG=0$. From Eq. (1-3), the highest stability would be achieved with the best compromise between low enthalpy and high entropy. This means that at low temperatures, solids are the most stable due to the fact that they have the strongest atomic bonding and the lowest internal energy. At higher temperatures, on the other hand, the entropy of the system is higher for liquids and gases due to the fact that atoms have more freedom for movement, thus the term $-TS$ in Eq. (1-3) dominates and makes these phases most stable. Any transformation that results in a decrease in Gibbs free energy is possible, therefore, a necessary criterion for a solidification process is that the difference between the free energies of the initial and final states must be negative [13].

Now, if a liquid metal is undercooled by ΔT below its melting temperature, T_m, solidification will be accompanied by a decrease in Gibbs free energy. This decrease provides the driving force for solidification process that can be obtained as below:

At temperature T:

$$\Delta G = \Delta H - T\Delta S \tag{1-5}$$

where $\Delta H = H^{Liquid} - H^{solid}$ and $\Delta S = S^{Liquid} - S^{solid}$. At the equilibrium melting temperature the free energies of solid and liquid are equal so Eq. (1-5) is zero, therefore:

$$\Delta S = \frac{\Delta H}{T_m} = \frac{L}{T_m} \tag{1-6}$$

If we substitute Eq. (1-6) into Eq. (1-5), for small undercooling [13]:

$$\Delta G \approx \frac{L\Delta T}{T_m} \tag{1-7}$$

1.4.1 Thermal and Constitutional Undercooling

The concepts of thermal and constitutional undercooling can be understood the best when they are defined together. The contribution of thermal undercooling and constitutional undercooling toward the solidification process is an increase in the free energy of the system.

If the growth of the solid lags the heat transport out of the liquid, then thermal undercooling occurs. The amount of undercooling is the amount liquid is under the equilibrium temperature or liquidus temperature: $\Delta T_T^{bulk} = T_{liq} - T_{bulk}$

One must note that to measure the thermal undercooling at the interface, the rejection of latent heat at the interface must also be considered. Using Eq. (1-6) and Eq. (1-7), the corresponding increase in free energy due to the thermal undercooling at the interface could be measured as:

$$\Delta G_T = \Delta S \times (T^* - T_{bulk}) \qquad (1\text{-}8)$$

in which T^* is the temperature at the solid/liquid interface.

When alloys solidify, if their partition coefficient is less than one, solute atoms are rejected from the first region to solidify into the liquid and build up just ahead of the solid/liquid interface, forming a boundary layer, δ, which has a higher content of solute than that of the bulk liquid, Fig. (1-2).

If the heat diffusion is considered to be complete and the solute diffusion in the solid is neglected, using an interfacial species balance results in an estimate of the thickness of the concentration boundary layer:

$$\underbrace{D_s \frac{\partial C_s}{\partial x}\Big|^*}_{0} - D_l \frac{\partial C_l}{\partial x}\Big|^* = (C_l^* - C_s^*) v^* \Rightarrow \delta = \frac{D_l}{v^*} \qquad (1\text{-}9)$$

In which v^* is the velocity of the interface and all the values with asterisks are evaluated at the solid/liquid interface. Higher interface velocities will result in a steeper solute gradient at the interface.

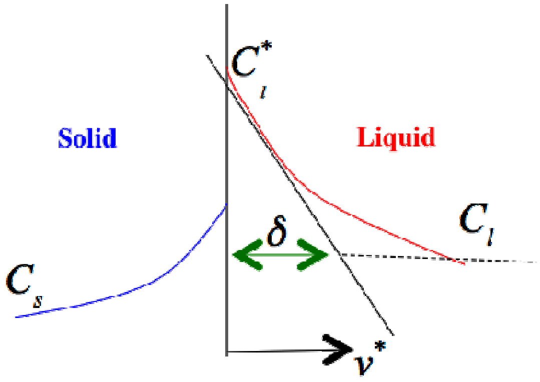

Figure 1-2: Shows the solute pile-up in front of the interface

This difference between the solid and liquid solubility of the alloying element is responsible for the additional undercooling that is called the constitutional undercooling.

The concept of constitutional undercooling can be explained using the phase diagram. Consider an alloy with a nominal composition of C_0. At the solidus temperature the composition of solid is C_0, while the composition of liquid is C_0/k_p, Fig. (1-3). Due to the higher concentration of the liquid at the interface compared to that further away from the interface, the concentration boundary layer forms [14,15].

As a consequence of the variation of the composition, from C_0/k_p at the interface (at solidus temperature) to C_0 in the bulk liquid (at liquidus temperature), a temperature boundary layer forms that states that the liquidus temperature is varying from solidus temperature at the interface to the nominal liquidus temperature in the bulk. Fig. (1-4)

If the temperature gradient resulting from the temperature field, $T(x)$, in the liquid is less than the one from $T_{liq}(x)$, then the liquid will be at a temperature lower than T_{liq}, the yellow region in Fig. (1-4). This is where the liquid is undercooled, meaning that the liquid has a lower temperature than the liquidus temperature but still has the liquid state.

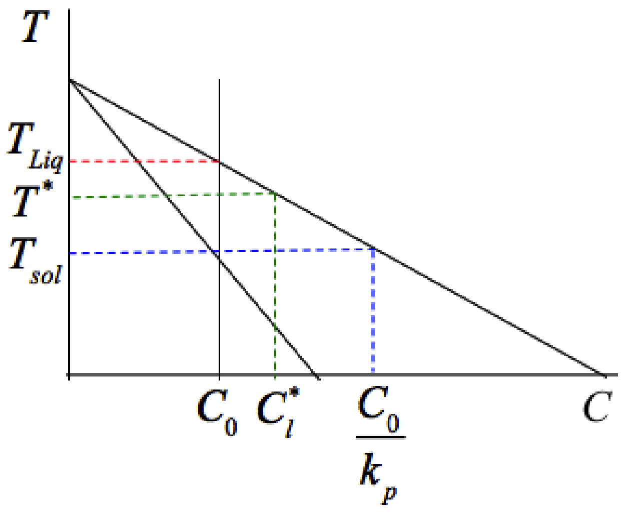

Figure 1-3: Schematic of a portion of a phase diagran

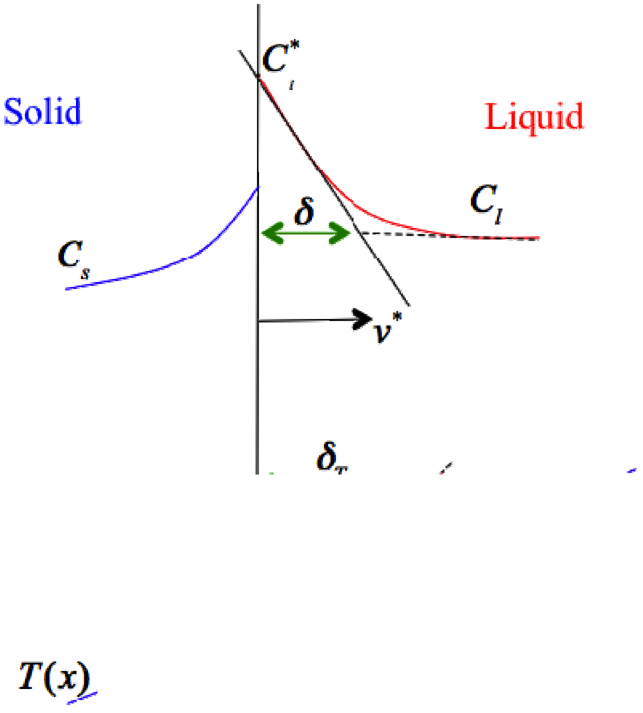

Figure 1-4: The thermal and solutal field in front of solid/liqui

The corresponding increase in the free energy due to the constitutional u be calculated as:

$$\Delta G_C = \Delta S \times (T_L - T^*) = \Delta S \times m(C_l^* - C_0)$$

1.5 Nucleation

If the molten metal is cooled below the melting temperature, there is a driving force for solidification, ΔG, and it might be expected that the liquid phase would solidify immediately, however, this might not always be the case. For example, under special conditions, liquid nickel can be undercooled to about 250 K below its melting temperature and held at this temperature without any phase change occurring. The absence of very small particles or *nuclei* is the reason that this happens [13].

The nucleation process occurs when the probability of atoms arranging themselves on a crystal lattice is high enough to form a solid crystal from the liquid. If there are no impurities in the liquid to assist nucleation and the solidification process initiated by undercooling alone, then the process of nucleation is called homogeneous. Heterogeneous nucleation occurs when nucleation sites such as walls of the mold or impurities exist to initiate crystal growth.

In homogeneous nucleation, if we assume that for a given volume of liquid at temperature ΔT below the melting temperature and free energy of $G_1 = (V_s + V_L)G_v^l$, some of the atoms of the liquid cluster together to form a small sphere of solid, then the free energy of the system will change into [14]:

$$G_2 = \gamma_{sl} A_{sl} + G_v^s V_s + G_v^l V_l \tag{1-11}$$

where A_{sl} is the solid/liquid interfacial area and γ_{sl} is the specific interface energy. So the formation of solid results in a free energy change of:

$$\Delta G = \gamma_{sl} A_{sl} - V_s (G_v^l - G_v^s) = \gamma_{sl} A_{sl} - V \Delta G_v \tag{1-12}$$

where ΔG_v can be calculated using Eq. (1-7). Eq. (1-12) states that the decrease in the Gibbs free energy due to the phase change balances the work required to keep the initial crystal bonds in the lattice structure from melting back to the liquid plus the change in the Gibbs free energy in changing from the liquid to solid phases. Below the melting temperature, ΔG_v is positive due to the lower free energy of a bulk solid and, therefore, the second term has a negative contribution to Eq. (1-12). However, the formation of solid/liquid interface has a positive contribution and it is the combination of these two terms that dictates whether the solid forms or not.

Assuming that the radius of the solid sphere is *r*, then [14]:

$$\Delta G_r = \gamma_{sl}(4\pi r^2) - \frac{4}{3}\pi r^3 \Delta G_v \tag{1-13}$$

Eq. (1-13) shows that the interfacial term increases as r^2 whereas the volume free energy released increases as r^3. This means that the creation of solid particles always leads to a free energy increase. Differentiating Eq. (1-13) gives a critical radius, r^*, below which the system can lower its free energy by dissolution of the solid and above which the free energy of the system decreases if the solid grows. The unstable solid spheres with radii below the critical radius are called embryo whereas the stable particles are referred to as nuclei [13,14].

If somehow the interfacial energy is reduced, it will be easier for nucleation to occur at smaller undercooling. A simple way of achieving this is if a nucleus forms in contact with the mold wall. It can be shown that the activation energy barrier against heterogeneous nucleation is smaller than that in the case of homogeneous nucleation [13,14].

1.5.1 Crystals and Grains

The crystallization of a large amount of material from a single point of nucleation results in a single crystal. In engineering materials, single crystals are produced only under carefully controlled conditions. The expense of producing single crystal materials is only necessary for special applications, such as turbine engine blades, solar cells, and piezoelectric materials. Normally, when a material begins to solidify, multiple crystals begin to grow in the liquid and a polycrystalline (more than one crystal) solid forms.

At the solidification temperature, atoms of the liquid begin to bond together at the nucleation points and start to form crystals. The final sizes of the individual crystals depend on the number of nucleation points. The crystals increase in size by the progressive addition of atoms and grow until they impinge upon adjacent growing crystals [13-15].

A crystal is usually referred to as a grain in engineering materials. A grain is simply a crystal without smooth faces because its growth is impeded by contact with another grain or a boundary surface. The interface formed between grains is called a grain boundary. The atoms between the grains (at the grain boundaries) have no crystalline structure and are called disordered [13-15].

1.5.2 Dendrites

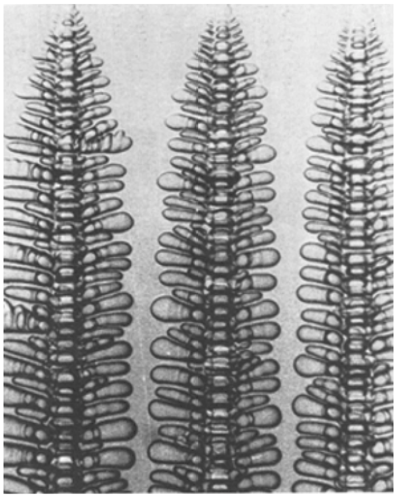

Figure 1-5: Dendritic structure [16]

The shape and size of crystallized grains depend on the conditions of their growth during solidification, mainly on the rate and direction of heat removal, the temperature of molten metal and the concentration of impurities. In most metals, the crystals that form in the liquid during freezing generally follow a pattern consisting of a main branch with many appendages. A crystal with this morphology slightly resembles a pine tree and is called a dendrite, which means branching. It has been established that crystals grow with the highest rate along the planes and directions where the atoms are packed most closely. Thus, long branches grow first, which are called the first-order dendritic axes. Then

secondary dendrite arms branch off the primary arm, and tertiary arms of
arms, etc.

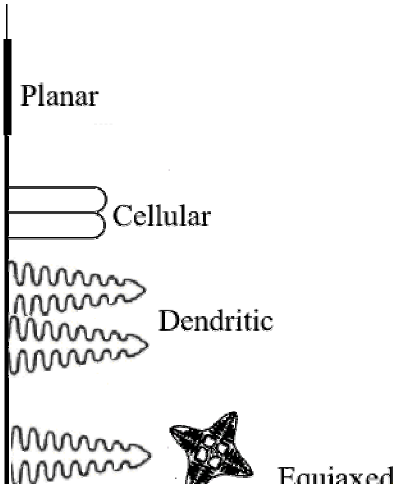

Figure 1-6: Transition from planar to dendrite

The possibility of the dendrite structure formation can be explained by st
of the planar interface. Interface instability can be promoted by the evolu
compositional field ahead of the growing interface. If the region is not ur
interface remains planar [13-15]. However, when the liquid is to a small
constitutionally undercooled, instabilities growing in this region will bec
because they will find themselves at a temperature lower than their equili
temperature; so they will grow and will only grow in the direction of soli
this small constitutional undercooling a cellular interface forms, Fig. (1-

As the constitutional undercooling increases, the spacing between cells i
constitutional undercooling may happen in the direction perpendicular to
directions. Instabilities will develop on the sides of these cells and this is
transition from cellular to dendritic solidification happens. Cellular and
that occurs from a wall in the direction opposite to the heat transfer is cal

growth. For higher constitutional undercooling, equiaxed grains grow further from the interface Fig. (1-6).

During solidification of a polycrystalline material, many dendritic crystals form and grow until they eventually become large enough to impinge upon each other. Eventually, the inter-dendritic spaces between the dendrite arms crystallize to yield a more regular crystal. If there is not enough liquid material to fill these spaces, some crystals may retain the dendritic shape. The original dendritic pattern may not be apparent when examining the microstructure of a material. However, dendrites can often be seen in solidification voids that occur in castings. It is worth mentioning that the region where there is a mixture of solid dendrites and interdendritic liquid is called mushy region. This region is where solidification happens and the microstructure forms.

1.6 Equilibrium and Nonequilibrium Cooling

Rapid solidification can be defined as the rapid extraction of thermal energy to include both superheat and latent heat during the transition from liquid at high temperature to solid at room temperature. A cooling rate of about 10^3 K/s and higher is considered a rapid solidification. Before commencing the solidification process, the rapid extraction of heat can cause undercooling as high as 100 ^{o} C or more, compared to about 10 ^{o}C or less in a conventional casting process, which promotes for the occurrence of several metastable effects that can be categorized as being microstructural [17].

In equilibrium cooling or solidification with slow change of temperature there is appropriate readjustment between liquid and solid composition based on the equilibrium phase diagram. These adjustments are done by the diffusion process, that is diffusion in both solid and liquid phase and across their interface [11]. It was shown in the preceding section, 1.2, that diffusion is a time-dependent phenomenon and the diffusion coefficient is also strongly dependent on the temperature. In particular, for solids, the diffusion coefficient or diffusion rate is low and decreases even more by lowering the temperature.

Consider the Mg-Al phase diagram depicted in Fig. (1-7). Most commercial Mg alloys, including AM60B, are in the hypoeutectoid region, where they solidify with a primary

$\alpha - Mg$ phase. Consider an AM60B in which nominal 6wt% Al exists. If the alloy is slowly cooled down from a temperature above liquidus temperature along the path that is shown by the vertical dashed line on the phase diagram, the alloy remains liquid, point a, and of composition 6wt% Al until the temperature reaches the liquidus line at about 892K (619 ^{0}C).

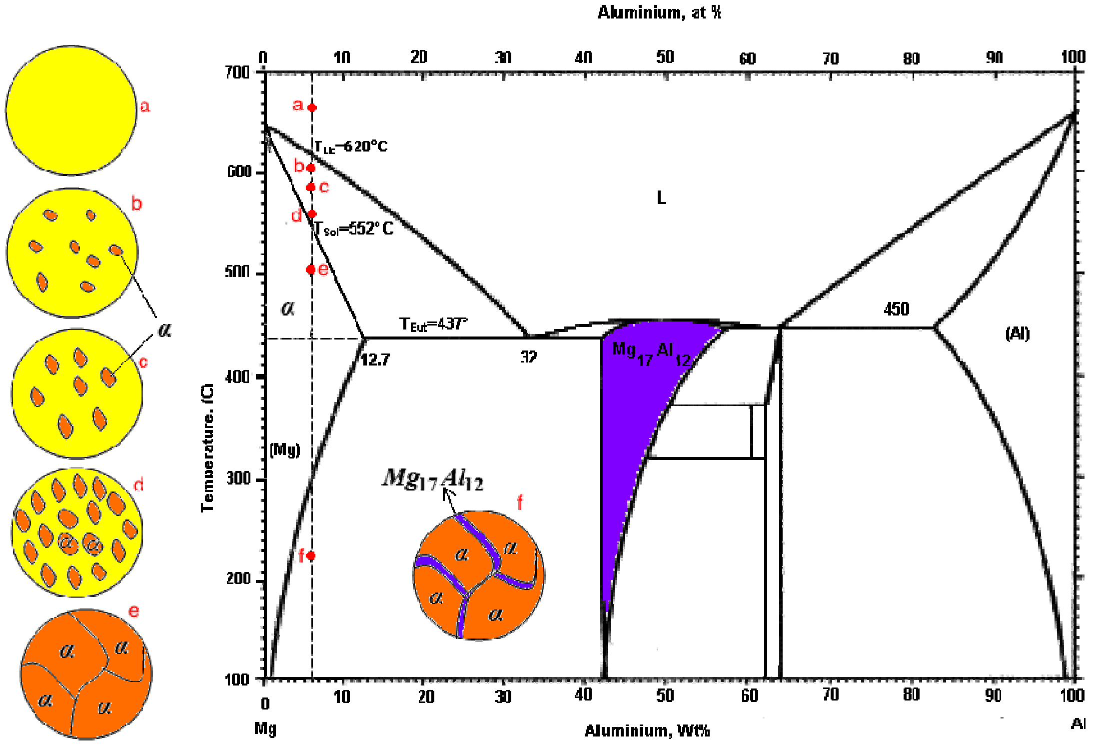

Figure 1-7: Magnesium-Aluminum phase diagram. The dashed line represents the equilibrium cooling and corresponding microstructures for 6wt% Al.

It is at this temperature when the solid $\alpha - Mg$ begins to form, point b. As we are passing the $\alpha + L$region more $\alpha - Mg$ forms, point c. The composition of the liquid and solid phase can be obtained by following the solidus and liquidus line on the phase diagram. Solidification reaches completion at the point where we cross the solidus line, point e. Once we pass the solvus line, point f, due to the fact that $\Delta G$is lower at the grain boundaries than any other locations in the formed grains, it is more favourable for intermetallic $\beta - phase$ ($Mg_{17}Al_{12}$) to grow on the grain boundaries through heterogeneous nucleation. $Mg_{17}Al_{12}$ is very brittle and the amount of it that is present in the microstructure depends on the cooling rate of the casting and the wt% of aluminum present.

When a high cooling rate is applied, however, microstructures are different from the equilibrium. For the purpose of simplification, consider the same alloy as discussed above, i.e. AM60B, that cools rapidly along the dashed line showed in Fig. (1-8). Also, it is assumed that diffusion rates in liquid phase are fast enough that equilibrium is reached. Following the vertical dashed line, again no changes occur while we are at the liquid region. Once we pass the liquidus line the $\alpha - Mg$ particles start growing, point a. Upon further cooling, point b in Fig (1-8), if the tie line is constructed, the liquid composition will be what it was expected, however, since diffusion in the solid $\alpha - Mg$ is relatively slow, the $\alpha - Mg$ that is formed at this point has not changed its composition accordingly and it has still a composition of about 2wt% Al. The fact is the composition of $\alpha - Mg$ has continuously changed with radial position from about 2wt%Al at grain centre to about 3wt%Al at the outer grain perimeters. Therefore, at point b, the average composition of solid grains would be some volume weighted average composition, lying between 2-3wt% Al, i.e. about 2.5wt% Al. Once we reach point c, although the solidus line on the equilibrium phase diagram has been reached, due to the fact that large proportion of liquid still exists, the solidification is not complete. In fact the solidification is completed at point e. The result of this nonequilibrium phenomenon is that the solidus line on the phase diagram has shifted to lower contents of Al, the blue line on the phase diagram. This displacement would be smaller as the cooling rate is slower. Generally, the centre of each grain is rich in the high-melting element, Al, whereas the concentration of the low melting element, Mg, increases with position from this region to the grain boundaries. This is termed *cored* structure, which causes the material to have less than optimal properties.

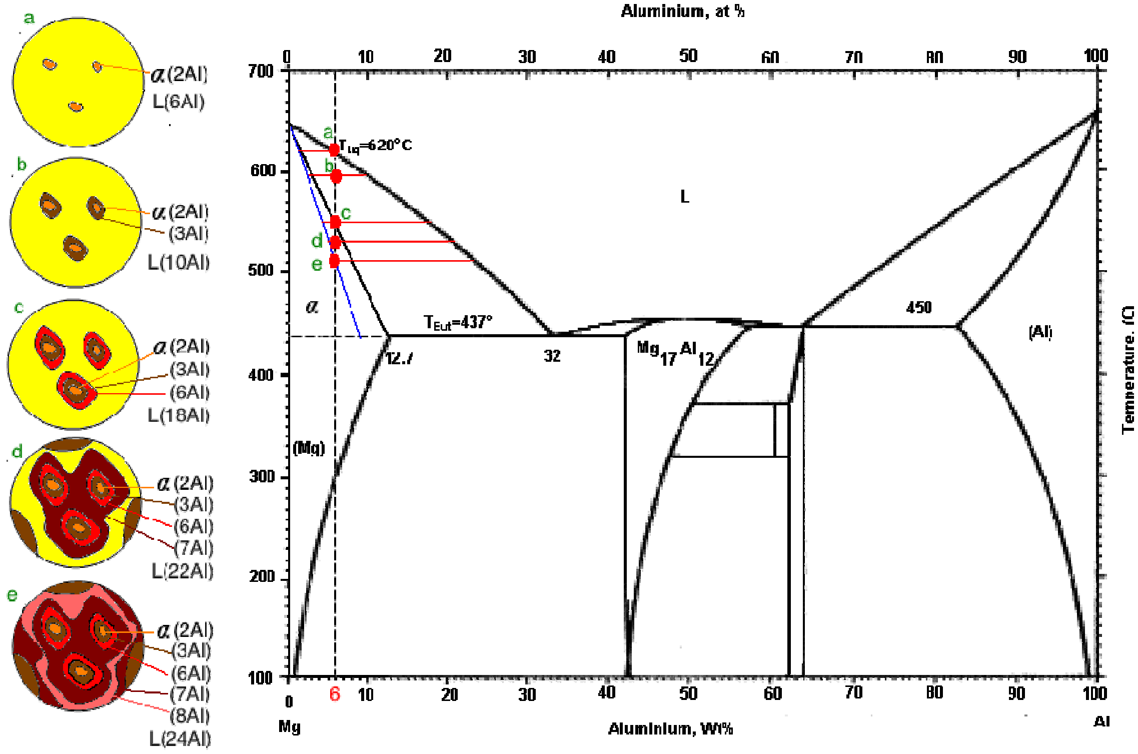

Figure 1-8: Magnesium-Aluminum phase diagram. The dashed line represents the solidus line displacement due to the nonequilibrium cooling and corresponding microstructures for 6wt% Al

1.6.1 Scheil's Equation

Scheil's equation describes the solute redistribution during nonequilibrium solidification process to some extent. In derivation of this equation no diffusion in solid and perfect mixing in the liquid is allowed. A local equilibrium at the solid/liquid interface is assumed, which allows the use of equilibrium phase diagram.

Writing a solute balance over a unit cell that is a closed system results in [18]:

$$\int_0^{x^*} C_s(x,t)\,dx + \int_{x^*}^{\lambda} C_l(x,t)\,dx = C_0 \tag{1-14}$$

where x^* is the location of the solid/liquid interface and λ is half of the space between idealized repeating dendrite arms, Fig. (1-9).

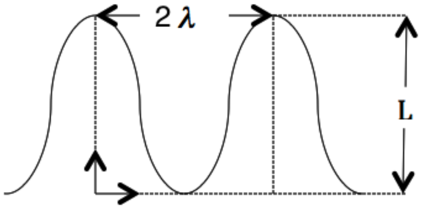

Figure 1-9:An idealized segment, displaying a periodic arrangement of dendrite arms

Because the liquid composition is uniform in space and is equal to the composition of the interface, then the second term on the L.H.S of Eq. (1-14) can be evaluated:

$$\int_0^{x*} C_s(x,t)\,dx + (\lambda - x^*)C_l^* = C_0 \tag{1-15}$$

Differentiating Eq. (1-12) with respect to time and setting the $C_s = C_s^*$, then:

$$C_s^* \frac{dx^*}{dt} + \int_0^{x*} \frac{\partial C_s}{\partial t} dx + (\lambda - x^*)\frac{dC_l^*}{dt} - C_l^* \frac{dx^*}{dt} = 0 \tag{1-16}$$

Using Eq. (1-1) and imposing the thermodynamic equilibrium at the interface, $C_s^* = k_0 C_l^*$, then:

$$-(1-k_0)C_l^* \frac{dx^*}{dt} + \int_0^{x*} D_s \frac{\partial^2 C_s}{\partial x^2} dx + (\lambda - x^*)\frac{dC_l^*}{dt} = 0 \tag{1-17}$$

For the assumed idealized shape a symmetry boundary condition can be imposed at x=0, i.e. $\frac{\partial C_s}{\partial x} = 0$:

$$-(1-k_0)C_l^* \frac{dx^*}{dt} + D_s \frac{\partial C_s}{\partial x} + (\lambda - x^*)\frac{dC_l^*}{dt} = 0 \tag{1-18}$$

Knowing that the solid fraction, f_s, is x^* / λ and considering the zero solid diffusion then:

$$-(1-k_0)C_l^*\frac{df_s}{dt}+(1-f_s)\frac{dC_l^*}{dt}=0 \tag{1-19}$$

Eq. (1-19) is stating that the solute rejected by the moving interface in time *dt* is equal to the increase of solute content in the liquid. As it is shown in Fig. (1-10) as solute is partitioned into the liquid, concentration of liquid rises to C_l^*. Also, C_s rises to C_s^* because the new solid is forming from a more concentrated liquid.

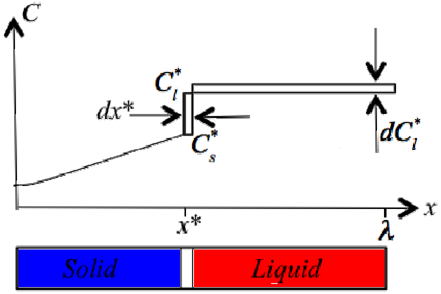

Figure 1-10: Schematic showing the partitioning of solute from the interface to the liquid

Further rearrangement of Eq. (1-19) and considering $C_l^*=C_0$ then the Gulliver-Scheil equation can be written as:

$$C_l^*=C_0 f_l^{k_0-1} \tag{1-20}$$

As it will be seen it is convenient to have the liquid fraction in terms of temperature. If it is assumed that on the phase diagram the liquidus curve is a straight line that is defined by $T=T_m+m_l C_l^*$, then:

$$f_s=1-\left(\frac{T-T_{mlt}}{T_{liq}-T_{mlt}}\right) \tag{1-21}$$

In this work, Eq. (1-21) is used to update the value of solid fraction in the energy equation. It is worth mentioning that an equilibrium assumption would result in deriving the equilibrium *Lever rule*.

1.7 Global Equilibrium Versus Local Equilibrium

From thermodynamics, Eq. (1-7), it is known that undercooling is necessary for solidification to occur. It is the amount of undercooling that dictates the degree of departure from equilibrium. As the solidification velocity increases, the solid-liquid transformation changes from fully diffusional to non-diffusional. Global equilibrium requires uniform composition and temperature across the system and happens mostly over geological time. The equilibrium phase diagram and Lever rule provides all information about the composition of solid and liquid, etc. For cases where the solidification velocity does not exceed the diffusive speed, local interface equilibrium and as a result the phase diagram is used to evaluate the composition and temperature at only the solid / liquid interface. This means that gradient of pressure, temperature and composition can exist in the interior of the phases and to evaluate field variables thermal, solutal and flow equations must be solved [19].

1.8 Casting of Mg alloys

1.8.1 Sand Casting

Casting, particularly sand casting, is one of the most common ways for mass production of parts with complex shapes. The main components of a casting system are the mold and feeding system. The mold usually consists of two parts; the lower drag and the upper cope, Fig. 1-11. In a typical hand-molding operation, the cope case is inverted over the drag part of the pattern, which is located on a flat surface. A sand mixture is poured over the pattern and pressed until it has sufficient strength so as to hold together after the pattern is removed. The mold cavity forms by subsequently separating the two mold halves. After the pattern has been removed, cores can be placed in this cavity to produce passages in the final cast product.

The feeding system is designed to introduce the liquid into the mold cavity with the minimum amount of turbulence as possible, so as to prevent incorporating surface oxides and other undesirable impurities into the casting. It mainly consists of a basin, down-sprue, runners, in-gates and risers. The basin is designed to absorb the impact of pouring and the metal is conducted to the level of mold cavity by the sprue. A set of runners and in-gates are included to feed the metal into the cavity. Risers are placed strategically on the casting to provide additional metal to feed the solidification shrinkage [20].

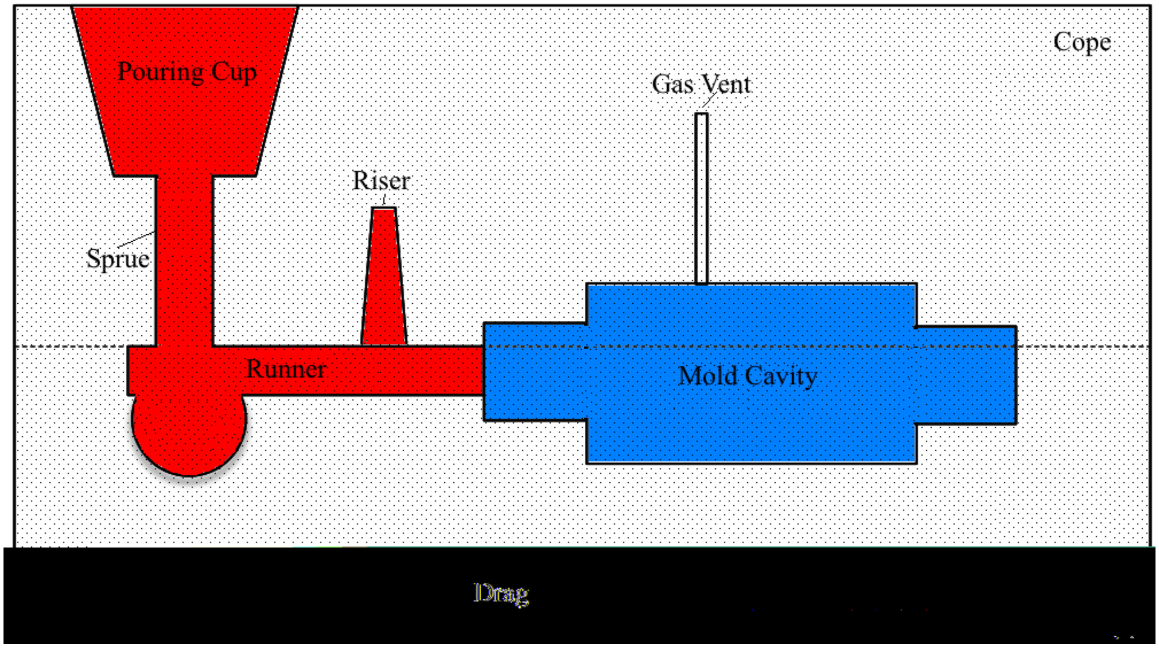

Figure 1-11: Schematic of a typical sand casting system

Mostly, in sand casting of pure metals and eutectic alloys, due to the fact that a smaller freezing range exists, a less restricted feeding channel forms and, hence, the head pressure in the sand casting is sufficient to lead the molten metal through the die.

Although the addition of aluminum to magnesium creates alloys with more attractive mechanical properties, it increases the freezing range of the alloy and subsequently the possibility of formation of higher-restricted feeding channels, which leads to a greater potential for porosity formation during die-casting operations [21]. Figure (1-12) shows that a wider freezing range of an alloy creates a more restricted feeding channel in which a higher pressure drop during the feeding process is experienced.

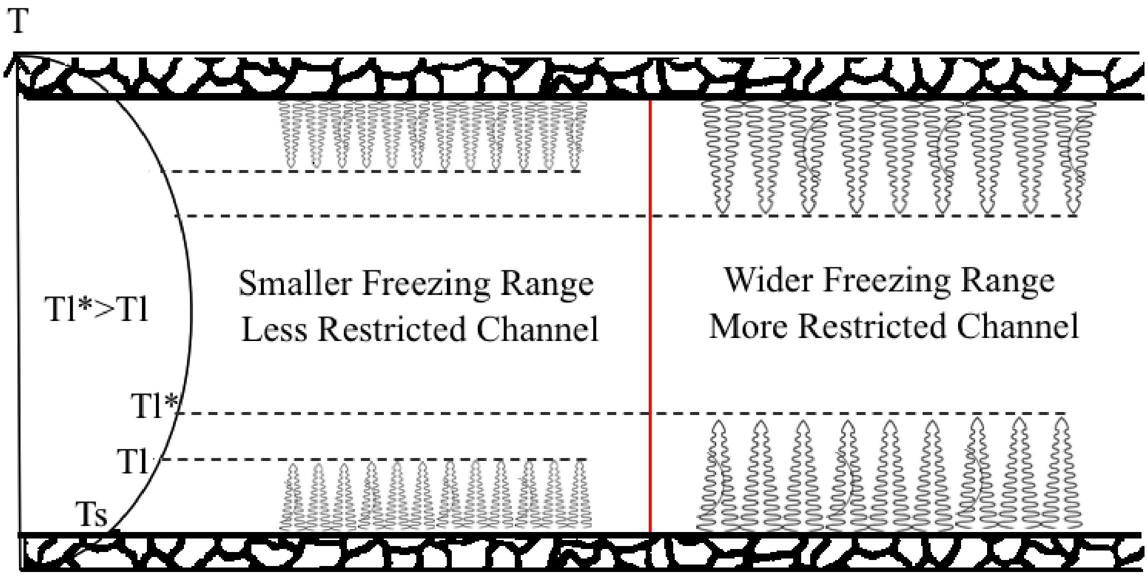

Figure 1-12: Schematic of the effect of freezing range on the casting process

Solidification shrinkage, which occurs from liquidus to solidus temperature, forms when these restricted feeding channels grow and the feeding liquids from the risers cannot compensate for it. The lack of proper feeding usually leads to a mass deficit and local shrinkage cavities and is one of the most important concerns for casting.

There are two other possible sources of porosity shrinkage that are not related to these restricted channels. Solid shrinkage, which occurs from solidus temperature to room temperature and is caused by the thermal expansion coefficient, could also cause a mass deficit that translates into shrinkage cavities. Also, liquid shrinkage, which occurs from the pouring temperature to the liquidus temperature, is compensated by the flow of liquid from the gating system and the risers and does not lead to considerable defects.

A High-Pressure Die-Casting (HPDC) is required to account for the more restricted channels for alloys further from eutectic. It is worth mentioning that due to the low density of Mg alloys, the metal velocity for a given pressure is considerably higher than for even aluminum alloys [21].

1.8.2 Die-Casting

In the die-casting process, parts of complex geometry are mass-produced to near net shape. Thin walls are a common feature of die-casting. Large cavity pressures of the order of 70 MPa are typically required to not only guarantee that the metal reaches the smallest features of the cavity but also to force metal into voids generated during the solidification process. Relatively short solidification times, of the order of 1 min or less, are usually observed in this type of casting. To prevent the solidification from impeding metal flow into the cavity of a die, a short fill time of up to a few hundredths of a second are required, which creates a turbulent flow regime at the gate [22].

In general there are two basic die-casting processes: Hot chamber and Cold chamber. The Hot chamber process is used for lower melting point metals such as Zinc, Lead etc. whereas Cold chamber is well suited for metals such as aluminum, brass and magnesium whose melting temperatures are fairly large. The process in Cold chamber machines start with melting the metal in a separate furnace. Then, a precise amount of molten metal is ladled manually or automatically into an unheated shot chamber after which the plunger advances to force the molten metal into the die cavity. In the Hot chamber, however, the plunger and cylinder are submerged in the molten metal in the holding furnace.

1.9 Porosity Defects

Development of defects appearing as porosity during the process of die-casting are mainly due to shrinkage and gas entrapment, which are also the two main reasons for the high scrap rate in Mg die-casting processes [15]. The presence of porosity strongly affects products' properties such as fracture toughness and fatigue and acts as crack initiation sites during the deformation process. In particular, several researchers have reported that the fracture of AM60B samples during tensile testing is strongly influenced by the amount of existing porosity in the samples [23-27].

The two main sources of gas porosity are the trapped gas and pre-existing suspended bubbles. These defects form during the filling process while the mold is being filled with molten liquid [15]. Figure (1-13) shows gas micropores that usually appear as round dark regions in the microstructure.

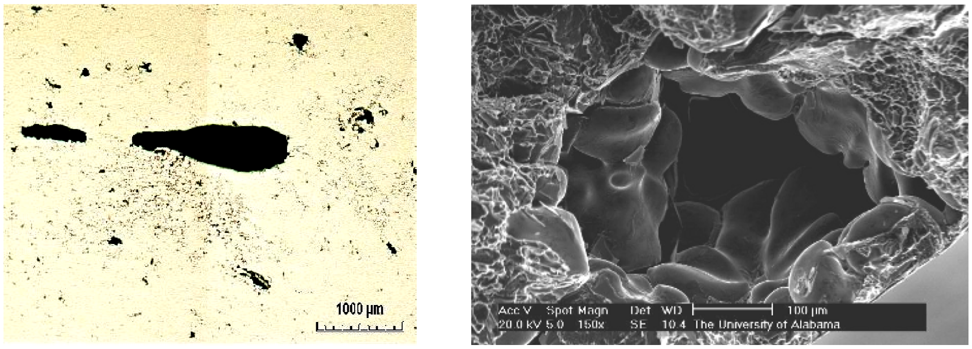

Figure 1-13: (Left) Appearance of gas porosity in a Mg alloy [28], (Right) SEM of a gas pore in unmodified Al-Si alloy [29]

Also, in general, there are two types of shrinkage defects; open shrinkage and closed shrinkage defects. Open shrinkage defects or macroshrinkage are usually driven by metal contraction and the atmospheric gases compensate the mass deficit produced by shrinkage. When they are open to the free surface, it is called *pipe shrinkage,* Fig. (1-14).

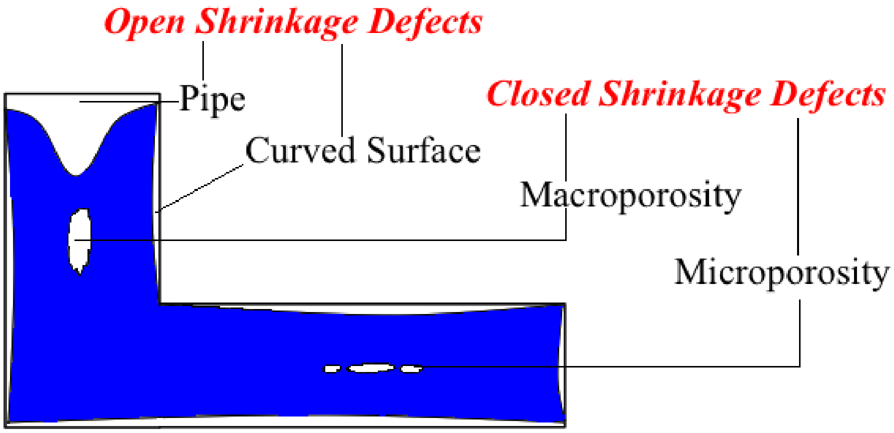

Figure 1-14; Types of shrinkage defects

Closed shrinkage, Fig. (1-14), is usually driven by metal contraction and pore nucleation. This shrinkage correlates with pore nucleation and growth in the mushy region and thus seems to depend on the impurity level and the amount of gas dissolved in the metal. This can exist as macroporosity or microporosity (microshrinkage) [15]. Microshrinkage takes the shape of interdendritic liquid, and pores are elongated [15, 30], Fig. (1-15).

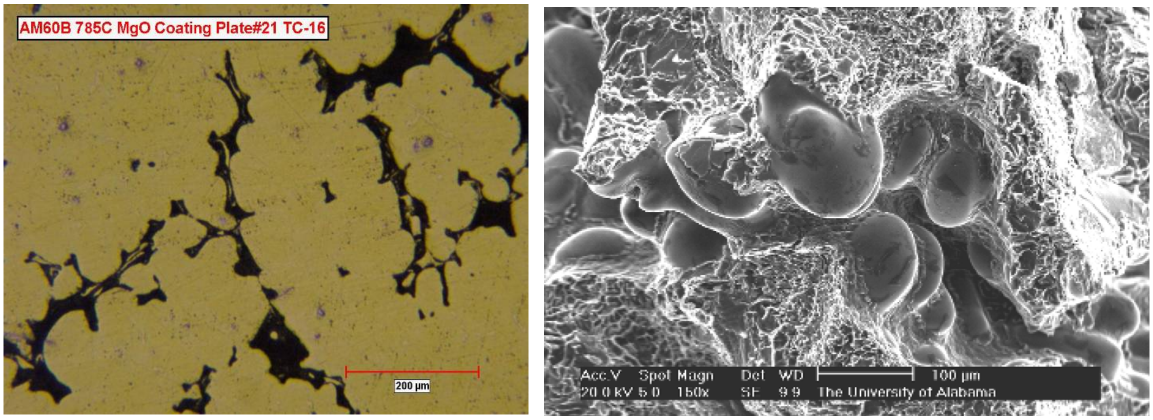

Figure 1-15: (Left) microshrinkage in a Mg alloy [28], (Right) SEM image of microshrinkage in Al-Si Alloy [29]

The current understanding of microporosity formation is that metal flows toward the region where shrinkage is occurring. When a gas pore appears in the mushy zone during the last stages of solidification, after dendrite coherency, it is entrapped in the dendritic network and more often at the root of dendrites. When the metal flow toward the solidification front is blocked, the pore becomes the starting point of microshrinkage. Thus, microshrinkage formation depends on the nucleation and growth of micro-pores, the formation of which can be understood from the analysis of the local pressure [15].

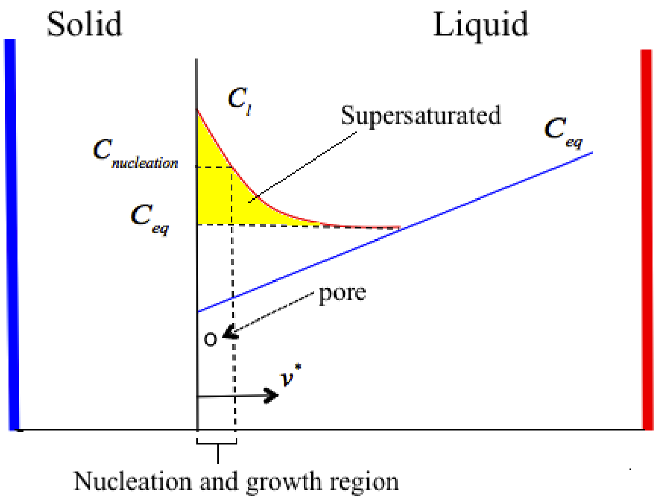

Figure 1-16: Pore formation mechanism

Pores follow the ideal gas law, meaning that at a certain temperature, the lower the pressure is, the bigger the pore volume can be. Sievert's law suggests that the solubility of a diatomic gas in metal is proportional to the square root of the partial pressure of the gas in thermodynamic equilibrium. i.e. $C_l \propto \sqrt{P_p}$ [31]. Also, solubility of gases in liquid metals decreases upon cooling them. Therefore, during solidification, the melt can become supersaturated in gases, consequently, gases can precipitate, and bubbles can grow, Fig. (1-16).

A pressure threshold for pore formation can be obtained by writing a balance equation between the pressure exerted by gas evolution and the sum of the local pressures in the mushy zone as well as induced pressure by the surface tension on the pore. If the gas pressure is larger than these pressures then a pore successfully forms:

$$P_{gas} \geq P_{mushy\ region} + P_{\gamma} \tag{1-22}$$

where P_{γ} is the pressure resulting from the surface energy of gas-liquid that must be overcome to have a gas-liquid interface and the local pressure of the mushy region can be decomposed into the following pressures, Fig. (1-17):

$$P_{mushy\ region} = P_{applied} + P_{metallostatic} - P_{shrinkage} \tag{1-23}$$

in which $P_{applied}$ is the pressure applied in die-casting or the atmospheric pressure, $P_{metallostatic}$ is the hydrostatic pressure due to the column of the metal, and $P_{Shrinkage}$ is the negative pressure from resistance to shrinkage induced flow through the dendrite network.

The pressure that a pore exerts to evolve, P_{gas}, and $P_{Shrinkage}$ are both in favour of pore formation whereas the others work against it.

It is difficult to control some of these pressures in a casting process. $P_{applied}$ can be controlled in a HPDC process and $P_{metallostatic}$ is almost negligible, however, controlling P_{γ} and $P_{Shrinkage}$ are almost impossible.

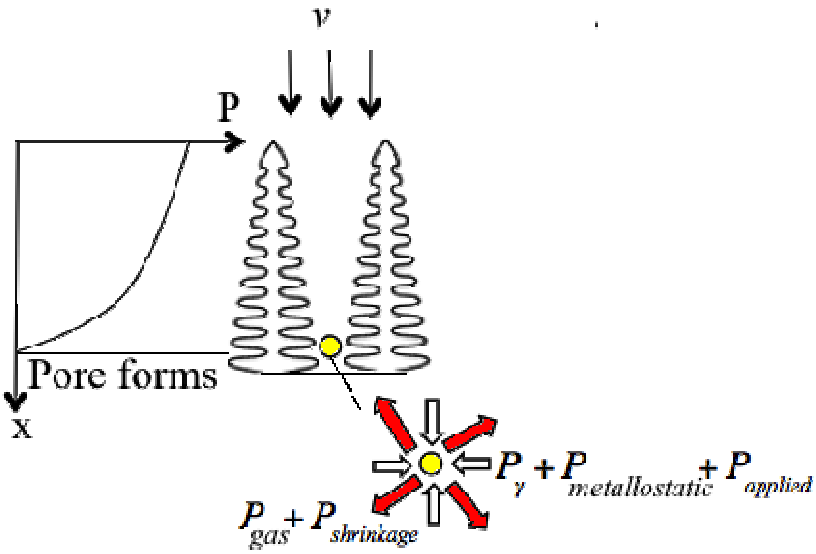

Figure 1-17: Pressure terms in favour of the pore formation versus terms against pore formation

1.10 Modeling of Casting Process

Modeling of the casting process involves the simulation of mold filling and solidification processes. Due to the absorption or release of latent heat and the presence of a complex interfacial structure that characterizes the phase change of most materials, exact solutions describing this process are not yet possible [32]. The metal flow, if considered, is treated as incompressible, although the density is generally temperature dependent. Since turbulence is experienced mostly during the mold filling process and the fluid flow for solidification is generally laminar, coupling these two processes is an arduous task.

The behaviour of a phase change system can be described by the conservation equations for mass, momentum, species and energy in the solid, liquid and mushy zones. In addition, appropriate relations are required for determining the portion of solid or liquid in each computational cell. Since most industrial applications have complex geometries, all the conservation equations should be solved on a body fitted, i.e. unstructured, grid to minimize the computational errors.

The casting process occurs across a wide range of time and length scales, therefore, a complete solidification model must also account for this. For example, in solidification processes, the time scale can vary from 10^{-6}(s), which is associated with nucleation kinetics, to 10^{-1} (s) that occurs in an industrial solidification process. The length scale can also range from submicron, associated with solid-liquid interface, to industrial process scale with a length scale of metres [33]. While one may choose any appropriate scales depending on the scope of the problem, most solidification models often analyze solidification problems at an intermediate scale, the meso-scale (10^{-4}). This scale allows description of the features of microstructure at the grain level, without resolving the grain boundary. Standard transport models of the type developed for the macro-scale can be combined with transformation dynamics model to predict microstructure evolution [15].

There have been many attempts to model casting and casting defects through complex numerical models that solve the transport equations. To reduce the mathematical complexity of models and predict when and where there is high probability of defect formation in casting, researchers have developed analytical equations termed “criterion functions”[15]. These functions essentially are simple rules that relate the process parameters such as cooling rate, solidification velocity, thermal gradient, etc. to defects such as shrinkage defects. Depending on the assumptions on the physics of the problem and the mathematical apparatus used, different approaches can be summarized as follows:

Thermal models: This was a pioneering work of [34] in which only an energy transport equation is solved to identify the last region to solidify or regions where feeding becomes restricted. Using this model, the last region to solidify (hot spots) in a casting can be identified by mapping the isotherms. Assuming that shrinkage cavities are located in the last region to solidify, mapping the position but not the size of shrinkage could be predicted.

Thermal/fluid flow models: These models deal more or less with the whole transport problem but ignore the contribution of gas rejected by the solidifying melt to porosity formation. An early model by [35] assumed that void pores form because the section of the channel along which feed metal travels continuously narrows during solidification until the pressure drop finally blocks the liquid in the channel. The authors of [36] derived an expression for the pressure drop along the channel. Niyama et al. [37] used Darcy's law in cylindrical coordinates and expressed the pressure drop in the mushy zone as an inverse function of the ratio $\frac{G}{\sqrt{R}}$ (local thermal gradient/$\sqrt{cooling\ rate}$). Shrinkage defects form in the region where the ratio is smaller than a critical value, to be determined experimentally. While this criterion works well for low-carbon steel, its application by many non-ferrous foundries is questionable (see for example [38]).

MT-TK models: In these models macro-transport (MT) and transformation kinetics (TK) models are coupled to predict mechanical properties based on direct microstructure-properties correlations [15]. The two computations can be performed uncoupled if it is assumed that TK does not influence MT. For example, the rate of cooling is evaluated with an MT code, and then, the microstructure length scale that includes phase spacing, λ, and volumetric grain density are calculated based on empirical equations as a function of the rate of cooling [15].

According to the literature review that is presented in this chapter and the one in the subsequent chapter, it was found that based upon assumptions that dictate the nature of the problem in an application, various numerical packages exist that are capable of simulating solidification processes. However, in most of these existing formulations, i.e. [39,40] the numerical fine-tuning from one case to another is significant and unpredictable.

1.11 Scope and Objectives

The aims of the present work is to create a general formulation that generates fairly accurate results in the solidification of magnesium alloys, without numerical fine-tuning for convergence, that can be used to predict microstructural features and mechanical properties of these alloys. Following from this aim, the main objectives of this work may be stated:

- Derive a volume-averaged mass, momentum and energy formulation based upon reasonable assumptions that capture the physics involved in the solidification of magnesium alloys. Based upon the formulation derived, the transient flow and heat transfer during the solidification of a magnesium alloy, i.e.AM60B is to be studied and the resulting cooling curves to be discussed.

- Implement experimental correlations into the in-house code, so the microstructural features such as grain size can be approximated locally.

- Based upon the predicted local grain distribution and previously reported experimental data, the skin and core region can be identified for studying some of the local mechanical properties of magnesium alloys. i.e. yield strength.

1.12 Outline of the Remaining Chapters

The remainder of this thesis is divided into three chapters. The outline of these chapters is as follows:

The following chapter, Chapter 2, is a submitted article to the Journal of Numerical Heat Transfer Part A: Application and outlines a literature review of solidification modeling, their benefits and drawbacks. Then, a novel volume averaged governing equations and the details of their derivation are explained and numerical methods for the discretization procedure are presented. The result of a comparison of the numerical studies with previously reported experimental data is discussed in the last section of this paper.

Chapter 3 is a submitted article to Metallurgical and Materials Transaction B in which the developed formulation in Chapter 2 is used to predict the local grain size and mechanical properties of Mg alloys. The effect of different cooling rate on the grain size distribution in magnesium alloys is studied. Then, the closest result to the experimental data is chosen for the identification of skin and core region. At the end, the experimental correlations are used to predict the yield strength based upon the thickness of the core and skin.

Chapter 4 provides a summary of the work. The present contributions are listed along with recommendations for future work.

1.13 References

[1] Mg, A North American Strategic Vision for Auto Weight Reduction, US Auto partnership, 2005

[2] B.J. Coultes: Mechanical Property Variations in a Magnesium High-Pressure Die-Cast Component. University of Western Ontario: London, Ontario, 2003, M.E.Sc. Thesis.

[3] J.P. Weiler, Structure property relationships for die-cast magnesium alloy AM60B, M.E.Sc. Thesis, The University of Western Ontario, London, Ontario, Canada, 2005

[4] J.P. Weiler, The development of comprehensive material models of the structure-property relationship for die-cast magnesium alloy AM60B, Ph.D. thesis, The University of Western Ontario, London, Ontario, Canada, 2009

[5] I. Basu, Effect of process variables on the microstructural features for as-cast magnesium alloys, M.E.Sc. Thesis, The University of Western Ontario, London, Ontario, 2011

[6] A. Banerjee, Process structure relationships of magnesium alloys, M.E.Sc thesis, The University of Western Ontario, London, Ontario, 2013

[7] M. Farrokhnejad, A.G. Straatman, J.T. Wood, A Finite-Volume Model for numerical solidification of Mg alloys, Materials Science Forum vol. 765, pp. 281-285, 2013

[8] ASM Specially Handbook, Magnesium and Magnesium alloys, Eds. M.A. Avedesian and H. Baker, Metals Park, OH, 1999

[9] A.K. Dahle, Y.C. Lee, M.D. Nave, P.L. Schaffer, and D.H. StJohn: Development of the as-cast microstructure in magnesium-aluminum alloys, Journal of Light Metals, vol. 1, pp.61-72. 2001

[10] T. Aune and H. Westengen: Magnesium die casting properties. Automotive Engineering, vol.1, pp.87-92, 1995

[11] W.D. Callister, Jr., Materials Science and Engineering, An Introduction, John Wiley & Sons, Sixth Ed. Hoboken, NJ, USA, 2003

[12] H.E., Friedrich and B.L. Mordike, Magnesium Technology: Metallurgy, Design Data, Applications, Springer, New York, USA, 2006

[13] D. A. Porter and K. E. Easterling, Phase Transformations in Metals and Alloys, CRC PressI Llc, 1992.

[14] K. Fisher, and W. Kurz, Fundamentals of solidification, Trans Tech Publications, 1986

[15] D. M. Stefanescue, Science and Engineering of Casting Solidification Springer-Verlag US, 2009

[16] R. Trivedi and K. Somboonsuk, Constrained dendritic growth and spacing, Materials Science and Engineering, vol. 65, pp.65-74, 1984

[17] E.J. Lavernia and T.S. Srivatsan, The rapid solidification processing of materials: Science, principles, technology, advances, and applications, Journal of Materials Science, vol.45, pp. 287-325, 2010

[18] J.A. Dantzig and M. Rappaz, Solidification, CRC Press, Boca Raton, FL, USA, 2009

[19] W. J. Boettinger and S. R. Coriell. "Science and Technology of the Undercooled Melt (edited by PR Sahm, H. Jones and CM Adams)." Martinus Nijhoff, Dordrecht, The Netherlands p. 81, 1986

[20] R.W. Heine, C.R. Loper and P.C. Rosenthal, Principal of metal casting, McGraw-Hill, New York, 1967

[21] H. Gjestland, S. Sanned and H. Westengen, High pressure die casting – getting the best out of magnesium, The 10th Mg Automotive and End User Seminar, Aalen, Germany, 2002

[22] T. Maier, J Kolakowski and J. Wallace, Die Casting of copper Alloys, AFS Transactions, vol.83, pp. 279-294, 1975

[23] A. Balasundaram and A.M. Gokhale: Quantitative characterization of spatial arrangement of shrinkage and gas (air) pores in cast magnesium alloys. Materials Characterization vol. 46, pp.419-426, 2001

[24] A.M. Gokhale, and G.R. Patel: Origins of Variability in the Mechanical Properties of AM60 Magnesium Alloy Castings, Magnesium Technology 2001, ed. J. Hryn, pp.195-199, 2001

[25] S.G. Lee, G.R. Patel, A.M. Gokhale, A. Sreeranganthan, and M.F. Horstemeyer: Variability in the tensile ductility of high-pressure die-cast AM50 Mg-alloy. Scripta Materialia, vol.53, pp.851-856, 2005

[26] C.D. Lee: Tensile properties of high-pressure die-cast AM60 and AZ91 magnesium alloys on microporosity variation. Journal of Material Science, vol. 42, pp.10032-10039, 2007

[27] C.D. Lee: Dependence of tensile properties of AM60 magnesium alloy on microporosity and grain size, Materials Science and Engineering. Vol. A454-455, pp.575 580, 2007

[28] L. John, Presentation slides at Meridian Lightweight Technology, 2008

[29] Piwonka T.S., 2000, in: Proceedings of the Merton C. Flemings Symposium on Solidification and Materials Processing, R. Abbaschian, H. Brody, and A. Mortensen eds.,TMS, Warrendale Pa. p.363

[30] D. M. Stefanescue, Computer simulation of shrinkage related defects in metal castings – a review, International Journal of Cast Metals Research, vol. 18, pp.129-143, 2005

[31] Sieverts, Adolf , The Absorption of Gases by Metals. Zeitschrift für Metallkunde vol.21, pp. 37–46, 1929

[32] M. Zerroukat, and C. R. Chatwin Computational moving boundary problem Research Studies Press, England, 1994

[33] V. R. Voller Numerical Methods for phase-change problems, in: edited by W.J. Minkowycz, E.M. Sparrow, J. Y. Murthy; with editorial assistance by John P. Abraham, Handbook of numerical Heat transfer, 2nd ed. Hoboken, N.J: J. Wiley, PP. 593-622, 2006

[34] J. G. Henzel, and J. Keverian, Computer Programs for Heat Flow Calculations, Transactions of the American Foundrymen's Society, vol.74, pp.661-79, 1966

[35] W.D.Walther, C.M. Adams and H.F.Taylor, Techniques of improving strength and ductility of Al alloy castings, Transaction, A F S, vol. 64, p.658, 1956

[36] T. S. Piwonka and M. C. Flemings, Pore formation in solidification, AIME MET SOC TRANS, vol. 236.8, pp.1157-1165, 1966

[37] E. Niyama, T. Uchida, M. Morikawa and S. Saito, A method of shrinkage prediction and its application to steel casting practice, International Cast Metal Journals vol. 7.3, pp. 52-63, 1982

[38] J. A. Spittle, M. Almeshhedani, and S. G. R. Brown, The Niyama function and its proposed application to microporosity prediction, Cast Metals vol.7, p.51, 1994

[39] A.D. Brent, V. R. Voller and K.J. Reid, Enthalpy-porosity technique for modeling convection-diffusion phase change: application to the melting of a pure metal, Numerical Heat Transfer, vol.13, pp.297-318, 1988

[40] V.R. Voller and C. Prakash, A fixed grid numerical modeling methodology for convection-diffusion mushy region phase-change problems, International Journal of Heat and Mass Transfer, vol.30, (8), pp.1709-1719, 1987

Chapter 2

2 A Volume Averaged Finite-Volume Model for Solidification of Magnesium Alloys on a General Unstructured Collocated Grid

2.1 Introduction and Literature Review

Automakers are concentrating on reducing car weight and limiting exhaust emissions due to legislative requirements for safer, cleaner vehicles. Lightweight alloys including magnesium (Mg) alloys could reduce manufacturing cost versus steel, especially for production volumes of less than 200,000 units per year [1]. However, defects that often develop during the casting of these alloys lead to the local degradation of mechanical properties and prevent them from being used widely. A better understanding of the casting process will mitigate such defects and lead to minimization of the prototyping sequence for newly developed alloys or die designs, and will also reduce costs by minimizing the production of these prototype castings for testing.

Understanding the solidification process, as an inherent part of casting processes, is essential to achieving these goals. Castings are made with dimensions of a few millimeters up to meters in length. However, since the as-cast microstructure of the casting determines its properties, studying the solidification process at this scale is essential. In general, to better understand the microstructure of castings, changes in the solid/liquid interface during the solidification process should be considered at the nano, micro and macroscale.

Because solidification is the process of moving individual atoms from the liquid phase to the solid alloy lattice, studying the distances over which atoms travel is of a great importance as well. Monte Carlo methods are used at the nanoscale in which the atomic morphology of the solid/liquid interface is discussed in terms of nucleation and growth kinetics. The complex morphology of the solidification grains can be described using either the Cellular Automaton (CA) technique or phase field methods at the microscale.

Also, one can choose to study solidification processes at the macro scale (100 to 10^{-3} (m)). However, since at this scale only two phases are assumed to exist, the solid and the liquid, it is customary to analyze solidification processes at an intermediate scale, mesoscale (10^{-4} (m)), in which the microstructure features at the grain level are considered, but without resolving the grain boundary. At this scale, there is no clear boundary between solid and liquid and in fact, three regions can be observed: liquid, mushy (contains both liquid and solid) and solid, Fig. (2-1).

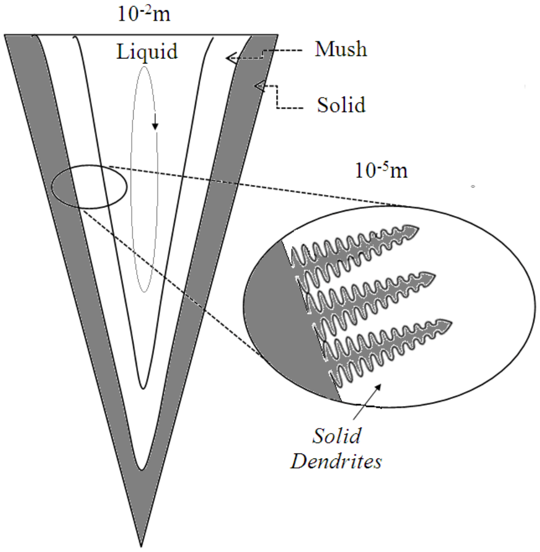

Figure 2-1: Schematic of different length-scale in a typical wedge casting

The computational models that describe solidification at this scale are typically either based on the CA technique or the combined macroscopic transport equations with transformation kinetics models, in which the evolution of grain morphology would not be the output of the simulation. In such models, for example, one can use microscale models to calculate the variation of solid fraction during solidification and pass the results to the macroscopic model for the computation of the latent heat released. The evaluation of the new temperature field is, in turn, passed to the microscale model to determine a new solid fraction [2-4]. One should note that an accurate measurement of crucial parameters such as cooling rate and solid volume fraction at this scale are essential for verification.

To derive macroscopic models of the transport phenomena, techniques such as volume-averaging, mixture theory, and more recently, the homogenization method [5], are often utilized to average the microscopic (exact) equations over a finite sized volume, which is much smaller than the size of the system and large compared to the characteristic size of the interfacial structures. Then, the resulting averaged or macroscopic equations of each constituent can be combined with transformation kinetics models to predict microstructure evolution [3]. An extensive number of publications exist on the macro-mesoscale modeling of solidification processes, however, most of the formulations are based upon the initial work of a few groups of researchers.

The pioneering efforts of [6-8] utilize mixture theory to derive single-phase macroscopic equations without reference to any microscopic equations, thereby, eliminating the need for separate phase conservation equations by assuming that each phase is a continuum that occupies the entire domain, described by a set of variables that are continuous and differentiable functions of space and time. The major advantage of single region formulations is that their solution can be obtained by conventional numerical methods [9]. While mixture theory assumes the validity of certain continuum relations on a macroscopic scale, approaches that are motivated by general theories of flow through porous media [10-12] utilize formal volume averaging procedures [13-15] in which various macroscopic terms and their relationship to the microscopic terms are clear. Hence, future transformation kinetics models can be coupled to this type of formulation with more insight. One should note that with carefully made assumptions one can derive the same macroscopic equations using both aforementioned approaches [16].

The mixture formulated volume-averaged transport equations of [13], in which the volume-averaged macroscopic transport equations are added together, have been used in various publications [17-20]. While using mixture density and thermal conductivity in this type of formulation might be physically reasonable, the effective or mixture viscosity in a mixture momentum equation, at least in the context of alloy solidification, might not be physically meaningful [15]. This is particularly true when purely numerical assumptions are made for the value of the permeability in the Darcy term for closure of the equation [21]. A better way to model the flow in the single equation approach would be to use only the liquid momentum equation and account for the changes in the flow by closure terms similar to those used in porous media application, implemented in solidification process modeling [22]. Other transport equations can be used in the form of mixture transport equations without compromising the physical description of the problem.

Not surprisingly, assumptions that have been made to derive the volume-averaged equations [15,20,22] for a solidification process are similar to those used for a porous medium. However, one must notice that the assumption of constant porosity or a zero gradient of volume fraction is not reasonable in the case of a solidification problem as the volume fraction of solid (liquid) is changing spatially and temporally. In addition, the volume-averaged transport equations that are used for porous media and conjugate domain problems are used in fixed geometries in which the pore region boundaries are set to coincide with the control volumes boundaries. Hence, all the corrections that have been made for interface conditions between solid and liquid are applicable to the cases where there exists a sharp interface that coincides with the control volume boundaries. Noting that at the mesoscale no sharp interface exists, the jump conditions including pressure gradient from solid/mushy or mushy/liquid control volumes must be smoothed in a different way than that proposed in porous media literature.

Also, a challenging complication in solving the energy equation is updating the value of solid volume fraction and evolving the latent heat of fusion in the energy equation. While it is not correct to assume that within the small volume element the liquid is solutally well mixed and species diffusion in the solid is either complete or absent, there are three prevalent solution techniques currently available: effective specific heat, enthalpy method and source based method for solving the energy equation.

In the effective specific heat method, an apparent heat capacity is defined in the range of temperature in which phase change happens, so it accounts for the entire enthalpy change, including sensible and latent heat. For the case of a pure material or an alloy of eutectic composition, an artificial phase change temperature range must be implemented during which the latent heat is released, [23,24]. Although this approach is numerically stable, an important drawback of this method is that when a nodal temperature in one time step falls from above the liquidus temperature to below solidus temperature, the latent heat released is not accounted for. To solve this issue, a large mushy region must be assumed, which may not be physically meaningful [25].

Probably the most extensively used formulation is the enthalpy-porosity approach, which was proposed by [19]. The basic method includes casting the energy equation in terms of enthalpy instead of temperature to overcome the singularity at the eutectic point of an alloy or at the melting temperature of a pure substance. Then, based on the latent heat release characteristics of the phase change material, a variation between the total enthalpy and temperature is defined. The enthalpy method is reasonably accurate for materials solidifying over a range of temperatures, [26] however, it is more complex than effective specific heat method and is known to produce ‘wiggles’ or ‘false’ eutectic plateaus in the cooling curves [27].

A substitute for setting up a non-linear coefficient in the form of a specific heat is to develop a non-linear source term in the energy transport equation similar to the enthalpy method. This technique, which is called ‘Source-based’ technique [28], can deal with a general liquid fraction curve, unlike the apparent heat capacity method, and also has a certain similarity to the enthalpy formulation. The latent heat appears as a source term in the energy equation and in this way it is directly coupled to the nodal temperature, which produces fairly accurate results, particularly for non-isothermal solidification. Careful implementation of the appropriate source terms could remove the potential for oscillations in the iterative solution while providing an accurate characterization of the solidification process.

Considering the above background and literature review, in the current work, a set of volume-averaged equations similar to the one proposed by [13] with the additional assumption of variable porosity in the mushy zone is presented. All assumptions in the derivation of the equations are outlined in detail and additional terms are physically reasoned. Particularly, an explanation is presented for the relationship between the Darcy term and the additional term in the new proposed formulation. Special care is given to the control volumes that are adjacent to solid and liquid control volumes. For the energy equation, a temperature-dependent, source-based formulation similar to the approach of [28] is derived. However, in addition to the effect of convection, which has a significant influence on the solidification process [22], it is shown how a unique derivation of the energy equation can eliminate unnecessary terms that account for the evolution of latent heat. Physically reasonable logic is then presented to avoid instability in the solution process. As a demonstration of the robustness of the proposed numerical formulation, a wedge casting solidification of a Mg alloy is predicted and results are compared with existing experimental data.

2.2 Mathematical Formulation

In this section, the mathematical model of fluid flow and the heat transfer in a domain consisting of solid, liquid, and mushy regions is presented. In order to provide some physical insight of the mathematical model used in this study, a brief review of the volume averaging techniques is presented along with all the related assumptions and constraints that have been made to make the general equations amenable to the purpose of this study. In addition, appropriate relations that are required for determining the portion of solid and/or liquid in each control volume, and for representing the variation of mixture properties in the mushy region are clearly stated.

2.2.1 Microscopic Transport Equations

The microscopic mass, momentum and energy equations for a medium consisting of phase that is undergoing phase change is given by:

$$\frac{\partial \rho_k}{\partial t} + \nabla \bullet \left(\rho_k \vec{v}_k \right) = 0 \tag{2-1}$$

$$\frac{\partial}{\partial t}\left(\rho_k \vec{v}_k \right) + \nabla \bullet \left(\rho_k \vec{v}_k \vec{v}_k \right) = -\nabla P_k + \nabla \bullet \left(\mu_k \nabla \vec{v}_k \right) + \rho_k \vec{b} \tag{2-2}$$

$$\frac{\partial}{\partial t}\left(\rho_k h_k \right) + \nabla \bullet \left(\rho_k h_k \vec{v}_k \right) = \nabla \bullet \left(k_k \nabla T_k \right) \tag{2-3}$$

for the k^{th} phase.

2.2.2 Volume-Averaged Transport Equations

A phase represents a quantity of matter, which is homogeneous in physical structure and comprised of one or more compounds. An interfacial length scale can be defined as the ratio of the volume of the structure to the interfacial area. In alloy solidification processes, in the case of equiaxed or columnar growth of solid crystals, the interdendritic liquid, which is the liquid that flows between dendrite arms, and the solid crystals share the same length scale of the order of 10^{-5} to 10^{-4} (m), whereas the interface between the liquid outside the region of the grain growth and the interdendritic liquid has a larger length scale by one order of magnitude. The size of the Representative Elementary Volume (REV) shown in Fig. (2-2) must be chosen in such a way that it is much larger than all the interfacial length scales, to smooth out the complexities of the problem related to the morphology, interdendritic flow and latent heat release, etc., but small compared to the system scale, to capture the global characteristics of flow field and heat transfer.

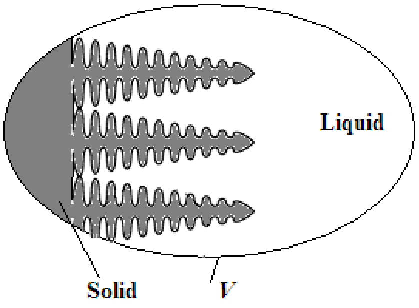

Figure 2-2: Schematic illustration of the averaging volume containing columnar dendritic crystals

The REV can vary between 10^{-3} to 10^{-2} (m). It is worth mentioning that in case of problems with columnar dendritic growth in which the microstructure evolves in a heterogeneous manner, then the defined REV should vary in size and the aforementioned discussion for the size of REV might not be correct.

Once the REV is defined, to cast the macroscopic governing equations for studying the behaviour of fluid undergoing phase change, the following averaging theorem and assumptions have been implemented:

- A characteristic phase function, f_k, associated with the portion of the REV that is occupied by one of the constituents is defined. Herein, the REV includes pure fluid (phase k) if the value of f_k is unity and solid if it is zero. Consequently, any value of f_k between unity and zero indicates a mixed control volume or mushy region. The volume fraction of phase liquid (or solid), f_k, can be defined as:

$$f_k = \frac{1}{V}\int_{V_k} f_k(\vec{x},t)dV = \frac{V_k}{V} \tag{2-4}$$

- The extrinsic or superficial average of property φ_k associated with phase k is defined as:

$$\left\langle \varphi_k \right\rangle = \frac{1}{V}\int_{V_k} \varphi_k dV \tag{2-5}$$

- The intrinsic average is defined as:

$$\left\langle \varphi_k \right\rangle^k = \frac{1}{V_k}\int_{V_k} \varphi_k dV = \frac{\left\langle \varphi_k \right\rangle}{f_k} \tag{2-6}$$

  When φ_k is uniformly distributed in V_k, then $\left\langle \varphi_k \right\rangle^k = \varphi_k$.

- The total average over V of a property defined in all phases is defined by:

$$\left\langle \varphi \right\rangle = \frac{1}{V}\int_{V} \varphi dV \tag{2-7}$$

- Spatial averaging theorem proposed by [29,30] is used to average terms that include gradient and divergence of a variable:

$$\left\langle \nabla \varphi_k \right\rangle = \nabla \left\langle \varphi_k \right\rangle + \frac{1}{V} \int_{A_k} \varphi_k \hat{n} dA_k$$
$$\left\langle \nabla \bullet \varphi_k \right\rangle = \nabla \bullet \left\langle \varphi_k \right\rangle + \frac{1}{V} \int_{A_k} \hat{n} \bullet \varphi_k dA_k \tag{2-8}$$

- The fluctuating component, which represents the deviation of φ_k from the intrinsic volume average property, is defined by:

$$\hat{\varphi}_k = \varphi_k - \left\langle \varphi_k \right\rangle^k \tag{2-9}$$

This is similar to the time averaging of turbulent transport equation proposed by [31] in which the velocity is decomposed into a time average and a temporal deviation. In the method of volume averaging it is customary to decompose the velocity and pressure into spatial averages and spatial deviations.

- In the case where the average of a product exists, while it is the product of averages that is desired, the method of [10] is followed:

$$\left\langle \varphi_k \psi_k \right\rangle = f_k \left\langle \psi_k \right\rangle^k \left\langle \varphi_k \right\rangle^k + \left\langle \hat{\varphi}_k \hat{\psi}_k \right\rangle$$
$$\left\langle \varphi_k \psi_k \right\rangle^k = \left\langle \psi_k \right\rangle^k \left\langle \varphi_k \right\rangle^k + \left\langle \hat{\varphi}_k \hat{\psi}_k \right\rangle^k \tag{2-10}$$

- And finally, the transient terms are averaged using

$$\left\langle \frac{\partial \varphi_k}{\partial t} \right\rangle = \frac{\partial \left\langle \varphi_k \right\rangle}{\partial t} - \frac{1}{V} \int_{A_k} \varphi_k \vec{v}_I \bullet \hat{n} \, dA_k \tag{2-11}$$

2.2.3 Continuity Equation

Taking the extrinsic average of Eq. (2-1), the volume averaged continuity equation may be expressed in the form:

$$\left\langle \frac{\partial \rho_k}{\partial t} \right\rangle + \left\langle \nabla \bullet \left(\rho_k \vec{v}_k \right) \right\rangle = 0 \tag{2-12}$$

Applying the previously shown theories:

$$\frac{\partial}{\partial t}\left(f_k\left\langle\rho_k\right\rangle^k\right)+\nabla\bullet\left[f_k\left\langle\rho_k\right\rangle^k\left\langle\vec{v}_k\right\rangle^k\right]=-\frac{1}{V_k}\int_{A_k}\rho_k\left(\vec{v}_k-\vec{v}_I\right)\bullet\hat{n}_k\,dA_k=\sum_{j=1}^{N}\dot{m}'''_{jk} \quad (2\text{-}13)$$

In which the R.H.S of Eq. (2-13) represents the net rate of mass exchange of phase *k* at the *jk* interface and is constrained by interfacial balances on the interface. Since the overall interfacial balance follows by adding the interfacial balance for each interface, the R.H.S of the Eq. (2-13) is zero in a REV, [13].

Assuming that the variation of material properties occurs globally and not within the dV_k i.e. $\left\langle\rho_k\right\rangle^k=\rho_k$ and also ignoring the effect of shrinkage and density variation, the intrinsic, Eq. (2-14), and extrinsic, Eq. (2-15), forms of continuity equation can be written as:

$$\rho_k\nabla\bullet\left[f_k\left\langle\vec{v}_k\right\rangle^k\right]=0 \qquad (2\text{-}14)$$

$$\rho_k\nabla\bullet\left\langle\vec{v}_k\right\rangle=0 \qquad (2\text{-}15)$$

It is worth mentioning that to cast the governing equations for studying the behaviour of continuum (fluid) undergoing phase change, we select the case in which the phase change region, also called mushy region, has a crystalline structure consisting of columnar grains with interdendritic liquid, and the solid/liquid interface is a complex shape that is not necessarily smooth. For a general case of columnar and equiaxed, in which the velocity of solid crystals is not necessarily zero, one can consider a mixture continuity equation in which the density and velocity are the summation of solid and liquid constituents. However, due to the assumptions that have been made, in this study, only the fluid continuity equation would be sufficient.

2.2.4 Momentum Equation

The extrinsically averaged momentum equation can be written as:

$$\left\langle \frac{\partial}{\partial t}\left(\rho_k \vec{v}_k\right)\right\rangle + \left\langle \nabla \bullet \left(\rho_k \vec{v}_k \vec{v}_k\right)\right\rangle = -\left\langle \nabla P_k \right\rangle + \left\langle \mu_k \nabla \bullet \nabla \vec{v}_k \right\rangle + \left\langle \rho_k \vec{b} \right\rangle \qquad (2\text{-}16)$$

Using the aforementioned theorems, noting that the volume of the phase k contained within the average volume is changing with time, the transient term of the momentum equation can be written as:

$$\left\langle \frac{\partial}{\partial t}\left(\rho_k \vec{v}_k\right)\right\rangle = \frac{\partial}{\partial t}\left[f_k \left\langle \rho_k \right\rangle^k \left\langle \vec{v}_k \right\rangle^k + \left\langle \hat{\rho}_k \hat{\vec{v}}_k \right\rangle \right] - \frac{1}{V}\int_{A_k} \rho_k \vec{v}_k \left(\vec{v}_I \bullet \hat{n}_k\right) dA_k \qquad (2\text{-}17)$$

Knowing that the correlation between the fluctuating components of $\hat{\rho}_k$ and $\hat{\vec{v}}_k$ is zero then Eq. (2-17) can be simplified to:

$$\left\langle \frac{\partial}{\partial t}\left(\rho_k \vec{v}_k\right)\right\rangle = \rho_k \frac{\partial}{\partial t}\left[f_k \left\langle \vec{v}_k \right\rangle^k \right] - \frac{1}{V}\int_{A_k} \rho_k \vec{v}_k \left(\vec{v}_I \bullet \hat{n}_k\right) dA_k \qquad (2\text{-}18)$$

The convective term can be written as:

$$\left\langle \nabla \bullet \left(\rho_k \vec{v}_k \vec{v}_k\right)\right\rangle = \rho_k \left[\nabla \bullet \left[f_k \left\langle \vec{v}_k \right\rangle^k \left\langle \vec{v}_k \right\rangle^k \right] + \frac{1}{V}\int_{A_k} \vec{v}_k \vec{v}_k \bullet \hat{n}_k \, dA_k \right] \qquad (2\text{-}19)$$

The pressure gradient can be extrinsically averaged as:

$$\left\langle \nabla P_k \right\rangle = \nabla\left(f_k \left\langle P_k \right\rangle^k \right) + \frac{1}{V}\int_{A_k} P_k \hat{n}_k \, dA_k \qquad (2\text{-}20)$$

Using Eq. (2-9) in Eq. (2-20) results in:

$$\left\langle \nabla P_k \right\rangle = \nabla\left(f_k \left\langle P_k \right\rangle^k \right) + \left(\frac{1}{V}\int_{A_k} \hat{n}_k \, dA_k \right) \left\langle P_k \right\rangle^k + \frac{1}{V}\int_{A_k} \hat{P}_k \hat{n}_k \, dA_k \qquad (2\text{-}21)$$

Knowing that

$$\left\langle \nabla 1 \right\rangle = \nabla \left\langle 1 \right\rangle + \frac{1}{V}\int_{A_k} \hat{n}_k \, dA_k = 0 \qquad (2\text{-}22)$$

then

$$\frac{1}{V}\int_{A_k}\hat{n}_k\,dA_k=-\nabla f_k \tag{2-23}$$

Substituting back into Eq. (2-21),

$$\left\langle\nabla P_k\right\rangle=\nabla\left(f_k\left\langle P_k\right\rangle^k\right)-\nabla f_k\left\langle P_k\right\rangle^k+\frac{1}{V}\int_{A_k}\hat{P}_k\hat{n}_k\,dA_k \tag{2-24}$$

According to [13], the second term on the R.H.S of Eq. (2-24) represents the buoyant force due to the average interfacial pressure, however the term “buoyant” could be misleading due to the fact that in an incompressible flow this term does not have any effects on the density. Herein, it is better to be interpreted as a momentum sink that senses the presence of interface. With further simplification:

$$\begin{aligned}&\left\langle\nabla P_k\right\rangle=\left(\nabla f_k\left\langle P_k\right\rangle^k+f_k\nabla\left\langle p_k\right\rangle^k\right)-\nabla f_k\left\langle P_k\right\rangle^k+\frac{1}{V}\int_{A_k}\hat{P}_k\hat{n}_k\,dA_k=\\&f_k\nabla\left\langle p_k\right\rangle^k+\frac{1}{V}\int_{A_k}\hat{P}_k\hat{n}_k\,dA_k\end{aligned} \tag{2-25}$$

The diffusion term in the momentum equation can be extrinsically averaged as:

$$\mu_k\left\langle\nabla\bullet\nabla\vec{v}_k\right\rangle=\mu_k\left[\nabla\bullet\left(\nabla\left\langle\vec{v}_k\right\rangle+\frac{1}{V}\int_{A_k}\vec{v}_k\hat{n}_k\,dA_k\right)+\frac{1}{V}\int_{A_k}\nabla\vec{v}_k\hat{n}_k\,dA_k\right] \tag{2-26}$$

where the second term on the R.H.S is zero if a no-slip boundary condition is applied.

Using Eq. (2-9) and (2-22),

$$\mu_k\left\langle\nabla\bullet\nabla\vec{v}_k\right\rangle=\mu_k\nabla\bullet\nabla\left(f_k\left\langle\vec{v}_k\right\rangle^k\right)+\mu_k\frac{1}{V}\int_{A_k}\nabla\hat{\vec{v}}_k\hat{n}_k\,dA_k-\mu_k\nabla f_k\left(\nabla\left\langle\vec{v}_k\right\rangle^k\right) \tag{2-27}$$

the momentum equation can be written as:

$$\begin{aligned}&\rho_k \frac{\partial}{\partial t}\left[f_k\left\langle\vec{v}_k\right\rangle^k\right]+\rho_k\nabla\bullet\left[f_k\left\langle\vec{v}_k\right\rangle^k\left\langle\vec{v}_k\right\rangle^k\right]=-f_k\nabla\left\langle P_k\right\rangle^k+\mu_k\nabla\bullet\nabla\left(f_k\left\langle\vec{v}_k\right\rangle^k\right)+\\&\frac{1}{V}\int_{A_k}\rho_k\vec{v}_k(\vec{v}_I-\vec{v}_k)\bullet\hat{n}_k dA_k+\\&\frac{1}{V}\int_{A_k}\left(\mu_k\nabla\hat{\vec{v}}_k-\vec{I}\hat{P}_k\right)\hat{n}_k\,dA_k-\mu_k\nabla f_k\left(\nabla\left\langle\vec{v}_k\right\rangle^k\right)+\rho_k f_k\left\langle\vec{b}\right\rangle\end{aligned}\qquad(2\text{-}28)$$

On the R.H.S of Eq. (2-28), it can be noted that with the assumption that has been made for Eq. (2-13), the third term is zero.

In a solidifying alloy, the liquid or more specifically the interdendritic liquid moves in a solid network in which the volume fraction of solid is continuously changing. While in most porous media, the fluid advects in a network with a uniform volume fraction of solid, it is still customary, and validated by experiment [32], to assume that the flow resistance in the mushy region is similar to that in a porous media. Hence, the momentum transfer due to interfacial interactions between the liquid and solid phases may be expressed in terms of a permeability tensor for flow through a continuous solid structure and since in most cases the solid structures are assumed to be isotropic, the fourth term on the R.H.S, which is referred to as a surface filter [12] can be estimated by the Darcy expression in terms of force per unit volume of porosity.

Then, Eq. (2-28) can be re-written as:

$$\begin{aligned}&\rho_k \frac{\partial}{\partial t}\left[f_k\left\langle\vec{v}_k\right\rangle^k\right]+\rho_k\nabla\bullet\left[f_k\left\langle\vec{v}_k\right\rangle^k\left\langle\vec{v}_k\right\rangle^k\right]=-f_k\nabla\left\langle P_k\right\rangle^k+\mu_k\nabla\bullet\nabla\left(f_k\left\langle\vec{v}_k\right\rangle^k\right)\\&-\frac{f_k^2\mu_f}{K}\left\langle\vec{v}_k\right\rangle^k-\mu_k\nabla f_k\left(\nabla\left\langle\vec{v}_k\right\rangle^k\right)+\rho_k f_k\left\langle\vec{b}\right\rangle\end{aligned}\qquad(2\text{-}29)$$

where the value of the K, the permeability in the Darcy term, can be approximated using the Kozeny-Carman equation:

$$K=\frac{\kappa f_l^3}{(1-f_l)^2}\qquad(2\text{-}30)$$

The value of κ depends on the size of the secondary dendrite arm spacing (SDAS) and morphology of the mushy region. This term has no effect on the momentum equation when it deals with pure liquid regions, while it is infinity in the pure solid regions.

The Darcy term and the fourth term in Eq. (2-29) both have similar effects on the momentum equation and there is no region where they act independently in terms of sign. The fourth term on the R.H.S of Eq. (2.29) is not considered explicitly in any previous volume averaged formulations for solidification, including the work of [13] or [20]. In regions where the volume fraction of the constituent varies dramatically, such terms are of great importance and should be considered. Moreover, in applications where the problem involves a creeping flow and a weak convection this term might not have a significant influence on the solution.

The intrinsic average of pressure gradient in the momentum equation is preferred since it provides better insight. Also, for the purpose of this study, the extrinsic form of Eq. (2-29) is more desirable, and can be written as:

$$\begin{aligned}\rho_k\left[\frac{\partial\langle\vec{v}_k\rangle}{\partial t}+\frac{1}{f_k}\nabla\bullet\left(\langle\vec{v}_k\rangle\langle\vec{v}_k\rangle\right)\right]=-f_k\nabla\langle P_k\rangle^k+\mu_k\nabla\bullet\nabla\langle\vec{v}_k\rangle- \\ \frac{f_k\mu_f}{K}\langle\vec{v}_k\rangle-\frac{\mu_k}{f_k}\nabla f_k\left(\nabla\langle\vec{v}_k\rangle\right)+\rho_k f_k\langle\vec{b}\rangle\end{aligned} \tag{2-31}$$

Density is assumed to be constant, except in the buoyancy term. The buoyancy effects are modeled using Boussinesq approximation:

$$\rho_k f_k\langle\vec{b}\rangle=\rho f_k\vec{g}\beta\left(\langle T\rangle-T_{ref}\right) \tag{2-32}$$

2.2.5 Energy Equation

The extrinsic volume average of Eq. (2-3) is:

$$\left\langle\frac{\partial}{\partial t}\left(\rho_k h_k\right)\right\rangle+\left\langle\nabla\bullet\left(\rho_k h_k\vec{v}_k\right)\right\rangle=\left\langle\nabla\bullet k_k\nabla T_k\right\rangle \tag{2-33}$$

Using Eq. (2-4) – (2-9) and Eq. (2-11),

$$\begin{aligned}&\frac{\partial}{\partial t}\left[\rho_k f_k \left\langle h_k \right\rangle^k\right] - \frac{1}{V}\int_{A_k} \rho_k h_k \left(\vec{v}_I \bullet \hat{n}_k\right) dA_k + \nabla \bullet \left[\rho_k f_k \left\langle h_k \right\rangle^k \left\langle \vec{v}_k \right\rangle^k\right] \\ &+ \frac{1}{V}\int_{A_k} \rho_k h_k \vec{v}_k \bullet \hat{n}_k \, dA_k = k_k\left[\nabla \bullet \left(\nabla \left\langle T_k \right\rangle + \frac{1}{V}\int_{A_k} T_k \hat{n}_k \, dA_k\right)\right] + \frac{1}{V}\int_{A_k} k_k \nabla T_k \hat{n}_k \, dA_k\end{aligned} \tag{2-34}$$

In the first term on the R.H.S of Eq. (2-34), the second term in parenthesis is called tortuosity and is a measure of diffusion in the mushy zone. Using Eq. (2-8) and Eq. (2-22), the first term in the R.H.S of equation (2-34) can be written as:

$$\begin{aligned}&k_k\left[\nabla \bullet \left(\nabla \left\langle T_k \right\rangle + \frac{1}{V}\int_{A_k} T_k \hat{n}_k \, dA_k\right)\right] = \\ &\nabla \bullet \left(k_k \nabla\left(f_k \left\langle T_k \right\rangle^k\right) + \frac{k_k}{V}\int_{A_k} \hat{T}_k \hat{n}_k \, dA_k - k_k \left\langle T_k \right\rangle^k \nabla f_k\right)\end{aligned} \tag{2-35}$$

To close the solid energy equation, a substitution similar to the substitution of [12] and [33] can be used for $\hat{T}_k$ in Eq. (2-35),

$$\begin{aligned}&k_k\left[\nabla \bullet \left(\nabla \left\langle T_k \right\rangle + \frac{1}{V}\int_{A_k} T_k \hat{n}_k \, dA_k\right)\right] = \\ &\nabla \bullet \left(f_k k_k \nabla \left\langle T_k \right\rangle^k + \frac{k_k}{V}\int_{A_k} \left(\vec{b}_k \bullet \nabla \left\langle T_k \right\rangle^k\right) \hat{n}_k \, dA_k\right)\end{aligned} \tag{2-36}$$

By defining the effective conductivity as:

$$k_{eff,k} = f_k k_k \vec{I} + \frac{k_k}{V}\int_{A_k} \vec{b}_k \hat{n}_k \, dA_k \tag{2-37}$$

Then Eq. (2-36) can be simplified as:

$$k_k\left[\nabla \bullet \left(\nabla \left\langle T_k \right\rangle + \frac{1}{V}\int_{A_k} T_k \hat{n}_k \, dA_k\right)\right] = \nabla \bullet \left(k_{eff,k} \nabla \left\langle T_k \right\rangle^k\right) \tag{2-38}$$

The closed form of energy equation for each constituent can be written as:

$$\begin{aligned}&\frac{\partial}{\partial t}\left[\rho_k f_k \left\langle h_k \right\rangle^k\right] + \nabla \bullet \left[\rho_k f_k \left\langle h_k \right\rangle^k \left\langle \vec{v}_k \right\rangle^k\right] = \\ &\nabla \bullet \left(k_{eff,k} \nabla \left\langle T_k \right\rangle^k\right) + \frac{1}{V}\int_{A_k} k_k \nabla T_k \hat{n}_k \, dA_k - \frac{1}{V}\int_{A_k} \rho_k h_k \left(\vec{v}_I - \vec{v}_k\right) \bullet \hat{n}_k \, dA_k\end{aligned} \qquad (2\text{-}39)$$

If the structure of the solid crystal is considered to grow in a columnar shape, as long as dendrites are not fragmented and surrounded by the melt, then $k_{eff,k}$ has a non zero value and should be obtained from measurements. If fragmentation happens $k_{eff,k}$ can have the value of zero as no heat can be transferred through such solid on a macroscopic scale. Only a few studies have been done on this topic despite its importance [34]. In this study, we assume that the $k_{eff,k}$ has a value equal to the value of k_k.

In addition, the third term on the R.H.S of Eq. (2-39) is equal to zero for the same reason as discussed earlier for Eq. (2-11).

In the solidification of metal alloys, since the Lewis number of a liquid metal is large $(Le \geq 1000)$, thermal equilibrium is readily achieved and nonequilibrium effects are mostly influenced by solutal undercooling. Hence, assuming thermal equilibrium to exist interfacially and through an REV is correct, $\left\langle T_s \right\rangle^s = \left\langle T_l \right\rangle^l = \left\langle T \right\rangle = T$. Using Eq. (2-39) for solid and liquid and adding them together results in:

$$\begin{aligned}&\frac{\partial}{\partial t}\left[\rho_s f_s \left\langle h_s \right\rangle^s + \rho_l f_l \left\langle h_l \right\rangle^l\right] + \nabla \bullet \left[\rho_l f_l \left\langle h_l \right\rangle^l \left\langle \vec{v}_l \right\rangle^l\right] = \\ &\nabla \bullet \left(f_s k_s \nabla \left\langle T_s \right\rangle^s + f_l k_l \nabla \left\langle T_l \right\rangle^l\right) + \frac{1}{V}\int_{A_s} k_s \nabla T_s \hat{n}_s \, dA_s + \frac{1}{V}\int_{A_l} k_l \nabla T_l \hat{n}_l \, dA_l\end{aligned} \qquad (2\text{-}40)$$

Considering the fact that the REV is isothermal, the total enthalpy, H, which is the combination of the enthalpy of solid and liquid, can be defined as:

$$H = \left(\int_{T_{ref}}^{T} Cp_s \, d\theta\right) + \left(\int_{T_{ref}}^{T} Cp_l \, d\theta + L_{ls}\right) \qquad (2\text{-}41)$$

in which, Cp_s, Cp_l, L_{ls} are the specific heat of solid, specific heat of liquid and the latent heat of fusion, respectively. Also, noting that the last two terms on the R.H.S of Eq. (2-40) represent the interfacial heat transfer, they can be modeled using Newton's cooling law:

$$\begin{aligned} \frac{1}{V}\int_{A_s} k_s \nabla T_s \hat{n}_s \, dA_s &= -h_{sl} A_{sl} \left(\left\langle T_s \right\rangle^s - \left\langle T_l \right\rangle^l \right) \\ \frac{1}{V}\int_{A_l} k_l \nabla T_l \hat{n}_l \, dA_l &= +h_{sl} A_{sl} \left(\left\langle T_s \right\rangle^s - \left\langle T_l \right\rangle^l \right) \end{aligned} \qquad (2\text{-}42)$$

Then, Eq. (2-40) can be re-written as:

$$\begin{aligned} &\frac{\partial}{\partial t}\left[\rho_s \left(1-f_l\right) \int_{T_{ref}}^{T} Cp_s \, d\theta + \rho_l f_l \left(\int_{T_{ref}}^{T} Cp_s \, d\theta + L_{ls} \right) \right] + \\ &\nabla \bullet \left[\rho_l f_l \left(\int_{T_{ref}}^{T} Cp_l \, d\theta + L_{ls} \right) \left\langle \vec{v}_l \right\rangle^l \right] = \nabla \bullet \left(f_s k_s + f_l k_l \right) \nabla \left\langle T \right\rangle \end{aligned} \qquad (2\text{-}43)$$

Introducing the mixture specific heat and thermal conductivity coefficient,

$$\begin{aligned} Cp_m &= \left(1-f_l\right) Cp_s + f_l Cp_l \\ k_m &= \left(1-f_l\right) k_s + f_l k_l \end{aligned} \qquad (2\text{-}44)$$

the final form of energy equation is

$$\begin{aligned} &\rho Cp_m \frac{\partial \left\langle T \right\rangle}{\partial t} + \nabla \bullet \left[\rho_l f_l Cp_l \left\langle T \right\rangle \left\langle \vec{v}_l \right\rangle^l \right] = \\ &\nabla \bullet \left(k_m \nabla \left\langle T \right\rangle \right) - \delta H_P \frac{\partial f_l}{\partial t} - \nabla \bullet \left[\rho_l f_l L_{ls} \left\langle \vec{v}_l \right\rangle^l \right] + \nabla \bullet \left[\rho_l f_l Cp_l T_{ref} \left\langle \vec{v}_l \right\rangle^l \right] \end{aligned} \qquad (2\text{-}45)$$

in which

$$\delta H_P = \rho \left(\left\langle T \right\rangle - T_{ref} \right) \left(Cp_l - Cp_s \right) + \rho L_{ls} \qquad (2\text{-}46)$$

Re-writing Eq. (2-45) in terms of extrinsic velocity

$$\begin{aligned}&\rho Cp_m\frac{\partial\langle T\rangle}{\partial t}+\nabla\bullet\left[\rho_l Cp_l\langle T\rangle\langle\vec{v}_l\rangle\right]=\\&\nabla\bullet\left(k_m\nabla\langle T\rangle\right)-\delta H_P\frac{\partial f_l}{\partial t}-\nabla\bullet\left[\rho_l L_{ls}\langle\vec{v}_l\rangle\right]+\nabla\bullet\left[\rho_l Cp_l T_{ref}\langle\vec{v}_l\rangle\right]\end{aligned}\tag{2-47}$$

One should note that in an REV, once the solid is formed, the latent heat has already been released and it will not be carried out with the solid to another volume. Thus, the third term on the R.H.S. of the Eq. (2-47) must be set to zero, while it is considered non-zero in the work of [17], [21] or [35]. The final form of energy equation is reduced to:

$$\begin{aligned}&\rho Cp_m\frac{\partial\langle T\rangle}{\partial t}+\nabla\bullet\left[\rho_l Cp_l\langle T\rangle\langle\vec{v}_l\rangle\right]=\\&\nabla\bullet\left(k_m\nabla\langle T\rangle\right)-\delta H_P\frac{\partial f_l}{\partial t}-\nabla\bullet\left[\rho_l Cp_l T_{ref}\langle\vec{v}_l\rangle\right]\end{aligned}\tag{2-48}$$

2.3 Computational Methods

Most of the pioneering work that has been done on deriving single region formulations for simulation of phase change problems and particularly solidification processes are discretized either based on the finite difference method (FDM), [18,19,21], in which all applications have been applied to structured and staggered grids, or the finite element method (FEM), [20,28]. While all of these formulations were successful for their specific applications, which were mostly two-dimensional and easily discretized using orthogonal grids, it is quite cumbersome to implement a staggered grid formulation for more general three-dimensional problems where nonorthogonal grids are required. Although FEM is similar to finite volume method (FVM) in many ways, the facts that the FVM is conservative by construction and each individual term has a physical significance makes it superior for studying the solidification and flow in casting processes and thus is considered in this work. Some researchers used the method of control volume-based finite difference [35,36] to discretize the governing equations on structured staggered grids, however, the model was again only tested for simple orthogonal grids, thus, it is unclear how the model would perform for nonorthogonal grid.

2.3.1 Spatial Discretization

Consider an arbitrary fixed control volume $\Omega_p \subset R^2$, of volume V and boundary, $\partial\Omega_p$ with unit vector $\hat{n}$ normal to the surfaces and pointing outward, filled by continuum (molten metal). The discretization of the governing equations is carried out on an unstructured grid, such as that illustrated in Fig. (2-3), in accordance with the cell-centred finite volume procedure of [9], using a colocated approach.

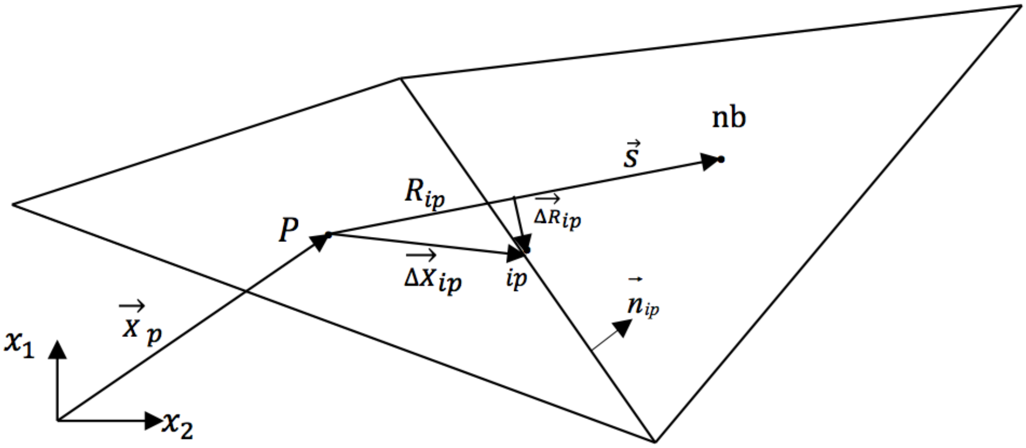

Figure 2-3: A portion of the grid and related nomenclature used in the FVM

The calculation domain is first sub-divided into arbitrary triangular or quadrilateral volumes, and the grid points are placed at the centres, $\vec{x}_p$, of the control volume, while boundary nodes, needed for implementing the boundary conditions, are located at the centre of boundary cell-faces.

Then, the governing equations are integrated over an arbitrary control volume with the volume of V_P, which is bounded by the control surface $\partial\Omega_P$, and time. The $\partial\Omega_P$ is assumed to be the union of the discrete control surfaces dA_{ip}, where $ip \in \{1,2,...,n_{ip}\}$, for $n_{ip} = 3$ triangles and $n_{ip} = 4$ for quadratic grids. All dependent variables, which are unknowns to be solved for, are stored at the centre of each control volume and the discrete equations formed for a control volume depend implicitly upon these values.

In the remainder, we consider a general transport equation for a conserved dependent variable $\varphi(\vec{x},t)$ that is differentiable, and obtain first the spatial discretization of unsteady, advective, diffusive and source terms in the governing equation, remarking any details that are found necessary, and then fully time-implicit discretized governing equations are presented. A general transport equation can be written as:

$$\rho\left[\frac{\partial\varphi}{\partial t}+\nabla\bullet\left(\vec{v}\varphi\right)\right]=\nabla\bullet\left(\Gamma\nabla\varphi\right)+S''' \tag{2-49}$$

2.3.1.1 Unsteady Term

The rate of change of storage of the conserved quantity within a control volume, V_P, is represented by the first term on the L.H.S of the momentum and energy equation. To obtain a spatial second order accurate discrete term, the integrand is expanded using a Taylor series about the centroid $\vec{x}_p$:

$$\int_{V_P}\rho\frac{\partial\varphi}{\partial t}dV=\int_{V_P}\left[\rho\left.\frac{\partial\varphi}{\partial t}\right|_P+\nabla\left.\left(\rho\frac{\partial\varphi}{\partial t}\right)\right|_P\bullet\left(\vec{x}-\vec{x}_p\right)+O(\delta^2)\right]dV \tag{2-50}$$

where φ is the unknown variable in the governing equations. Considering the definition of $\vec{x}_p$,

$$\vec{x}_P=\frac{\int_{V_p}\vec{x}\,dV}{V_P} \tag{2-51}$$

and centroid, the second term on the R.H.S of Eq. (2-50) is zero. Noting that the V_P is of the order of three, the unsteady term may be approximated as:

$$\int_{V_P}\rho\frac{\partial\varphi}{\partial t}dV=\rho V_P\left.\frac{\partial\varphi}{\partial t}\right|_P \tag{2-52}$$

2.3.1.2 Advection Terms

The mass equation and the second term in the momentum and energy equations represent the net rate of transport of the conserved quantity out of the control volume by advection. This is more obvious by integrating the term and employing the Gauss theorem to form the advective term as a surface integral over the control surfaces bounding volume V_P.

$$\int_{V_P} \rho \nabla . \left(\vec{v} \varphi \right) dV = \int_{A_{ip}} \rho \left(\vec{v} . \hat{n} \right) \varphi dA \tag{2-53}$$

where $\hat{n}$ is the outward unit normal to the control surface, (faces of a control volume). Writing the surface integral as the sum of integrals over the faces and expanding the integrands in Taylor series about the integration points, which is located at the centre of a face and is illustrated as ip in Fig. (2-3), results in:

$$\begin{aligned} &\int_{V_P} \rho \nabla \bullet \left(\vec{v} \varphi \right) dV = \\ &\sum_{ip}^{n_{ip}} \int_{A_{ip}} \left[\left(\rho \left(\vec{v} \bullet \hat{n} \right) \varphi \right) \Big|_{ip} + \nabla \left(\rho \left(\vec{v} \bullet \hat{n} \right) \varphi \right) \Big|_{ip} \left(\vec{x} - \vec{x}_{ip} \right) + O(\delta^2) \right] dA \end{aligned} \tag{2-54}$$

Again employing the definition of centroid and considering the fact that dA is of the order of two, the advective term will reduce to:

$$\int_{V_P} \rho \nabla \bullet \left(\vec{v} \varphi \right) dV = \sum_{ip}^{n_{ip}} \dot{m}_{ip} \varphi_{ip} \tag{2-55}$$

where the mass flux through the discrete control surface is computed as:

$$\dot{m}_{ip} = \rho \left(\hat{\vec{v}} \bullet \hat{n} \right) A_{ip} \tag{2-56}$$

where the advecting velocity $(\hat{\vec{v}} \bullet \hat{n})$ appearing in the mass flux expression for the C.V faces is adopted in accordance with the colocated variable method of Rhie and Chow [37], which uses a specially constructed momentum equation to avoid pressure-velocity decoupling.

The advected value of φ_{ip} is approximated implicitly by a first-order accurate upwind scheme to ensure numerical stability and then a deferred correction procedure [38] is employed to explicitly correct the advected value to higher order, see Appendix A for more detail.

2.3.1.3 Diffusive Term

The first term on the R.H.S. of the Eq. (2-49) represents the net rate of transport of the conserved quantity in to the C.V by the diffusion process associated with that quantity. Using the same analogy as arriving at Eq. (2-55), the diffusive term can be written as:

$$\int_{V_P} \nabla \bullet \left(\Gamma \nabla \varphi \right) dV = \sum_{ip}^{n_{ip}} \left[\Gamma \left(\nabla \varphi \Big|_{ip} \bullet n \right) A_{ip} \right] \qquad \text{(2-57)}$$

It is necessary to obtain a second-order accurate approximation for the gradient at the integration points to maintain the order of accuracy of Eq. (2-57). The authors of [39] derived a second order gradient and Hessian reconstruction in which the accuracy of the cell centre gradient and Hessian were estimated second order and first order, respectively. Having these approximations at the cell centre, we used the method of [40], in which the quantity of interest and its derivative is first interpolated to some point lying a fraction R_{ip}, see Fig. (2-3), of the distance along the vector that connects node P to its neighbor, $\vec{s}$, then extrapolated from this point to the integration point, See Appendix B. This leads to:

$$\nabla \varphi \Big|_{ip}^{m} \approx \overline{\nabla \varphi} \Big|_{ip}^{m-1} + \frac{1}{\vec{s}.\hat{n}_{ip}} \left\lfloor \left(\varphi_{nb}^{m} - \varphi_{p}^{m} \right) - \frac{1}{2} \left(\nabla \varphi \Big|_{p}^{m-1} + \nabla \varphi \Big|_{nb}^{m-1} \right) \bullet \vec{s} \right\rfloor \hat{n}_{ip} \qquad \text{(2-58)}$$

where $\overline{\nabla \varphi} \Big|_{ip}^{m-1}$ is calculated at the previous iteration, $m-1$.

2.3.1.4 Source Term

The last term on the R.H.S of Eq. (2-49) is a source term and since it is different from equation to equation, a more detailed explanation will be presented in the subsequent sections. The procedure to arrive at the spatial discretization of these terms is similar to the unsteady term:

$$\int_{V_P} S'''dV = S'''_P V_P \tag{2-59}$$

2.3.1.5 Governing Equations: Semi-Discrete

The semi-discretized forms of Eq. (2-15), (2-31) and (2-48) are given, respectively, for a fully implicit discretization as:

$$\sum_{ip=1}^{n_{ip}} \dot{m}_{ip} = 0 \tag{2-60}$$

$$\begin{aligned} &\rho V_P \frac{\partial \left\langle \vec{v}_l \right\rangle_P}{\partial t} + \sum_{ip=1}^{n_{ip}} \frac{\dot{m}}{f_l}\left(\left\langle \vec{v}_l \right\rangle_{ip} - \left\langle \vec{v}_l \right\rangle_P \right) = -\sum_{ip=1}^{n_{ip}} f_l \left\langle P_l \right\rangle_{ip}^{l} \hat{n}_{ip} A_{ip} + \\ &\sum_{ip=1}^{n_{ip}} \mu_l \nabla \left\langle \vec{v}_l \right\rangle_{ip} \bullet \hat{n}_{ip} A_{ip} - \frac{f_l \mu_l}{K} \left\langle \vec{v}_l \right\rangle_P V_P - \sum_{ip=1}^{n_{ip}} \mu_l \nabla f_l \Big|_{ip} \bullet \hat{n}_{ip} A_{ip} + \rho_l f_l \left\langle \vec{b} \right\rangle V_P \end{aligned} \tag{2-61}$$

$$\begin{aligned} &\rho Cp_m V_P \frac{\partial \left\langle T \right\rangle_P}{\partial t} + \sum_{ip=1}^{n_{ip}} \dot{m}_{ip} Cp_l \left(\left\langle T \right\rangle_{ip} - \left\langle T \right\rangle_P \right) = \\ &\sum_{ip=1}^{n_{ip}} k_m \nabla \left\langle T \right\rangle_{ip} . \hat{n}_{ip} A_{ip} - \delta H_P V_P \frac{\partial f_l}{\partial t} \end{aligned} \tag{2-62}$$

2.4 Temporal Discretization

In the present work, a fully implicit discretization is employed in which all terms are evaluated at the present time. The time derivative is discretized using backward differences. In Eq. (2-61) and Eq. (2-62), terms with the subscript ip are evaluated at the integration point located at the centroid of face A_{ip}. Note that Eq. (2-61) is in fact obtained by subtracting Eq. (2-60), multiplied by $\left\langle \vec{v}_l \right\rangle_P / f_l$, from the discretized form of equation (15). Also, Eq. (2-62) is subtracted from Eq. (2-60), multiplied by $Cp_l\left(\left\langle T \right\rangle_P - T_{ref} \right)$. This is done to ensure a conservative method. The fully discretized form of Eq. (2-49) can be written in the form of:

$$a_P \varphi_P^m = \sum\nolimits_{ip}^{n_{ip}} a_{nb} \varphi_{nb}^m + b_P \qquad \text{(2-63)}$$

2.5 Pressure-Velocity Coupling

As previously mentioned the approach of Rhie and Chow [37] is used to construct the special momentum equation. However, to show the effect of variable liquid volume fraction on the final form of special momentum equation, consider the x-momentum equation in the form of

$$a_P \left\langle u \right\rangle\Big|_P = \sum\nolimits_{ip=1}^{n_{ip}} a_{nb} \left\langle u \right\rangle\Big|_{nb} + b_P - f_{l,P} V_P \frac{\partial \left\langle p_l \right\rangle^l}{\partial x}\Big|_P = \left\langle \tilde{u} \right\rangle\Big|_P - f_{l,P} V_P \frac{\partial \left\langle p_l \right\rangle^l}{\partial x}\Big|_P \qquad \text{(2-64)}$$

in which the last term on the R.H.S of Eq. (2-64) depends upon the pressure field and the other term depends upon the velocity field. Also, for the C.V in the neighboring of volume P that shares the same integration point, one can write:

$$a_{P,nb} \left\langle u \right\rangle\Big|_{nb} = \left\langle \tilde{u} \right\rangle\Big|_{nb} - f_{l,nb} V_{nb} \frac{\partial \left\langle p_l \right\rangle^l}{\partial x}\Big|_{nb} \qquad \text{(2-65)}$$

Now, if a similar equation about the integration point is written based on the same analogy as above, then:

$$a_{P,ip} \left\langle \hat{\tilde{u}} \right\rangle\Big|_{ip} = \left\langle \tilde{u} \right\rangle\Big|_{ip} - f_{l,ip} V_{ip} \frac{\partial \left\langle p_l \right\rangle^l}{\partial x}\Big|_{ip} \qquad \text{(2-66)}$$

If an approximation for $a_{ip}$and V_{ip} is made, then the value of $\left\langle \tilde{u} \right\rangle\Big|_{ip}$ can be found by interpolation and the values of $\left\langle \tilde{u} \right\rangle\Big|_p$ and $\left\langle \tilde{u} \right\rangle\Big|_{nb}$.

Assuming that

$$a_{P,ip} = \frac{a_P + a_{P,nb}}{2} \;,\quad V_{ip} = \frac{V_P + V_{nb}}{2} \qquad \text{(2-67)}$$

and

$$f_{l,ip} = (1-R_{ip}) f_{l,P} + R_{ip} f_{l,nb} + \left[(1-R_{ip}) \nabla f_l \big|_P + R_{ip} \nabla f_l \big|_{nb} \right] . \Delta \vec{R}_{ip} \qquad (2\text{-}68)$$

The ∇f can be calculated using the Differential Least Square (DLS) method in which the volume fraction Taylor series expansion of f_P^{TS} are formed from a reference mixed control volume at $\vec{x}_P$ to each immediate neighbours, those having at least one vertex in common, f_i at point $\vec{x}_i$. However, this would result in a first order approximation of ∇f. In this work, the second order accurate reconstruction algorithm of [39] was used to evaluate the value of gradient of volume fraction at the cell centre. Then, $\langle \tilde{u} \rangle_{ip}$ can be written as:

$$\langle \tilde{u} \rangle \big|_{ip} = \frac{a_P + a_{P,nb}}{2} \overline{\langle u \rangle} \big|_{ip} + \frac{f_{l,ip} \left(V_P + V_{nb} \right)}{2} \overline{\frac{\partial \langle P_l \rangle^l}{\partial x}} \bigg|_{ip} \qquad (2\text{-}69)$$

where the overbar is an indication of the use of interpolation. Then substitution Eq. (2-69) in Eq. (2-66) and solving for advecting velocity, one obtains:

$$\langle \hat{\vec{u}} \rangle_{ip} = \overline{\langle u \rangle}_{ip} - \frac{f_{l,ip} (V_P + V_{nb})}{(a_P + a_{P,nb})} \left(\frac{\partial \langle p_l \rangle^l}{\partial x} \bigg|_{ip} - \overline{\frac{\partial \langle p_l \rangle^l}{\partial x}} \bigg|_{ip} \right) \qquad (2\text{-}70)$$

Writing Eq. (2-70) for all component of the advecting velocity, the advecting velocity in the direction of the normal to the integration point can be written as:

$$\langle \hat{\vec{u}} \rangle_{ip} . \hat{n}_{ip} = \overline{\langle \vec{u} \rangle}_{ip} . \hat{n}_{ip} - \frac{f_{l,ip} (V_P + V_{nb})}{(a_P + a_{P,nb})} \left(\nabla \langle p_l \rangle^l \big|_{ip} - \overline{\nabla \langle p_l \rangle^l} \big|_{ip} \right) . \hat{n}_{ip} \qquad (2\text{-}71)$$

The first pressure term in Eq. (2-69) can be approximated using Eq. (2-62):

$$\left\langle \hat{\vec{u}} \right\rangle_{ip} .\hat{n}_{ip} = \overline{\left\langle \vec{u} \right\rangle}_{ip} .\hat{n}_{ip} - \hat{d}_{ip} \left[\frac{\left\langle P_l \right\rangle_{nb}^{l} - \left\langle p_l \right\rangle_{P}^{l}}{\vec{s}.\hat{n}_{ip}} - \frac{\frac{1}{2}\left(\nabla \left\langle P_l \right\rangle^{l} \big|_{P} + \nabla \left\langle P_l \right\rangle^{l} \big|_{nb} \right) .\vec{s}}{\vec{s}.\hat{n}_{ip}} \right] \qquad (2\text{-}72)$$

in which

$$\hat{d}_{ip} = \frac{f_{l,ip}(V_P + V_{nb})\left(\hat{n}_{ip}\right)^2}{(a_P + a_{P,nb})} \qquad (2\text{-}73)$$

When the two neighbouring control volumes are not in the same region the pressure gradient is expected to be discontinuous across these control volumes. The authors of [41] proposed an approximation for the pressure gradient at the integration point where the interface coincides the common face between two control volumes. However, in this work, since the interface between constituents does not necessarily coincide at the sides of a control volume, the pressure gradient at the cell centre is corrected, using the method that is explained in the proceeding section and then the corrected pressure gradient is used to approximate the pressure gradient in Eq. (2-72).

2.6 Pressure Gradient

It was found that the iteration method of [40] with five iterations gives the best result for pressure gradient at the cell centre. This is based on the implementation of Gauss theorem on the pressure gradient in the momentum equation:

$$\nabla P \Big|_{P} = \sum_{ip=1}^{n_{ip}} f_l \left\langle P_l \right\rangle_{ip}^{l} \hat{n}_{ip} A_{ip} \qquad (2\text{-}74)$$

where $\left\langle P_l \right\rangle_{ip}^{l}$ is calculated using interpolation.

To avoid spurious behavior of velocity field special attention must be given to ensure the pressure gradient is normal to the interface [42,43], see Appendix C. As mentioned, for the purpose of this study and the scale of the problem there is no sharp interface exists and here the interface is an imaginary line that is defined based upon the volume fraction of liquid in a C.V. The following steps are taken to correct the pressure gradients.

Let us consider that an arbitrary interface cuts through a control volume P that shares vertices with nine neighbouring control volumes, see Fig. (2-4). Knowing ∇f, normal to an imaginary interface can be calculated knowing that:

$$normal = \frac{\nabla f_l}{\left|\nabla f_l\right|} \tag{2-75}$$

The continuation of the normal intersects with the line that connects neighbouring pure fluid C.V. Then, the inverse distance approximation gives a suitable approximation for the pressure and pressure gradient at the mixed-cell center:

$$\left\langle P_l \right\rangle^l_{Corrected} = \omega \left\langle P_l \right\rangle^l_{nb_3} + \left(1-\omega\right)\left\langle P \right\rangle^l_{nb_2} \tag{2-76}$$

$$\nabla \left\langle P_l \right\rangle^l_{Corrected} = \omega \nabla \left\langle P_l \right\rangle^l_{nb_3} + \left(1-\omega\right)\nabla\left\langle P \right\rangle^l_{nb_2} \tag{2-77}$$

One should notice that this correction did not happen by solving directly the transport equations, however, it uses the pressure that has been solved by governing equation.

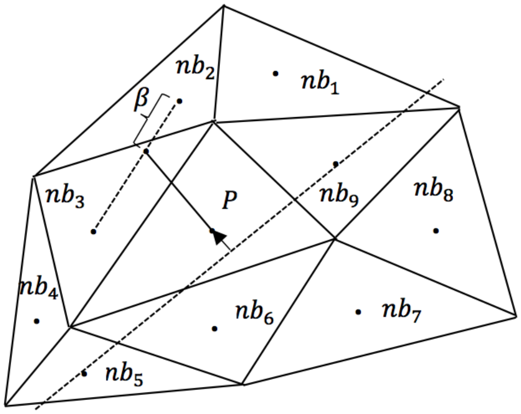

Figure 2-4: Representative portion of a triangular unstructured grid for pressure gradient correction

2.7 Source Term in the Energy Equation

The discretized form of source terms in the energy equation, Eq. (2-62) will be presented here. In general, the local liquid volume fraction depends on the nature of solidification [44]. The local volume fraction could be a function of temperature, cooling rate, speed of solidification and the rate of nucleation if the kinetics of liquid-solid transformation is such that undercooling is considerable [45,46]. In a system of multicomponent alloys, solutal transport (macrosegregation) will also influence the local liquid volume fraction field [17]. For simplification, however, it is convenient to assume the liquid volume fraction is only a function of temperature [44].

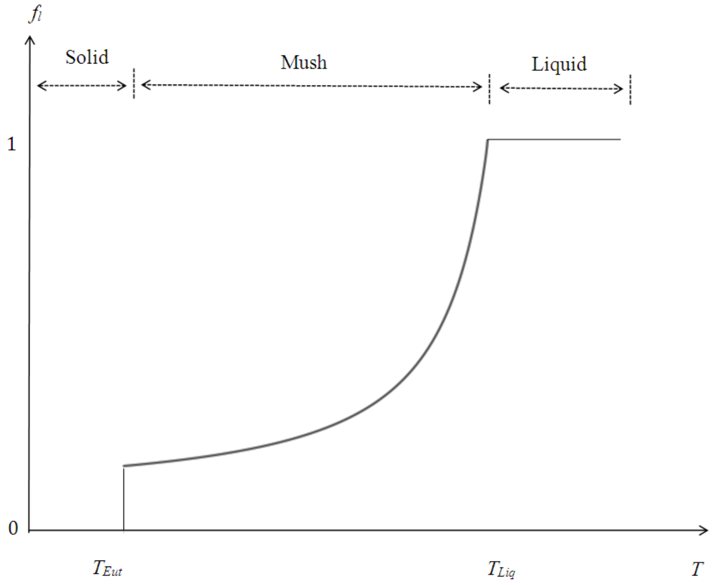

Figure 2-5: Schematic of liquid volume fraction vs. temperature

The authors of [44] demonstrated different possible forms for liquid fraction variation versus temperature functions including: linear function, linear eutectic function, power function and Scheil’s equation. In the current work, the fraction of liquid in the mushy region is estimated by Scheil’s equation, which assumes complete mixing in the liquid and no solid diffusion, [44]:

$$f_l = F(T) = \left[\frac{T - T_{mlt}}{T_{liq} - T_{mlt}} \right]^{\frac{1}{k_P - 1}} \tag{2-78}$$

where T_{mlt} is the melting temperature of the alloy, T_{liq} is the liquidus temperature and k_P is the partition coefficient. A schematic of Scheil's equation, which illustrates the liquid fraction variation versus temperature, is shown in Fig. (2-5). Regarding this graph, one may notice a temperature range associated with a non-linear change of f_l in the mushy region, a step discontinuity at the mush/solid interface that can be associated with a eutectic phase change [28], and also a step discontinuity at the mushy/liquid interface, which can be associated with undercooling at the dendrite tips [28]. Therefore, special care must be taken to account for these discontinuities.

The discretized form of the transient source term in the energy equation can be written as:

$$\frac{\delta H_P V_P}{\Delta t}\left[f_l^{new} - f_l^{old}\right] \tag{2-79}$$

in which the f_l^{new} is obtained using Taylor's series considering the fact that the volume fraction of the liquid is a function of temperature that is following Scheil's equation in the mushy zone, then,

$$f_l^{m+1} = f_l^{m} + \left.\frac{dF}{dT}\right|_{f_P^m} \times \left[T_P^{m+1} - F^{-1}\left(f_P^m\right)\right] \tag{2-80}$$

in which F^{-1} is the inverse function of *F(T)* and is evaluated at the previous iteration. It is worth mentioning that contrary to other works including [18], in this work, no under-relaxation factor is used in any of the equations.

Thus, the linearized source term in the energy equation takes the following form:

$$\frac{\delta H_P V_P}{\Delta t}\left[\left(f_P^m - f_P^{old}\right) - \left.\frac{dF}{dT}\right|_{f_P^m} \times F^{-1}\left(f_P^m\right)\right] + \frac{\delta H_P V_P}{\Delta t}\left[\left.\frac{dF}{dT}\right|_{f_P^m} \times T_P^{m+1}\right] \tag{2-81}$$

In implementing Eq. (2-85), the following logic, Eq. (2-82)– (84), is proposed to avoid oscillation in the solution.

$$f_P^{m+1} = \begin{cases} T_{mlt} < T_p^{m+1} & 1 \\ T_{Liq} < T_P^{m+1} \le T_{mlt} & 1 \\ T_{Eut} < T_P^{m+1} \le T_{liq} \quad \text{if} \begin{cases} \Delta T = T_P^{m+1} - F^{-1}(f_P^m) < -10, & \left(\dfrac{T_P^{m+1} - T_{mlt}}{T_{liq} - T_{mlt}} \right)^{\frac{1}{k_P - 1}} \\ Else & f_P^m + \dfrac{dF}{dT}\Big|^m \times \left(T_P^{m+1} - F^{-1}(f_P^m) \right) \end{cases} \\ T_P^{m+1} < T_{Eut} & 0 \end{cases} \qquad (2\text{-}82)$$

$$\frac{dF}{dT} = \begin{cases} T_{mlt} < T_p^{m+1} & 10^{-10} \\ T_{Liq} < T_P^{m+1} \le T_{mlt} & 10^{-10} \\ T_{Eut} < T_P^{m+1} \le T_{liq} & \dfrac{1}{(k_0 - 1) \times (T_{liq} - T_{mlt})} \times \left(\dfrac{T_P^{m+1} - T_{mlt}}{T_{liq} - T_{mlt}} \right)^{\frac{2 - k_P}{k_P - 1}} \end{cases} \qquad (2\text{-}83)$$

$$F^{-1}(f_P^m) = \begin{cases} T_{mlt} < T_p^{m+1} & \mathrm{T}_P^m \\ T_{Liq} < T_P^{m+1} \le T_{mlt} & \mathrm{T}_P^m \\ T_{Eut} < T_P^{m+1} \le T_{liq} & \mathrm{T}_{mlt} + (T_{liq} - T_{mlt}) \times (f_P^m)^{(k_P - 1)} \\ T_P^{m+1} < T_{Eut} & \mathrm{T}_P^m \end{cases} \qquad (2\text{-}84)$$

2.8 Solution

Now that all terms in the governing equations are fully discretized one can construct the solution matrix for the algebraic equation in the form of Eq. (2-63), see appendix D. In this work, the linear algebraic equation was solved using version 3.3 of the Portable, Extensible Toolkit for Scientific Computation (PETSc) solver on the Shared Hierarchical Academic Research Computing Network (SHARCNET).

2.9 The Wedge Casting

The mechanical properties of Mg-Al alloys are strongly affected by the obtained microstructure. Grain size can be controlled by process parameters such as cooling rate during the casting process and is one of the microstructural features that strongly influence the mechanical properties of all polycrystalline materials, particularly, Mg-Al alloys. Relationships such as Hall-Petch [47,48] suggest that generally a smaller grain size leads to higher yield strength. Grain boundaries impede dislocation motion; therefore, they contribute to strengthening, whose magnitude depends upon the structure of the grain boundaries and the degree of misorientation between grains [49]. In dendritic structures secondary dendrite arm spacing (SDAS) has a similar influence on the mechanical properties as the grain size. Herein, a case study is chosen to emphasize that the information facilitated by the cooling curve during a solidification process is of great importance and can be used for predicting microstructural features such as local SDAS or grain size.

The wedge casting is a unique case study that is able to produce various cooling rates from the lower tip to the top and hence, different microstructure can be obtained. In this case, a finer grain size microstructure is obtained closer to the tip due to the higher rate of cooling. Experiments reported previously in [50] have been simulated herein to demonstrate the viability of the present formulation and computational framework.

2.9.1 Numerical Set up

A wedge-shaped casting, AM60B with physical properties indicated in Table 1 is simulated. Due to the fact that the geometry under consideration is symmetrical, only half of the domain is considered. Figure (2-6) shows the dimensions of the computational domain and a sample of the grid used.

A convective boundary condition is applied at the top of the half wedge. An ambient temperature of 298 K and a convection coefficient of 10 W/m^2K are used, combined with a slip condition on velocity to approximate the natural convection at this surface. For the side wall, extensive studies have been done previously to estimate the boundary condition for a mold-metal interface through experimental and numerical calibration [52-54].

Table 2-1: Properties of AM60B (units are shown in the nomenclature)[51]

Average Density ρ	2483	Equilibrium Partition Coefficient k_p	0.1875
Liquid Specific Heat Cp_l	1097	Thermal Expansion β	2.3×10^{-5}
Solid Specific Heat Cp_s	992	Melting Temperature T_{mlt}	923
Latent Heat of Fusion L_{ls}	396	Liquidus Temperature T_{liq}	892
Liquid Thermal Conductivity K_l	92.6	Solidus Temperature T_{sol}	796
Solid Thermal Conductivity K_s	130	Liquid Viscosity μ_l	0.0013

Herein, since we are most interested in the performance of the computational framework, on the side wall, where mold and metal are in contact, two different conditions are considered to attempt to replicate the water-cooling condition at this edge. First, a constant temperature of 423 K and a constant convection coefficient of h= 5000 W/m^{2}K are used, combined with no-slip zero-penetration conditions on velocity. Temperature and convective heat transfer coefficients on the side wall are typical conditions used for water cooling. The second condition uses the same constant temperature (423 K) and velocity conditions, but instead of imposing a constant heat transfer coefficient, the experimental result of [52] and [54], in which $h(t)=240+2150\times\exp(-t/14.5)$, is considered to partially account for the transient boundary condition on the side wall.

A symmetry condition is imposed on the left (vertical) edge of the domain. A grid-independence study was done based upon the total percentage of solid in the domain at a certain time during the process. 1497 triangular volumes were used to discretize the half domain, producing results that are grid-independent to within 1.9%. Grids of 856 and 3388 volumes were also run producing results of lower, and much higher accuracy. The 1497-cell case is presented here as it yields results of sufficient accuracy while also demonstrating the robustness of the code for a relatively coarse grid; something which is often required in more geometrically complex applications.

For the permeability coefficient in the Darcy term, different values and methods are previously reported [21,32] in the literature, either based on the fact that these values caused a better stability in the solution or based upon the physics that were involved in the problem. The correct value for a constant permeability for the purpose of this study, or any other similar study, is a value close to the average SDAS for the particular alloy of interest. Herein, $100\mu m$ is used as the permeability coefficient.

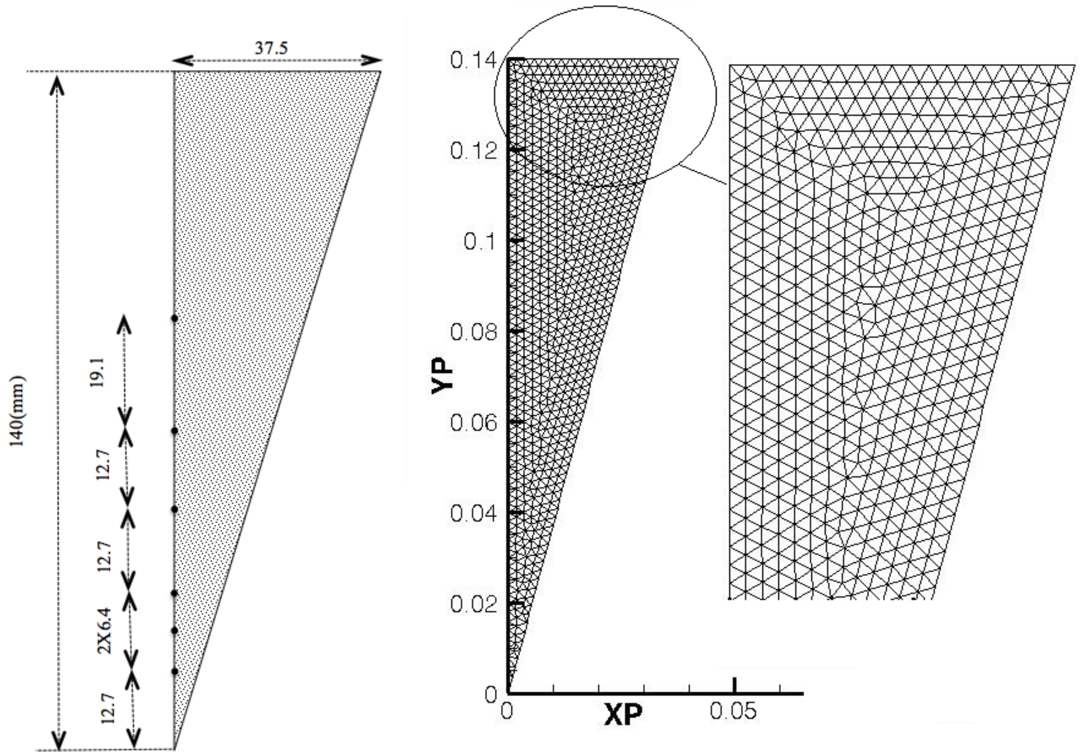

Figure 2-6: Half of the wedge-shaped casting with six thermocouples embedded at the centerline (left), Unstructured triangular mesh (right)

2.9.2 Numerical Study of Wedge Casting

A time step size of five milliseconds was required to properly capture the physics of the solidification process. A further reduction in time-step size produced results that were not significantly different. Convergence of the linearization loop occurred when the maximum normalized residual was reduced to below the value 10^{-6}. The computation was performed on SHARCNET using a single Intel Xeon 2.83 GHz CPU with 16 GB memory/node. The elapsed CPU time was 4.4 hours and the code required 2.9 GB virtual memory. The wall time was determined to be approximately 4.8 hours.

Figure (2-7) shows the convergence characteristic of the energy equation for 0.1s (20 time steps) and for the linearization loop at two different times during the solidification, t=10s and 20s. While the linearization loop required as many as 15 iterations per time-step early in the transient, full convergence typically required fewer than 8 iterations, as shown in Fig. (2-7). These plots clearly indicate that, contrary to other previous works [55,56], the solution converges smoothly and rapidly without any oscillations.

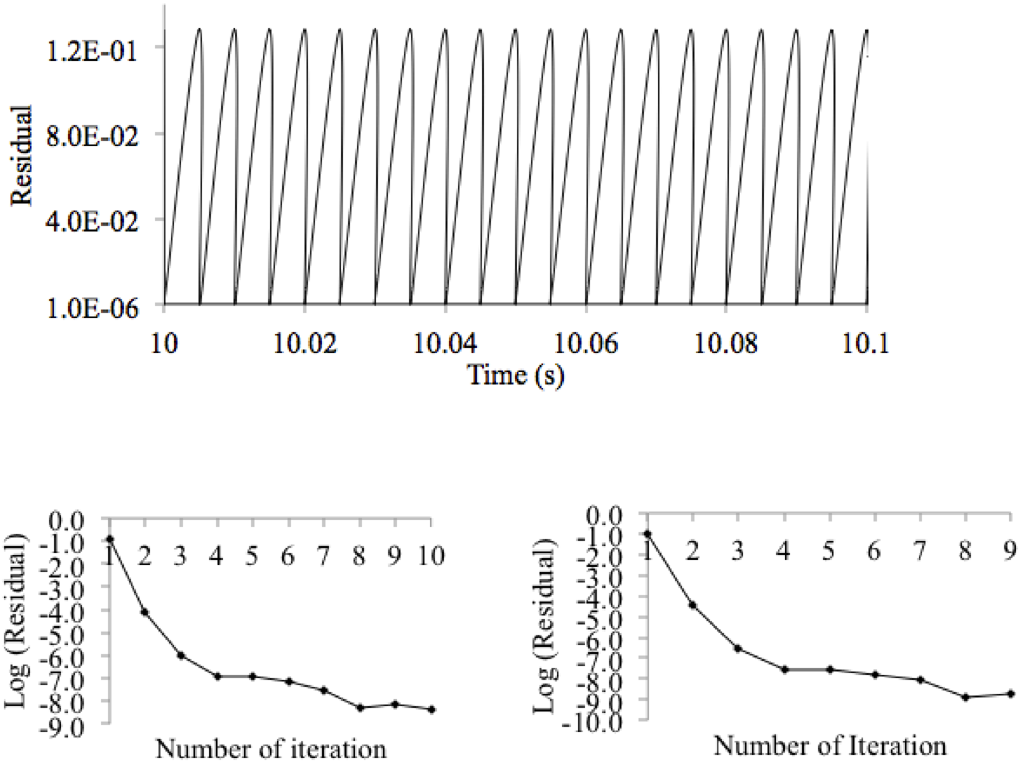

Figure 2-7: (top), Residual history of simulation for 0.1s, (bottom left) the residual for t=10(s), (bottom right) the residual for t=20(s)

Figure (2-8) shows contours of solid fraction (left of symmetry) and temperature (right of symmetry) for several times during the transient process. As expected, the plots show clearly the rapid cooling at the lower tip followed by the more gradual cooling that occurs in the wide part of the casting. The plots also show the connection between the temperature and the motion of the solidification front. The region close to the tip solidifies at the early stage of simulation due to the higher cooling rate while the rest of the domain requires a longer time to fully solidify. Solid, mushy and liquid regions are indicated in the figure.

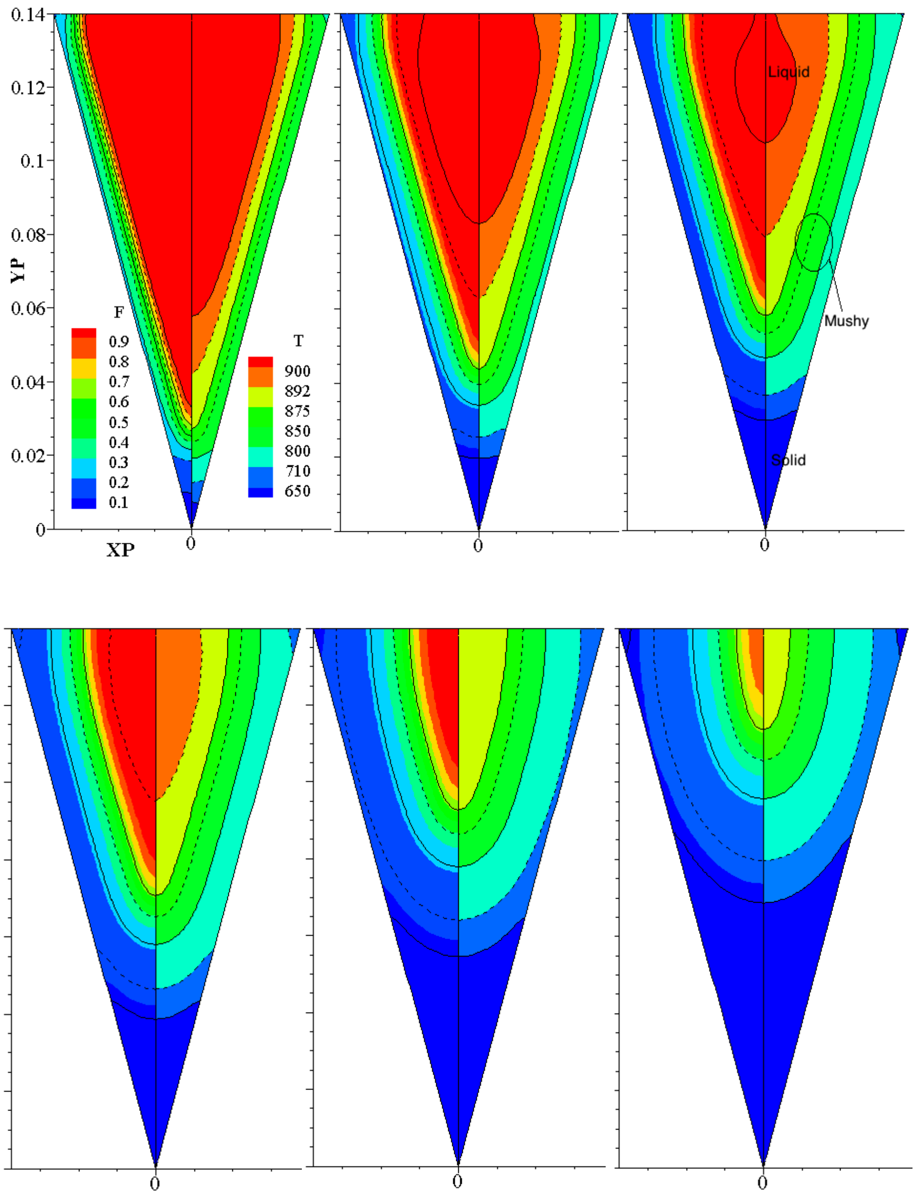

Figure 2-8: Contours of solid fraction (left of symmetry) and temperature (right of symmetry) for t=2.5,5,7.5,10,15 and 20 (s), top left to bottom right, respectively

Figure (2-9) shows contours of solid fraction with velocity vectors at 7.5 s. The velocity vector profile at height y=120 mm is also superimposed in the figure to show the structure of the velocity field. The figure shows the direction of flow in the mushy zone and molten alloy, which clearly shows the occurrence of convection during the process. As the molten metal solidifies in the tip region, the thermal convection creates a roll shaped velocity field that moves towards the top of the domain and disappears when the molten metal is fully solidified.

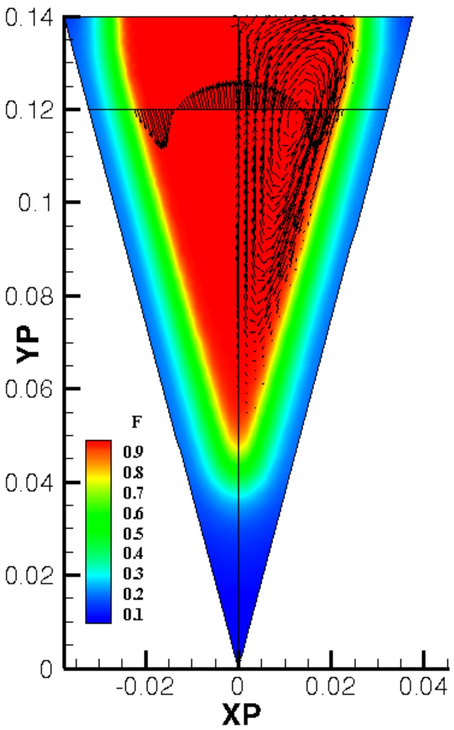

Figure 2-9: Contours of solid fraction and velocity field at a cross section at t=7.5(s)

Cooling curves at three of six thermocouples along the vertical centerline of the wedge casting for both boundary conditions at the side wall with constant and transient convective heat transfer coefficient are shown in Fig. (2-10) and Fig. (2-11), respectively. As can be seen, the predicted cooling rate decreases with increasing distance from the tip. Also, experimental data reported in [50] were used to compare cooling curves for the same three thermocouples, Fig. (2-10) and Fig. (2-11), in which a decrease of cooling rate from tip to the top of the geometry can be observed. The predictions from our in-house code using the transient convective heat transfer condition at the mold-metal interface are seen to yield better cooling curves that have the same trend as the experimental results. The discrepancy between the process time in the computational and experimental results is due to the fact that in our simulation the filling process is not considered; instead, the domain is assumed to be fully filled with molten alloy at t=0 s. For the experimental data, the initial time for solidification was considered to be 5.75 (s) to avoid depicting the temperature history during the filling process. Also, although two different thermal boundary conditions are considered for the side wall, the imposed thermal boundary conditions are still different from what occurs in the real casting process and experimental calibration is required. This is one of the main reasons for not attaining the exact cooling curves as the experimental result. Specifically, the existence of a thin gap between mold and metal, and also the increase of the mold temperature over time both play important roles in the cooling process.

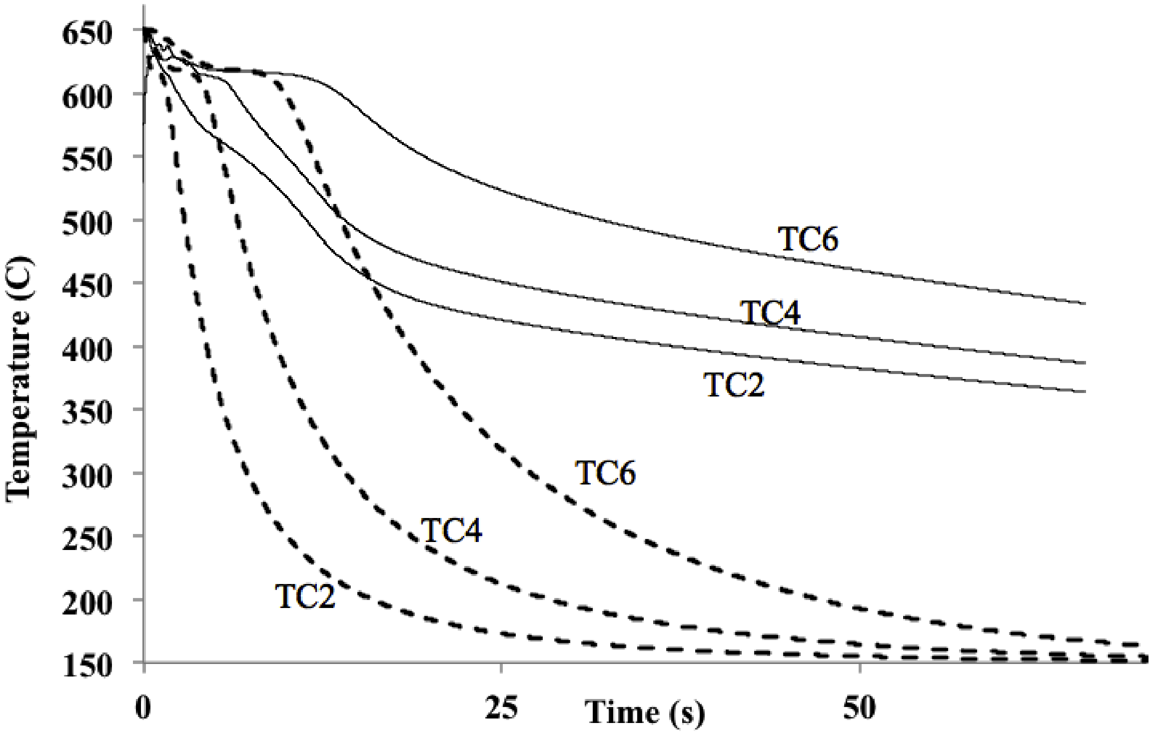

Figure 2-10: Comparison of the experimental cooling curves (solid line) and predicted cooling curves (dashed line) with constant h for AM60B at three different thermocouples, (TC#2, 4 and 6)

On the predicted cooling curves in Fig. (2-11), one may notice that at the liquidus temperature, 892 K (619 C) the molten alloy starts solidifying until it reaches the eutectic temperature 710 K (437 C) where all the liquid is converted into solid. Based upon the experimental cooling curves, the liquidus and solidus temperatures are observed to be at approximately 892 K (619 C) and 796 K (523 C), respectively.

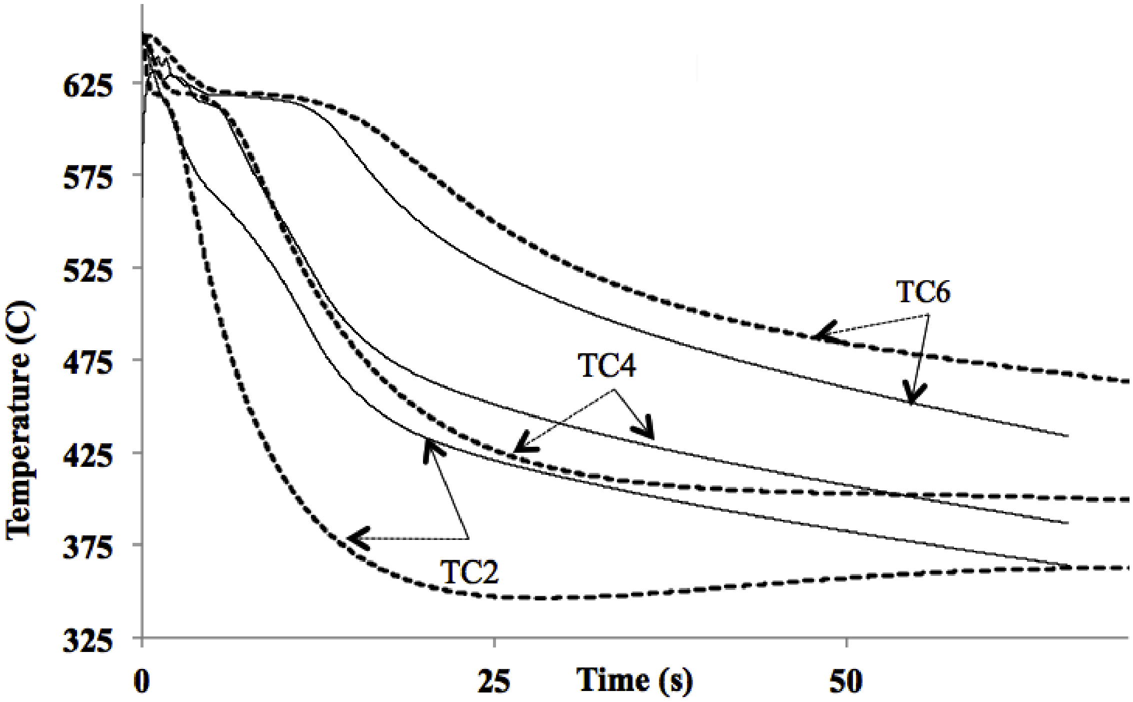

Figure 2-11: Comparison of the experimental cooling curves (solid line) and predicted cooling curves (dashed line) with transient h for AM60B at three different thermocouples (TC#2, 4 and 6)

One should notice that selecting the partition coefficient plays an important role in defining the freezing range and local solidification time. From the phase diagram shown in Fig. (2-12) the critical (equilibrium) partition coefficient, k_p, for AM60B is 0.1875, which is shown by solidus line A. In deriving Scheil's equation, a complete mixing of solute in the liquid and no diffusion of solute in the solid is assumed. This results in a steeper solidus line, i.e. line B, and a partition coefficient smaller than the critical value. If one considers a partition coefficient of 0.1, for such condition, the freezing range is the difference between liquidus and eutectic temperature. For any values greater than this value, the freezing range can be obtained from the phase diagram.

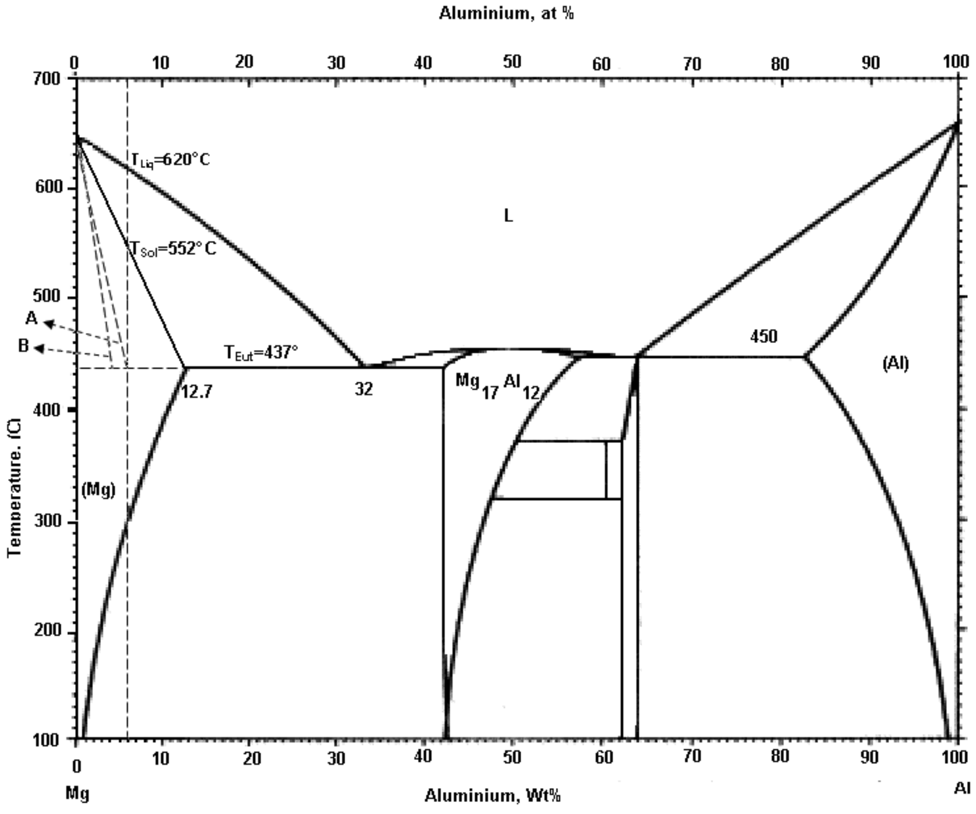

Figure 2-12: Mg-Al binary phase diagram, dashed line A and B, respectively, represent the solidus line corresponding to the critical partition coefficient and a value smaller than critical value

Knowing that the solidus temperature from the experiment is at about 796 K, means that the experiment is performed in such a way that the partition coefficient has a value greater than the critical value. Assuming that the liquidus line is a straight line on the phase diagram, using the experimental solidus temperature will result in a partition coefficient equal to 0.3165, which results in a solidification process closer to the equilibrium conditions.

2.9.3 Grain Size

Obtaining the cooling curves at different thermocouples and knowing the local solidification time at each thermocouple provides enough information for estimating SDAS or the grain size. Several analytical models that are reviewed in [50] have been developed to predict the grain size based upon the local solidification time. Most of them use an exponential correlation to obtain the SDAS or the grain size, G.S:

$$G.S = Ct_s^n \tag{2-85}$$

in which C is a constant and *n* is an exponent that is usually determined to be in the range of 0.25 to 0.5.

Table 2-2 Experimental [50] and numerical data for the local solidification time, grain size and percentage error at six thermocouples

#TC	Location (mm)	Experimental t_s (s)	Grain Size (μm) (Experiment)	Numerical t_s (s)	Grain Size (μm) (Numerical)	Grain Size Error %
1	13	9.95	5.45	2.71	6.31	13.6
2	19	8.24	5.93	3.88	6.67	11.1
3	26	7.41	7.06	4.73	6.88	2.53
4	37	8.53	7.93	8.79	7.58	4.66
5	51	12.7	7.31	11.7	7.93	7.73
6	69	20.6	8.58	24.4	8.89	3.45

Author of [50] experimentally showed that the exponent for the AM60B in a wedge casting would not fit this range. From Table 2-2, ignoring the data for the first two thermocouples that are closer to the tip and are under influence of the filling process then the best fit to their experimental data is

$$G.S = 5.40t_s^{0.156} \tag{2-86}$$

Figure (2-13) shows a comparison of the grain size estimated from Eq. (2-86) at the six thermocouple positions indicated in Fig. 6, using cooling times, t_s, obtained from the transient simulations of the wedge casting and considering the transient convective heat transfer in the thermal boundary condition of the side wall. The grain size is seen to increase for thermocouples further from the lower tip of the casting, as expected. Although there is still a discrepancy between the numerical and experimental work for all the thermocouples, a sudden decrease in the experimental measurement of grain size at the fifth thermocouple is more noticeable. It is worth mentioning that since the main reason for the unexpected experimental grain size at the fifth thermocouple in the experimental work of [50] is not explicitly stated, in this work the data for this thermocouple is not considered.

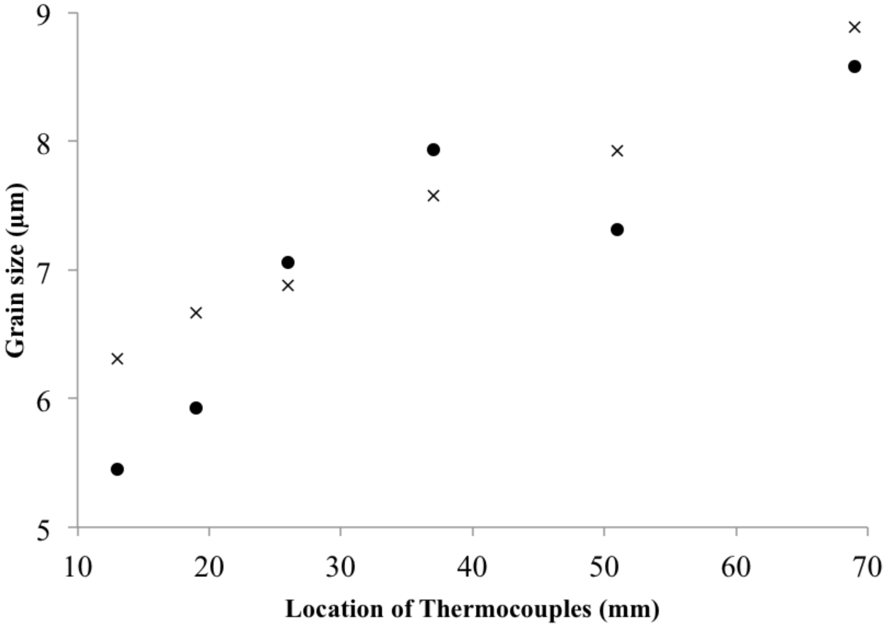

Figure 2-13: Comparison of the experimental [50] grain size values, (●), and values obtained from Eq. (2-86), (×)

2.10 Summary

In the present work, a general single region volume averaged finite volume formulation has been presented and tested for the solidification of a commercially available magnesium alloy.

The main difference in the derived momentum equation as compared to previously published momentum equations is an additional sink term resulting from the assumption of non-zero gradient of solid fraction. Although this assumption is necessary to make in the derivation of conservative equations for solidification of binary alloys, the extra term will only have a noticeable effect on the velocity field for cases where convection is strong.

The discretization of the equations was carried out for a general unstructured grid using the most modern existing approaches. However, to obtain a correct velocity field in the mushy zone and in control volumes adjacent to mixed control volumes, a special treatment of the pressure gradient is proposed. The special momentum proposed by [37] was modified to take the effect of non-zero solid fraction gradient into account.

In casting and discretization of the energy equation, a unique derivation approach was chosen that results in a stable temperature-based energy equation with all the essential terms that must be considered in the alloy solidification. For the evolution of solid fraction, contrary to previously published work, no under-over relaxation was considered, yet a smooth, rapid convergence of the temperature field was achieved without oscillation.

The proposed formulation was tested for a wedge-shaped AM60B alloy to predict the cooling rates and grain size at six embedded thermocouples, with results compared against previously reported experimental results. While the results of the numerical model agrees with the experimental data, a better understanding of the boundary condition that existed during the experiment would result in a more agreeable result.

It is concluded that the formulation and the numerical treatment presented herein is capable of capturing all of the essential features of the solidification process and, therefore, an excellent framework for providing information required to estimate local mechanical properties of die-cast components.

2.11 References

[1] A North American strategic vision for auto weight reduction, US auto partnership report, 2005

[2] W. Oldfield, Transaction for American Society for Metals, vol.59, pp.945-959, 1966

[3] L. Nastac and D.M. Stefanescu, Macrotransport- solidification kinetics modeling of equiaxed dendritic growth: Part I. Model development and discussion, Metallurgical Transactions A, vol.27A, pp. 4075-4083, 1996

[4] Ph. Thevoz, J.L. Desbiolles and M. Rappaz, Modeling of equiaxed microstructure formation in casting, Mettallurgical Transaction A, vol.20.2, pp.311-322, 1989

[5] D. DasGupta, S. Basu and S. Chakraborty, Effective property predictions in multi-scale solidification modeling using homogenization theory, Physical Letters A, vol.348, pp.386-396, 2006

[6] R.N. Hills, D.E. Loper and P.H. Roberts, A thermodynamically consistent model of mushy zone, The Quarterly Journal of Mechanics and Applied Mathematics, vol.36, pp. 505-538, 1983

[7] V.C. Prantil and P.R.Dawson, Application of a mixture theory to continuous casting, in: M.M. Chen, J. Mazumder and C.L. Tucker III (Eds.) Transport phenomena in materials processing, ASME, New York, pp.469-484, 1983

[8] W.D. Bennon and F.P. Incropera, A continuum model for momentum heat and species transport in binary solid-liquid phase change systems-II; Application to solidification in a rectangular cavity, International Journal of Heat and Mass Transfer, vol.30, pp.2171-2187, 1987

[9] S.V. Patankar, Numerical Heat Transfer and Fluid Flow, Hemisphere, New York, 1980

[10] W.G. Gray, A derivation of the equations for multi-phase transport, Chemical Engineering Science, vol.30, pp.229-233, 1975

[11] M. Hassanizadeh and W.G. Gray, General conservation equations for multi-phase systems: 1. Averaging procedure advances in water resources, vol.2, pp.131-144, 1979

[12] S.Whitaker, Volume averaging of transport equations, in: P.D. Plessis, Fluid Transport in Porous Media, Taylor & Francis, Billerica, MA, USA, 1999

[13] J. Ni and C. Beckermann, A volume-averaged two phase model for transport phenomena during solidification, Metallurgical Transactions B, vol.22B, pp. 349-361, 1991

[14] C. Beckermann and R. Viskanta, Mathematical modeling of transport phenomena during alloy solidification, Applied Mechanics Reviews, vol.46, pp.1-27, 1993

[15] S. Ganesan and D.R. Poirier, Solute redistribution in dendritic solidification with diffusion in the solid, Journal of Crystal Growth, vol.97, (3-4), pp.851-859, 1989

[16] P.J. Prescott, F.P. Incropera and W.D. Bennon, Modeling of dendritic solidification systems: Reassessment of the continuum momentum equation, International Journal of Heat and Mass Transfer, vol.34, (9), pp.2351-2359, 1991

[17] V.R. Voller, A.D. Brent and C. Prakash, The modeling of heat, mass and solute transport in solidification systems, International Journal of Heat and Mass Transfer, vol.32, (9), pp.1719-1731, 1989

[18] V.R. Voller and C.R. Swaminathan, General source based method for solidification phase change, Numerical Heat Transfer, Part B, vol.19, pp.175-189, 1991

[19] C.R. Swaminathan and V.R. Voller, A general enthalpy method for modeling solidification processes, Metallurgical Transactions B, vol.23B, pp.651-664, 1992

[20] N. Zabaras and D. Samantha, A stabilized volume-averaging finite element method for flow in porous media and binary alloy solidification processes, International Journal for Numerical methods in Engineering, vol.6, (5), pp.1-38, 2004

[21] V.R. Voller and C. Prakash, A fixed grid numerical modeling methodology for convection-diffusion mushy region phase-change problems, International Journal of Heat and Mass Transfer, vol.30, (8), pp.1709-1719, 1987

[22] C. Beckermann and R. Viskanta, Double-diffusive convection during dendritic solidification of a binary mixture, Physico Chemical Hydrodynamics, vol.10, (2), pp.195-213, 1988

[23] J. S. Hsiao, An efficient algorithm for finite difference analyses of heat transfer with melting and solidification, Numerical Heat Transfer, vol.8, pp. 653-666, 1985

[24] D. Celentano, M. Cruchaga, N. Moraga, and J. Fuentes, Modeling natural convection with solidification in mold cavities, Numerical Heat Transfer, Part A, vol.39, pp.631-654, 2001

[25] M. Salcudean, and Z. Abdullah, On the numerical modeling of heat transfer during solidification process, International Journal for Numerical Methods in Engineering, vol.25, pp.445-473, 1988

[26] D. Poirier and M. Salcudean, On numerical methods used in mathematical modeling of phase change in liquid metals, Master of Applied Science thesis, University of Ottawa, ON, 1986

[27] V.R. Voller, M. Cross and P.G. Walton, in: R.W. Lewis and K. Morgan (Eds.), Numerical methods in thermal problems, Pineridge, Press Swansea, p.172, 1979

[28] V.R. Voller, C.R. Swaminathan and B.G. Thomas, Fixed grid techniques for phase change problems: a review, International Journal for Numerical Methods in Engineering, vol.30, pp.875-898, 1990

[29] F.A. Howes and S. Whitaker, The spatial averaging theorem revisited, Chemical Engineering Science, vol.40, pp.1387-1392, 1985

[30] S. Whitaker, A simple geometrical derivation of the spatial averaging theorem, Chemical Engineering, vol.19, pp.18-21, 50-52, 1985

[31] H. Tennekes and J.L. Lumley, A first course in turbulence, MIT Press, Cambridge, Massachusetts, 1972

[32] D. R. Poirier, Permeability for flow of interdendritic liquid in columnar-dendritic alloys, Metallurgical and Materials Transactions B, vol.18b, pp.245-256, 1987

[33] M. Kaviani, Principles of Heat Transfer in Porous Media, second ed., Springer New York, pp.119-139, 1995

[34] S.L. Soo, Particulates and Continuum, Hemisphere Publishing Corp., New York, 1974

[35] A.D. Brent, V. R. Voller and K.J. Reid, Enthalpy-porosity technique for modeling convection-diffusion phase change: application to the melting of a pure metal, Numerical Heat Transfer, vol.13, pp.297-318, 1988

[36] C.R. Swaminathan and V.R. Voller, On the enthalpy method, International Journal of Numerical Methods in Heat and Fluid Flow, vol.3, pp.233-244, 1993

[37] C. M. Rhie and W.L. Chow, Numerical study of the turbulent flow past an airfoil with trailing edge separation, American Institute of Aeronautics and Astronautics Journal, vol.21, pp.1525-1532, 1983

[38] PK. Kholsa and SG. Rubin, A diagonally dominant second order accurate implicit scheme, Computers and Fluids, vol.2, pp.207-209, 1974

[39] L. Betchen, A. Straatman, An accurate gradient and Hessian reconstruction method for cell-centred FV discretization on general unstructured grids, International Journal for Numerical Methods In Fluids, vol.62, pp.945-962, 2009

[40] S.A. Karimian and A. Straatman, Discretization and parallel performance of an unstructured finite volume Navier Stokes solver, International Journal for Numerical Methods In Fluids, vol.52, pp.591-615, 2006

[41] C. DeGroot and A. Straatman, A FVM for fluid flow and nonequilibrium heat transfer in conjugate fluid/porous domains using general unstructured grids, Numerical Heat Transfer, Part B, vol.60, pp.1-26, 2011

[42] M. Farrokhnejad, A.G. Straatman, J. Wood, A Volume-of-Fluid Based Numerical Simulation of Solidification in Binary Alloys on Fixed Non-uniform Co-located grids, ASME International Manufacturing Science and Engineering, USA, West Lafayette, IN, pp. 427-436, 2009

[43] M. Farrokhnejad, A.G. Straatman, Advances on a VOF Based Numerical Simulation of Mg Die-Casting Process on a General Unstructured Grid. 9th International Conference on Mg Alloys & Their Applications, Vancouver, Canada, 2012

[44] V. R. Voller and C. R. Swaminathan, Earl Source-Based Method for solidification phase change, Numerical Heat Transfer, Part B: Fundamentals, vol.19, pp.175-189, 1991

[45] M. Rappaz, Modeling of microstructure formation in solidification process, International Materials Review, vol.34, pp.93-123, 1989

[46] D. M. Stefanescu and C. S. Kanetkar, Modeling microstructural evolution of eutectic cast iron and of the gray/white transition, Material science and Engineering, vol.95, pp.139-144, 1987

[47] E.O. Hall, The Deformation and aging of mild steel III, Proceeding of Physical Society, vol.64B, pp.747-753, 1951

[48] N.J. Petch, The cleavage strength of polycrystals, Journal of Iron and Steel Institute, vol.174, p.25, 1953

[49] D.J. Lloyd and S.A. Court, Influence of grain size on tensile properties of Al-Mg alloys, Material Science and Technology, vol.19, pp.1349-1354, 2003

[50] I. Basu, Effect of process variables on the microstructural features for as-cast magnesium alloys, ME.Sc Thesis, The University of Western Ontario, London, Ontario, 2011

[51] C.J. Vreeman and F.P. Incropera, The effect of free-floating dendrites and convection on macrosegregation in direct chill cast aluminum alloys: Part II: Predictions for Al-Cu and Al-Mg alloys, International Journal of Heat and Mass Transfer, vol.43, pp.687-704, 2000

[52] M. Trovant and S. Argyropoulos, Finding boundary conditions: A coupling Strategy for the modelling of metal casting processes: Part I. Experimental study and correlation development, Metallurgical and Materials transaction B, vol. 31B, pp.75-86, 2000

[53] Y. Nishida, W. Droste and S. Engler, The air gap formation process at the casting-mold interface and the heat transfer mechanism through the gap, Metallurgical Transaction B, vol. 17B, pp.883-844, 1986

[54] Y. He, A. Javaid, E. Essadiqi and M. Shehata, Numerical simulation and experimental study of the solidification of a wedge-shaped AZ31 Mg alloy casting, Canadian Metallurgical Quarterly, vol.48, pp. 145-156, 2009

[55] W.D. Rolph III and K.J. Bathe, An efficient algorithm for analysis of non-linear heat transfer with phase changes. International Journal for Numerical Methods in Engineering, vol.18, pp.119-134, 1982

[56] G.Comini, S. Del Giudice and O. Saro, A conservative algorithm for multidimensional conduction phase change. International Journal for Numerical Methods in Engineering vol.30 pp. 1191-1195, 1990

Chapter 3

3 Numerical Simulation of Solidification and Prediction of Mechanical Properties in Magnesium Alloy Casting

3.1 Introduction and Literature Review

Die-casting of Magnesium-Aluminum (Mg-Al) alloys results in varying casting features, which in turn, lead to strength and performance variation throughout different regions in the casting. These variations in mechanical properties are mostly influenced by microstructural features and defects, which develop during the filling and solidification process. Understanding the process of casting could help us to better understand the microstructure and, hence, the performance of the product would be more predictable.

Computational tools not only provide assistance for a faster understanding of these variations but also shorten the prototyping sequence for newly developed alloys, and improve the die designs. Microstructural features such as average grain size, amount and distribution of porosity and tensile-compression asymmetry of the Mg-Al alloys strongly affect the mechanical properties of these alloys. In this study grain size effects are investigated. Grain size can be controlled by process parameters such as cooling rate during the casting process and is one of the microstructural features that strongly influences the mechanical properties, particularly, the yield strength of Mg-Al alloys [1].

Typically, the solidification front in Mg castings proceeds from the die walls, where there is a large temperature gradient and towards the centre of the casting [2]. This results in the formation of finer grains closer to the die walls and coarser grains toward the centerline with lower cooling rates [3]. For AM60B, variations of grain size of about 7 μm close to the die walls to 17 μm in the central region have been reported previously [2,3]. Relationships such as Hall-Petch suggest that generally a smaller grain size leads to a higher yield or flow stress [4,5]:

$$\sigma = \sigma_0 + kd^{-1/2} \tag{3-1}$$

Grain boundaries impede dislocation motion; therefore, they contribute to strengthening whose magnitude depends upon the structure of the grain boundaries and the degree of misorientation between grains [1]. Extensive studies have been carried out to examine the validity of the Hall-Petch relationship for various Mg alloys [3,6-10]. For an AZ91 magnesium alloy, it was found that the Hall-Petch relationship is valid [6], while for a Mg-3wt% Zn alloy the value of k in the Hall-Petch equation was found to depend upon the testing temperature [10]. For AM60B the value of k and σ_0 in the Hall-Petch equation was reported [11] to be 297 $MPa.\mu m^{-1/2}$ and 24 MPa, respectively. These values were obtained using spherical indentation techniques.

It is well-known that in the process of Mg die-casting, variation in grain size are produced not only in different locations of the casting, but also across the thickness of the casting [8]. The result of these variations in grain size is the formation of regions that are called skin and core. The skin region is usually free of defects whereas the core region contains defects such as porosity. From the grain size point of view, regions of fine-grained microstructure are called skin and those with coarser grain size are called core regions. Several definitions of the skin thickness in terms of hardness profile, porosity fraction and its influence on the mechanical properties of Mg-Al alloys have been explored previously [8-15]. It was reported that [12] in a full thickness of an AZ91, by removing 125 μm, about 25% of the casting thickness, from the surface of a 1mm wide tensile sample, the yield strength drops from 186 MPa to 160 MPa. In particular, the author of [8] performed experiments for AM60B die-cast by machining part of the skin region. In [8] the results and influence of the skin thickness analysis on the yield strength of the AM60B die-cast component was compared to the grain size measurement of [13] and showed that removing the skin thickness permits for setting of a lower bound on the ductility of the casting, resulting in an approximately 15MPa lower yield strength than that for the as-cast samples.

The author of [13] found that the average grain size varies from 5 to 9 μm in the skin region and from 12 to 15 μm in the core region, however, the transition from skin to core was determined by a grain size threshold value of about 10 μm [8]. In addition, it was found that the average grain size is only consistent through the skin region, and then increases into the core region [8]. Hence, a modified Hall-Petch equation in which the variation of skin thickness is taken into account was proposed and validated experimentally by [8] to calculate the average yield strength for the sample from the yield strength determined from each field of measurement of the grain size across the sample thickness:

$$\sigma = \sum \delta_t \left(\sigma_0 + kd^{-1/2} \right) \tag{3-2}$$

where δ_t is the fraction of the thickness of the field of measurement to the sample thickness. In this study, the thresholds and correlations obtained by [8] are used to measure the skin thickness as well as the average yield strength.

Obtaining the cooling curves at different thermocouples and knowing the local solidification time at each thermocouple provides enough information for estimating SDAS or the grain size. Several analytical models that are reviewed in [16] have been developed to predict the grain size based upon the local solidification time. Most of them use an exponential correlation to obtain the SDAS or the grain size, G.S:

$$G.S = Ct_s^n \tag{3-3}$$

in which C is a constant and n is an exponent that is usually determined to be in the range of 0.25 to 0.5. t_s is the local solidification time and that is the time elapsed in the freezing range. The author of [16] experimentally showed that the exponent for the AM60B in a wedge casting would not fit this range. The best fit to their experimental data is through the following correlation:

$$G.S = 5.40t_s^{0.156} \tag{3-4}$$

Another common approach of predicting the grain size is using the local cooling rate [17-19]. Higher cooling rates lead to a shorter solidification time and, consequently, finer grain size. Recently [19], using a numerical study, the grain size for a high-pressure die-casting (HPDC) AM60B was estimated by:

$$G.S = 59R^{-0.303} \tag{3-5}$$

In this study, both correlations, Eq. (3-4) and Eq. (3-5), will be used and the results will be compared.

In the remainder of this paper, the formulation developed in [20] is used. The formulation was previously tested to compare the predicted cooling curves in a wedge-shaped magnesium alloy with the previously reported experimental result [20] and the detail of derivation is not repeated. Then, the aforementioned experimental correlations are implemented into our in-house code to predict the local grain size and average yield strength for a wedge- shaped AM60B alloy. These results are discussed and compared to the previously reported experimental work.

3.2 Mathematical Formulation

3.2.1 Governing Equations

The microscopic mass, momentum and energy equations for a medium consisting of phase that is going under phase change is given by:

$$\frac{\partial \rho_k}{\partial t} + \nabla \bullet \left(\rho_k \vec{v}_k\right) = 0 \tag{3-6}$$

$$\frac{\partial}{\partial t}\left(\rho_k \vec{v}_k\right) + \nabla \bullet \left(\rho_k \vec{v}_k \vec{v}_k\right) = -\nabla P_k + \mu_k \nabla \bullet \nabla \vec{v}_k + \rho_k \vec{b} \tag{3-7}$$

$$\frac{\partial}{\partial t}\left(\rho_k h_k\right) + \nabla \bullet \left(\rho_k h_k \vec{v}_k\right) = \nabla \bullet k_k \nabla T_k \tag{3-8}$$

for the k^{th} phase.

Assuming that the variation of material properties occurs globally and not within the dV_k, i.e. $\left\langle \rho_k \right\rangle^k = \rho_k$ and also ignoring the effect of shrinkage and density variation, the intrinsic form of continuity equation can be written as:

$$\rho_k \nabla \bullet \left[f_k \left\langle \vec{v}_k \right\rangle^k \right] = 0 \tag{3-9}$$

The extrinsic form of momentum equation is more desirable, and can be written as [20]:

$$\begin{aligned} \rho_k \left[\frac{\partial \left\langle \vec{v}_k \right\rangle}{\partial t} + \frac{1}{f_k} \nabla \bullet \left(\left\langle \vec{v}_k \right\rangle \left\langle \vec{v}_k \right\rangle \right) \right] &= -f_k \nabla \left\langle P_k \right\rangle^k + \mu_k \nabla \bullet \nabla \left\langle \vec{v}_k \right\rangle - \\ \frac{f_f \mu_f}{K} \left\langle \vec{v}_k \right\rangle - \frac{\mu_k}{f_k} \nabla f_k \left(\nabla \left\langle \vec{v}_k \right\rangle \right) + \rho_k f_k \left\langle \vec{b} \right\rangle \end{aligned} \tag{3-10}$$

where the value of the K, permeability in the Darcy term can be approximated using the Kozeny-Carman equation:

$$K = \frac{\kappa f_l^3}{(1 - f_l)^2} \tag{3-11}$$

The value of κ depends on the size of the secondary dendrite arm spacing (SDAS) and morphology of the mushy region. This term has no effect on the momentum equation when it deals with pure liquid regions, while it is infinity in the pure solid regions. Density is assumed to be constant, except in the buoyancy term. The buoyancy effects are modeled using Boussinesq approximation:

$$\rho_k f_k \vec{b} = \rho f_k \vec{g} \beta \left(\left\langle T \right\rangle - T_{ref} \right) \tag{3-12}$$

In the solidification of metal alloys, since the Lewis number of a liquid metal is large $(Le \geq 1000)$, thermal equilibrium is readily achieved and nonequilibrium effects are mostly influenced by solutal undercooling. Hence, assuming thermal equilibrium to exist interfacially and through an REV is correct, $\langle T_s\rangle^s = \langle T_l\rangle^l = \langle T\rangle = T$. Then, the final form of mixture energy equation can be written as [20]:

$$\begin{gathered}\rho Cp_m \frac{\partial\langle T\rangle}{\partial t} + \nabla\bullet\left[\rho_l Cp_l \langle T\rangle\langle\vec{v}_l\rangle\right] = \\ \nabla\bullet\left(k_m\nabla\langle T\rangle\right) - \delta H_P \frac{\partial f_l}{\partial t} - \nabla\bullet\left[\rho_l Cp_l T_{ref}\langle\vec{v}_l\rangle\right]\end{gathered} \tag{3-13}$$

in which,

$$\delta H_P = \rho\left(\langle T\rangle - T_{ref}\right)\left(Cp_l - Cp_s\right) + \rho L_{ls} \tag{3-14}$$

3.2.2 Discretization of the Governing Equations

Consider an arbitrary fixed control volume $\Omega_P \subset R^3$, of volume V and boundary, $\partial\Omega_p$ with unit vector $\hat{n}$ normal to the surfaces and pointing outward, filled by continuum (molten metal). The discretization of the governing equations is carried out on an unstructured grid, such as that illustrated in Fig. (3-1), in accordance with the cell-centred finite volume procedure of [21], using a colocated approach.

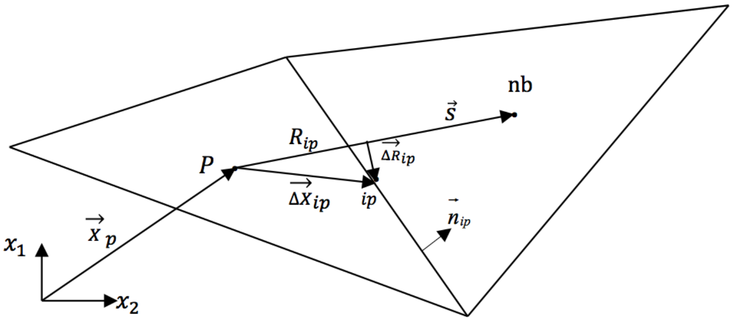

Figure 3-1: A portion of the grid and related nomenclature used in the FVM

The calculation domain is first sub-divided into arbitrary triangular or quadrilateral volumes, and the grid points are placed at the centres, $\vec{x}_p$, of the control volume, while boundary nodes, needed for implementing the boundary conditions, are located at the centre of boundary cell-faces. Then, the governing equations are integrated over an arbitrary control volume with the volume of V_P, which is bounded by the control surface $\partial\Omega_P$, and time. The $\partial\Omega_P$ is assumed to be the union of the discrete control surfaces dA_{ip}, where $ip \in \{1,2,...,n_{ip}\}$, for $n_{ip}=3$ triangles and $n_{ip}=4$ for quadratic grids. All dependent variables, which are unknowns to be solved for, are stored at the centre of each control volume and the discrete equations formed for a control volume depend implicitly upon these values.

The semi-discretized forms of Eq. (3-9), Eq. (3-10) and Eq. (3-13) are given, respectively, for a fully implicit discretization as:

$$\sum_{ip=1}^{n_{ip}} \dot{m}_{ip} = \sum_{ip=1}^{n_{ip}} \rho\left(\hat{\vec{v}}_{ip} \bullet \hat{n}_{ip}\right) A_{ip} = 0 \tag{3-15}$$

$$\begin{gathered}\rho V_P \frac{\partial\left\langle \vec{v}_l \right\rangle_P}{\partial t} + \sum_{ip=1}^{n_{ip}} \frac{\dot{m}}{f_l}\left(\left\langle \vec{v}_l \right\rangle_{ip} - \left\langle \vec{v}_l \right\rangle_P\right) = -\sum_{ip=1}^{n_{ip}} f_l \left\langle P_l \right\rangle_{ip}^{l} \hat{n}_{ip} A_{ip} + \\ \sum_{ip=1}^{n_{ip}} \mu_l \nabla\left\langle \vec{v}_l \right\rangle_{ip} \bullet \hat{n}_{ip} A_{ip} - \frac{f_l \mu_l}{K}\left\langle \vec{v}_l \right\rangle_P V_P - \sum_{ip=1}^{n_{ip}} \mu_l \nabla f_l \Big|_{ip} \bullet \hat{n}_{ip} A_{ip} + \rho_l f_l \left\langle \vec{b} \right\rangle V_P\end{gathered} \tag{3-16}$$

$$\begin{gathered}\rho Cp_m V_P \frac{\partial\left\langle T \right\rangle_P}{\partial t} + \sum_{ip=1}^{n_{ip}} \dot{m}_{ip} Cp_l \left(\left\langle T \right\rangle_{ip} - \left\langle T \right\rangle_P\right) = \\ \sum_{ip=1}^{n_{ip}} k_m \nabla\left\langle T \right\rangle_{ip} . \hat{n}_{ip} A_{ip} - \delta H_P V_P \frac{\partial f_l}{\partial t}\end{gathered} \tag{3-17}$$

The time derivative is discretized using backward differences. Terms with the subscript ip are evaluated at the integration point located at the centroid of face A_{ip}. Note that Eq. (3-16) is in fact obtained by subtracting Eq. (3-15), multiplied by $\left\langle \vec{v}_l \right\rangle_P / f_l$, from the discretized form of Eq. (3-10). Also, Eq. (3-17) is subtracted from Eq. (3-15), multiplied by $Cp_l\left(\left\langle T \right\rangle_P - T_{ref}\right)$. This is done to ensure conservation at all times during solution procedure.

The advecting velocity $(\hat{\vec{v}} \bullet \hat{n})$ appearing in the mass flux expression, Eq. (3-15) for the C.V faces is adopted and modified [20] in accordance with the colocated variable method of [22], which uses a specially constructed momentum equation to avoid pressure-velocity decoupling. The advected value of φ_{ip} is approximated implicitly by a first-order accurate upwind scheme to ensure numerical stability and then a deferred correction procedure [23] is employed to explicitly correct the advected value to higher order. Approximation of the gradient and hessians in the fluid and solid control volumes are based upon the approach of [24]. The detail of the treatment of pressure gradient in the mushy control volumes for structured and unstructured grids is previously reported [20, 25-27] and is not repeated here.

In the current work, the fraction of liquid in the mushy region in the source-based energy equation is estimated by Scheil's equation, which assumes complete mixing in the liquid and no solid diffusion, [28]:

$$f_l = F(T) = \left[\frac{T - T_{mlt}}{T_{liq} - T_{mlt}} \right]^{\frac{1}{k_P - 1}} \tag{3-18}$$

where T_{mlt} is the melting temperature of the alloy, T_{liq} is the liquidus temperature and k_P is the partition coefficient.

The fully discretized form of Eq. (3-15) – (17) can be written in the form of:

$$a_P \varphi_P^m = \sum_{ip}^{n_{ip}} a_{nb} \varphi_{nb}^m + b_P \tag{3-19}$$

The linear algebraic equation was solved using version 3.3 of Portable, Extensible Toolkit for Scientific Computation (PETSc) solver on Shared Hierarchical Academic Research Computing Network (SHARCNET).

3.3 Case Study

Herein, a case study is chosen to emphasize that the information facilitated by the cooling curve during the solidification process is of great importance and can be used for predicting microstructural features such as local SDAS, skin thickness and average yield strength. It is worth mentioning that, in magnesium alloys whose grain structures are in the form of dendritic structures, secondary dendrite arm spacing (SDAS) has a similar influence on the mechanical properties as the grain size and one may use correlations used for grain size prediction to estimate the SDAS.

3.3.1 Wedge Casting Experiment

Wedge casting is a unique experiment that is able to produce various cooling rates from tip to the top and hence, different microstructures can be obtained. As can be seen in Fig. (3-2), a finer grain size microstructure is obtained closer to the tip due to the higher rate of cooling compared to the one further from the tip.

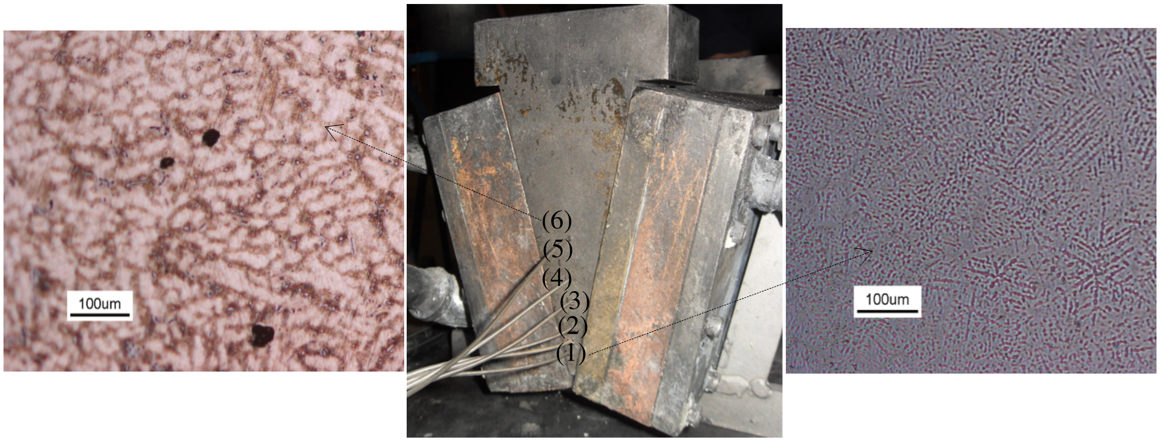

Figure 3-2: Wedge-shaped casting; six embedded thermocouples (middle) and their corresponding microstructures (margins)

Since the detail of the experiment set up was reported previously [16], only a brief explanation of the related process is presented here.

A commercial Al-Mg (AM60B) alloy wrought was used for the purpose of this experiment. The ingots were melted and degassed using hexachlorethane tablets. The melt was purged with argon for more than 20 minutes. The melt was poured at about 1000 K (727 ^{0}C) in a wedge-shaped, water-cooled mold with copper side walls, and steel at the two ends. Six K-type thermocouples were located in various positions as shown in

Fig. (3-2). After the solidification process, samples along the height of the casting were cut and prepared for metallographic analysis [16].

3.3.2 Numerical Set up

A wedge-shaped casting of magnesium alloy, AM60B with physical properties indicated in Table (3-1), [29], is considered.

Table 3-1: Properties of AM60B (units are shown in the nomenclature) [29]

Average Density ρ	2483	Equilibrium Partition Coefficient k_p	0.1875
Liquid Specific Heat Cp_l	1097	Thermal Expansion β	2.3×10^{-5}
Solid Specific Heat Cp_s	992	Melting Temperature T_{mlt}	923
Latent Heat of Fusion L_{ls}	396	Liquidus Temperature T_{liq}	892
Liquid Thermal Conductivity K_l	92.6	Solidus Temperature T_{sol}	796
Solid Thermal Conductivity K_s	130	Liquid Viscosity μ_l	0.0013

Due to the fact that the geometry under consideration is symmetrical, only half of the domain is considered for the numerical study. Fig. (3-3) shows the dimensions of the computational domain and a sample of the grid used. A grid-independence study was done based upon the total percentage of solid in the domain at a certain time during the process. 1497 triangular volumes were used to discretize the half domain, producing results that are grid-independent to within 1.9%. Grids of 856 and 3388 volumes were also run, producing results of lower, and much higher spatial resolution [20]. The 1497-cell case is presented here as it yields results of sufficient accuracy while also demonstrating the robustness of the code for a relatively coarse grid.

A convective boundary condition is applied at the top of the half wedge. An ambient temperature of 298 K and a convection coefficient of 10 W/m^{2}K are used, combined with a slip condition on velocity to approximate the natural convection at this surface.

On the side wall, where mold and metal are in contact, to replicate the water-cooling condition at this edge, a set of constant temperatures between 298 K and 423 K (25 – 150 ^{o}C) was used as the ambient temperature for the Robin boundary condition. For convective heat transfer coefficient, constant values of *h* between 5000 and 400 W/m^2K

were considered to observe the effect of cooling rate on the grain size. It is worth mentioning that this range of *h* values are determined empirically for aluminium alloys in [30] and tabulated in [31]. Also, in separate case studies, the experimental result of [32] and [33], in which the convective coefficients was proposed to be $h(t) = 240 + 2150 \times \exp(-t/14.5)$, is considered to partially account for the transient boundary condition on the side wall.

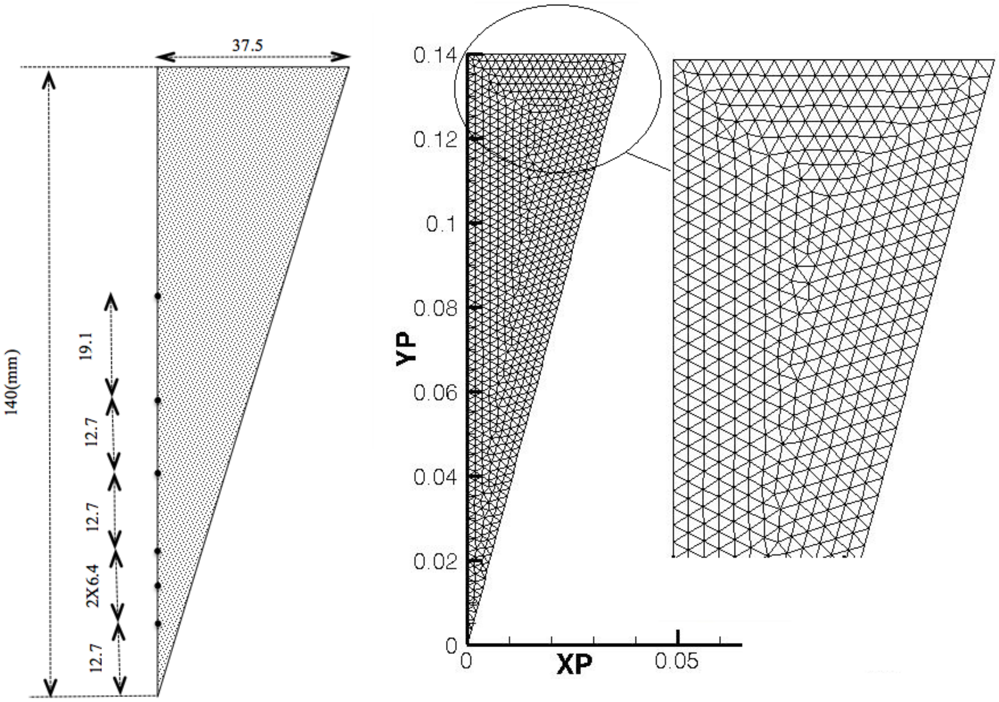

Figure 3-3: Half of the wedge-shaped casting with six thermocouples embedded at the centerline (left), Unstructured triangular mesh (right)

It will be shown later how this variation in the boundary conditions and, therefore, heat extraction at the boundary would result in different mechanical properties. In addition, a no-slip, zero-penetration condition on velocity was considered as the boundary conditions for mass and momentum equations. A symmetry condition is imposed on the left (vertical) edge of the domain.

For the permeability coefficient in the Darcy term of Eq. (3-16), several values and methods are previously reported [34,35] in the literature, either based on the fact that these values caused a better stability in the solution, or based upon the physics that were involved in the problem. The correct value for a constant permeability for the purpose of this study, or any other similar study, is a value close to the average SDAS or grain size for the particular alloy of interest. Herein, $100\mu m$ is used as the permeability coefficient.

A time step size of five milliseconds was required to properly capture the temporal resolution of the solidification process [20]. A further reduction in time-step size produced results that were not significantly different. Convergence of the linearization loop occurred when the maximum normalized residual was reduced to below the value 10^{-6}. The computation was performed on SHARCNET using a single Intel Xeon 2.83 GHz CPU with 16 GB memory/node. The averaged elapsed CPU times for obtaining a completely solidified domain were between about 4.4 and 12.0 hours for the cases with highest and lowest cooling rates, respectively, and the code required 2.9 GB virtual memory.

3.3.3 Results and Discussions

As previously mentioned, several different boundary conditions were considered for the side wall of the wedge shaped casting to replicate a condition similar to water-cooled copper mold, and also to observe the effect of cooling rate on the grain size and, therefore, the mechanical properties of the casting.

Table 3-2: A summary of imposed boundary conditions on the side wall

Case#	$q/A = h(t)\left(T - T_\infty\right)$ $h(t) = 240 + 2150 \times \exp(-t/14.5)$	Case#	$q/A = h\left(T - \left(75^0 C\right)\right)$
AM1	$T_\infty = 25\,^0C$	AM4	h=5000 W/m^2K
AM2	$T_\infty = 75\,^0C$	AM5	h=1000 W/m^2K
AM3	$T_\infty = 150\,^0C$	AM6	h=400 W/m^2K

To avoid confusion between cases, Table (3-2) is given to present a summary of the various cases to indicate the naming convention used in the remainder of this article.

Fig. (3-4) Shows contours of solid fraction (right half of the domain) and the temperature field (left half of the domain) at three different times (10, 20, and 30(s)) during the solidification process for case AM1.

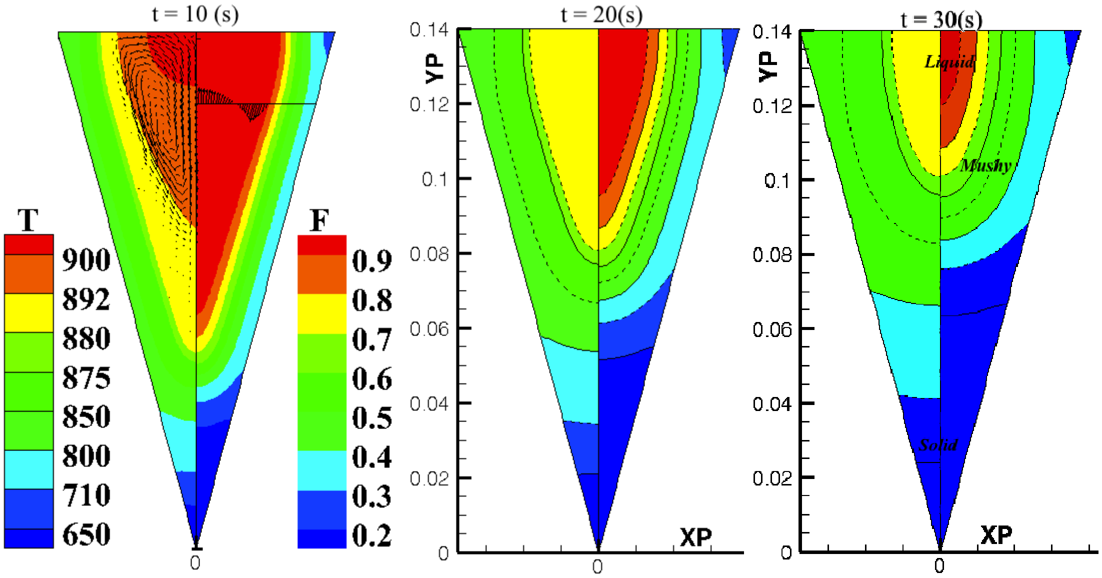

Figure 3-4: Contours of solid fraction (right half of the domain) and temperature (left half of the domain) at three different times during the solidification process. Also, the velocity vectors are shown to illustrate the direction of convection in the mushy and liquid regions.

As expected, the plots show clearly the rapid cooling at the lower tip followed by the more gradual cooling that occurs in the wide part of the casting. The plots also show the connection between the temperature and the motion of the solidification front. The region close to the tip solidifies at the early stage of simulation due to the higher cooling rate while the rest of the domain requires a longer time to fully solidify. Solid, mushy and liquid regions are indicated in the figure. At t = 10(s) the velocity field vectors are shown to illustrate the direction of flow in the mushy and liquid regions and confirms the occurrence of convection during the process. The velocity vector profile at height y=120 mm is also superimposed in the figure to show the structure of the velocity field. As the molten metal solidifies in the tip region, the thermal convection creates a roll shaped velocity field that moves towards the top of the domain and disappears when the molten metal is fully solidified.Fig. (3-5) shows contours of grain size for the six different cases, AM1-AM6, right half of the plots show contours of the grain size calculated based upon the solidification time (GSTS), Eq. (3-4), and the left half shows contours of the grain size calculated based upon the cooling rate (GSR), Eq. (3-5).

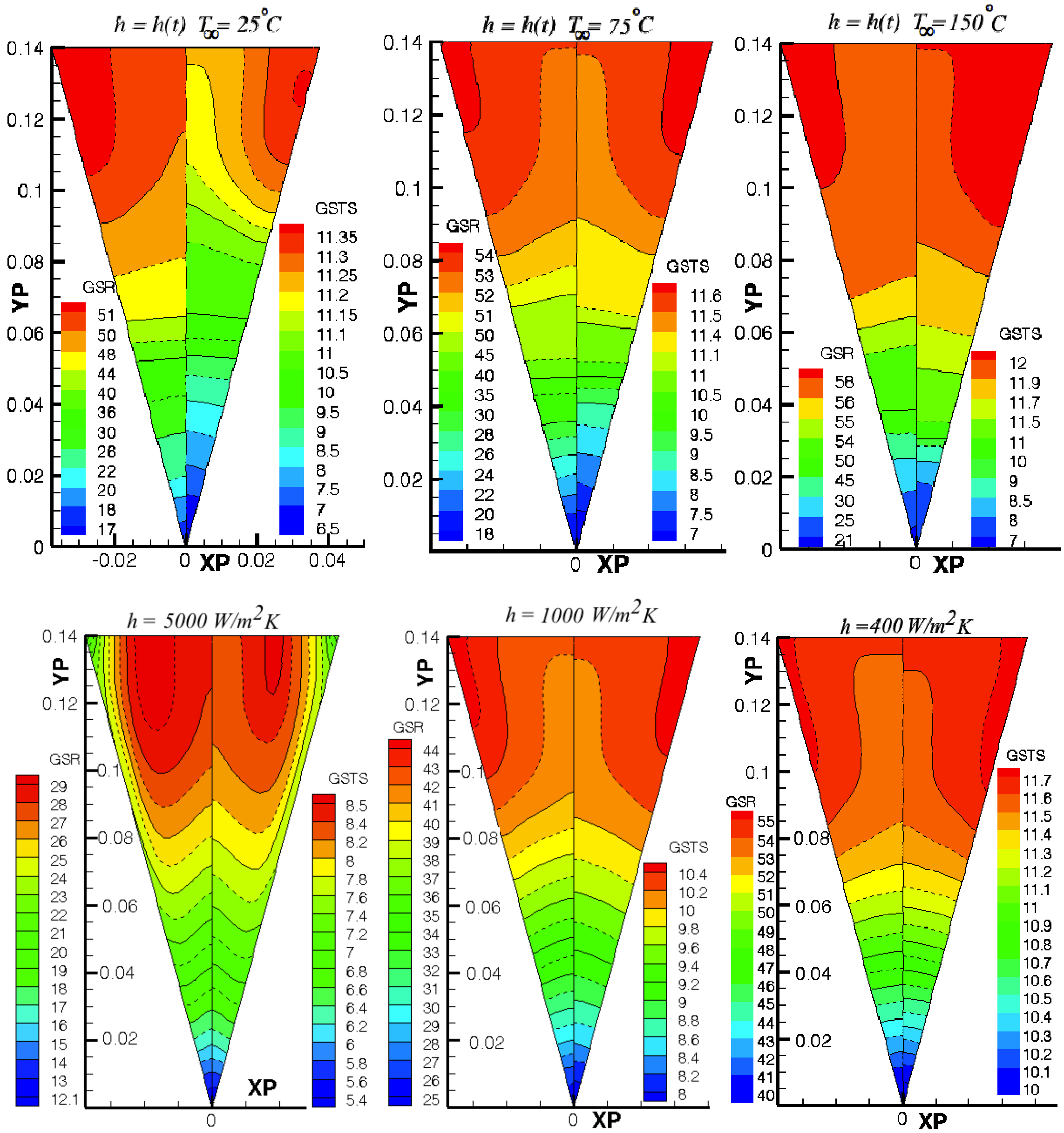

Figure 3-5: Contours of grain size from higher (left) to lower cooling rate (right) when h is constant. One half of the symmetry is the contours of the grain size calculated based upon the solidification time (GSTS) and the other half is contours of the grain size calculated based upon the cooling rate (GSR)

In each individual case, due to higher cooling rates and shorter solidification times close to the tip of the wedge, smaller grain size is obtained in this region. In all six cases, the grain size values calculated using Eq. (3-5) are above the threshold of 10 μm defined by

[8], therefore, the result suggests that for the entire domain at any cross section the yield strength can be calculated using the Hall-Petch relationship, Eq. (3-1).

The contours of grain size using Eq. (3-4), on the other hand, shows the possibility of the existence of both skin and core regions in all cases except for the case AM4, in which, due to the presence of high cooling rate, the grain size values for the entire domain are below the threshold of 10 μm. This advocates the use of modified Hall-Petch correlation, Eq. (3-2), for yield strength measurement for some cross sections within the domain.

Fig. (3-6) and Fig. (3-7) show plots of grain size variation at cross sections coinciding with the height of thermocouples #2, 4 and 6 for all six cases. While the variation of grain size across these cross-sections does not vary significantly the effect of various cooling rates along these cross sections is noticeable for case AM4. For the sake of discussion, consider Case AM4 in Fig. (3-7) (top left plot) and the cross section coinciding with thermocouple #6. The plot shows that the grain size is smaller closer to the wall and the centreline but larger in between. To explain this, we consider the cooling characteristics in different parts of the casting.

If a fluid parcel adjacent to the side wall is considered, it is evident that the fluid is surrounded by a cold wall on one side and hot liquid on the other. Due to the existence of the cold wall and the large temperature difference, the cooling rate during solidification is and, therefore, the grain size is fairly small in this region. If a parcel removed from the wall is considered, during its solidification it is exposed to already solidified, but hot, metal on one side and molten metal on the other. Since the temperature of the solidified metal is hotter than the mold wall, the net effect compared to a parcel that solidified at the mold wall is slower cooling rate and a larger grain size. Fluid parcels that cool near the symmetry plane of the casting experience cooling from already solidified metal and have little exposure to molten metal (only from above). As such, compared to fluid parcels that solidify in the region between the mold wall and the symmetry plane, the cooling rate is higher and the grain size is finer.

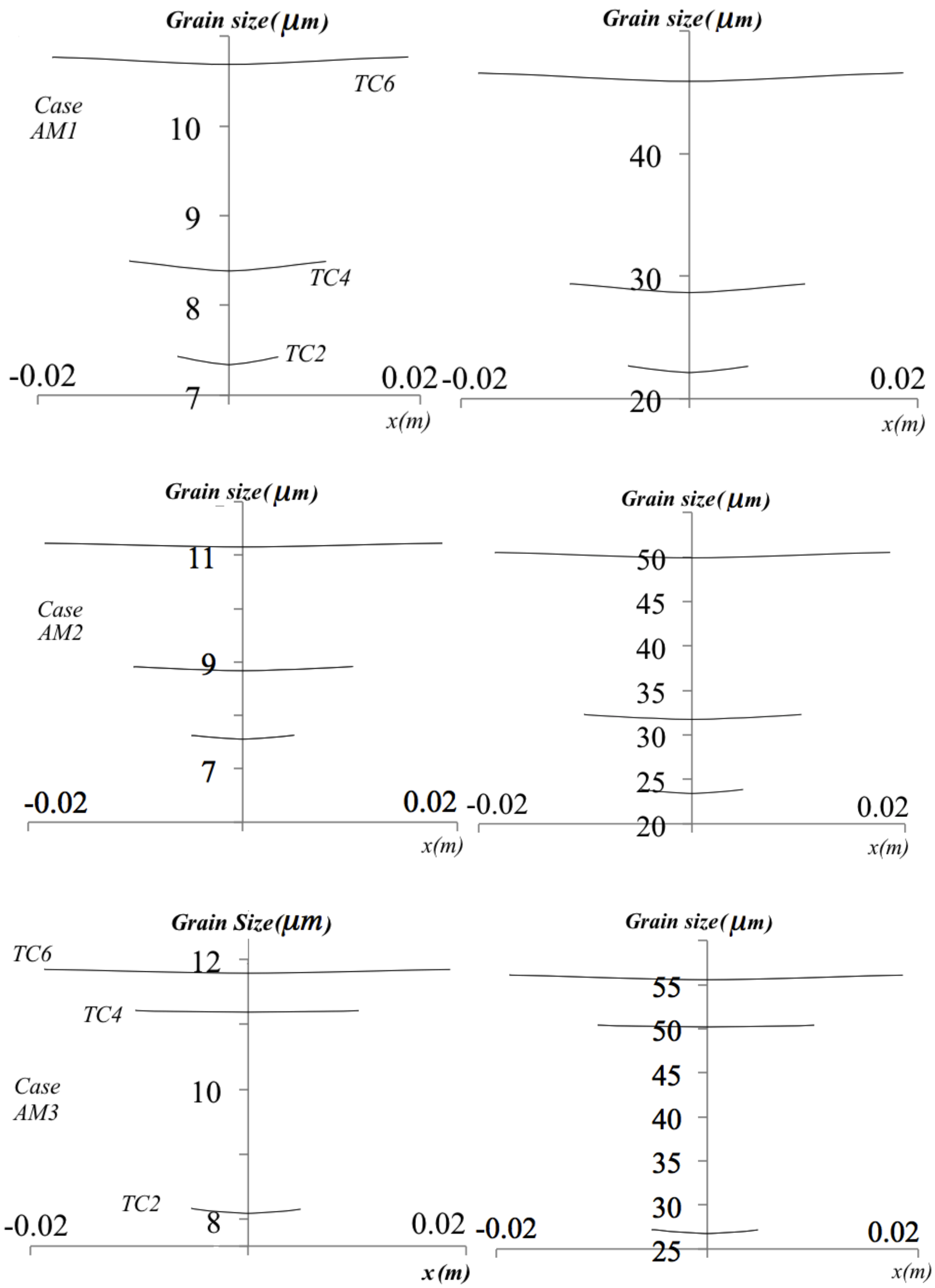

Figure 3-6: Plots of grain size variation at cross sections coincided with the height of thermocouples #2, 4 and 6 using solidification time (left column) and cooling rate (right column) for the case with transient h and T_∞=25,75 and 150 ^{0}C (top to bottom)

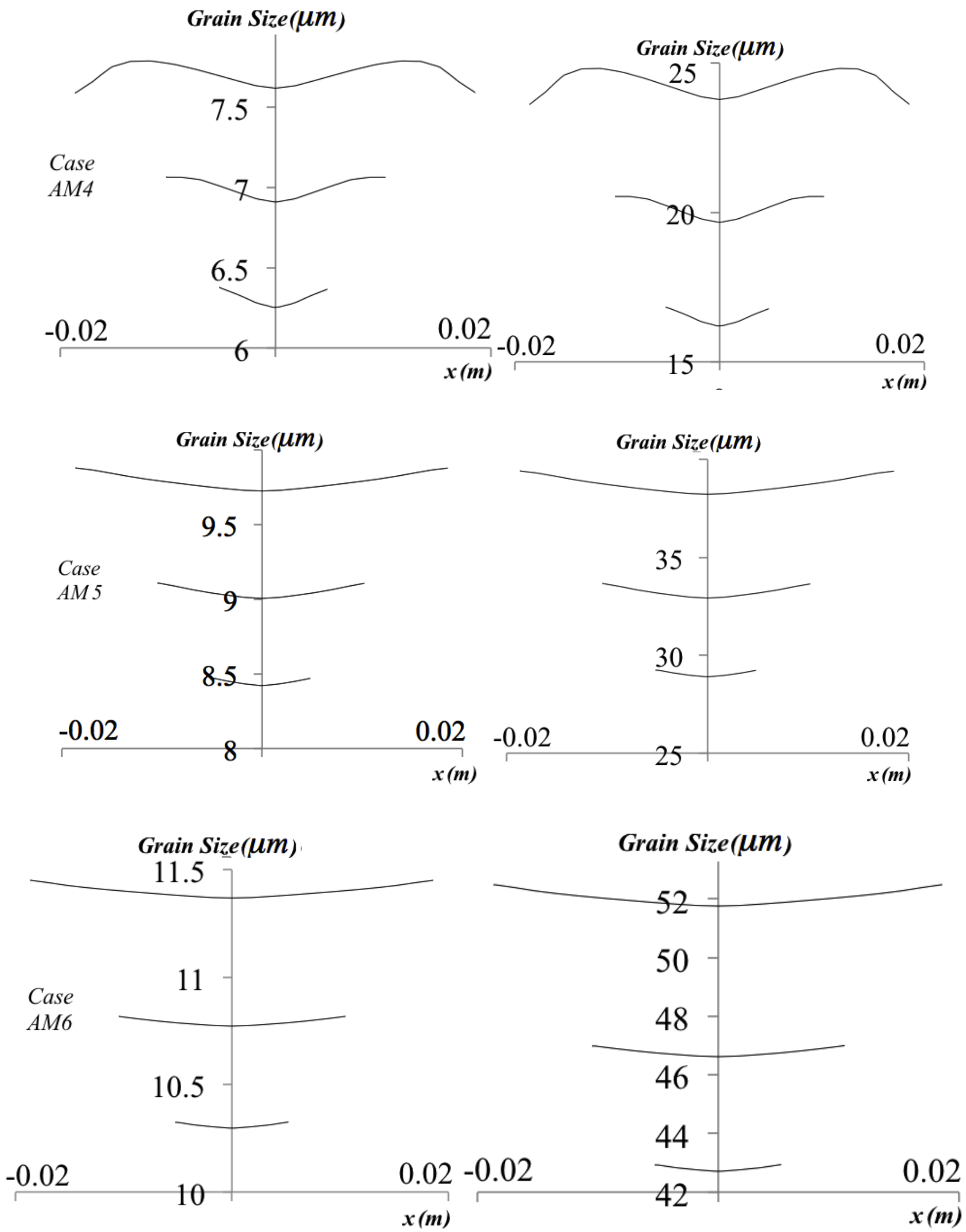

Figure 3-7: Plots of grain size variation at cross sections coincided with the height of thermocouples #2, 4 and 6 using solidification time (left column) and cooling rate (right column) for the case with transient h=5000, 1000 and 400 W/m^{2}K (top to bottom)

The resulting cooling curves of thermocouple#4 for all the six cases are shown in Fig. (3-8).

Cases AM1-AM3 (dashed lines) show the closest trend to the experimental cooling curve. Therefore, only the results of grain size calculation based upon these three cases are compared to the previously reported experimental data [16] and are shown in Fig. (3-9).

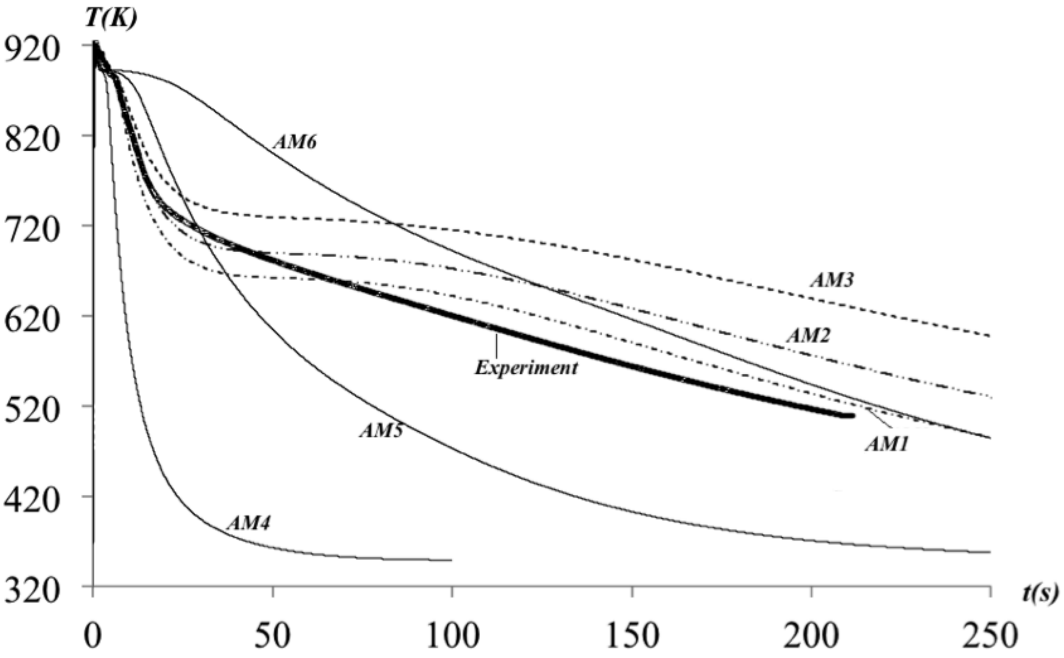

Figure 3-8: Cooling curves for different cases at thermocouple #4

One should notice that both Eq. (3-4) and Eq. (3-5) are using the data related to the solidification time. However, since based upon the numerical study presented here, it was found that the numerically derived correlation, Eq. (3-5), leads to overestimated grain size with unreasonable error, only grain size measurements calculated using experimentally derived correlation, Eq. (3-4), are compared to the experimental data. The result of this comparison shows an increasing trend in the grain size from the tip of the wedge to the top of the wedge in all three cases due to the variation of cooling rate. Also, a good agreement between the result of AM1 and AM2 and the experimental measurement of the grain size at various thermocouples can be observed.

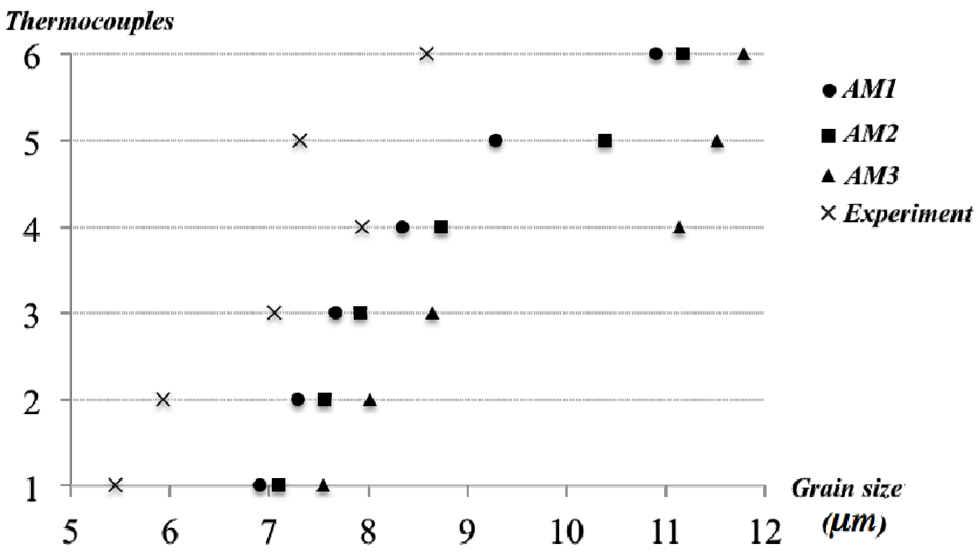

Figure 3-9: Comparison of experimental grain size measurement and cases AM1-AM3

Fig. (3-10) shows contours of the local yield strength using the Hall-Petch equation for cases AM1-AM3.

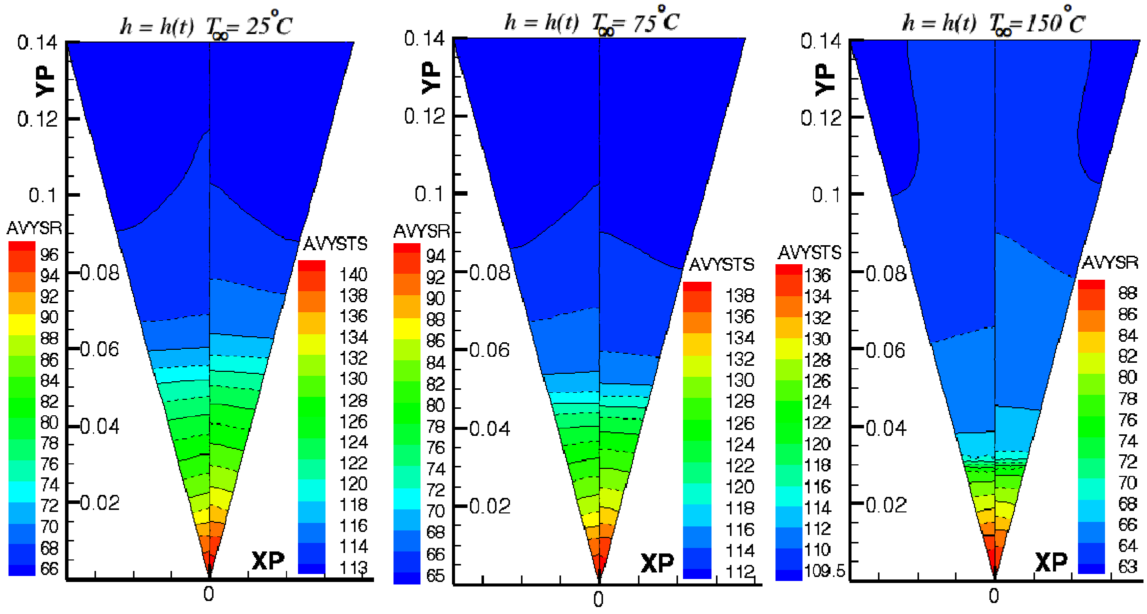

Figure 3-10: Contours of local yield strength using Hall-Petch correlation. On the right and left half of symmetry the grain size used in the Hall-Petch correlation is calculated using the cooling rate and the solidification time, respectively

The yield strengths on the left and right side of the symmetry line are calculated based upon the grain size that is measured by Eq. (3-5) and Eq. (3-4), respectively.

As the grain size increases from tip to the top of the wedge the yield strength decreases, as expected. As discussed previously, for a more accurate measurement of the yield strength within the domain a measurement of the thickness of the skin and core region is required.

Fig. (3-11) shows plots of grain size variation at the centerline of the wedge using Eq. (3-4) and Eq. (3-5) for cases with transient h and T_∞=25,75 and 150 ^{0}C, (AM1-AM3). Fig. (3-12) also shows the same type of plots but for cases with constant h, (AM4-AM6). In all cases, if the grain size is under the threshold of $10\,\mu m$, defined in [8], then, the region is identified as skin and if the grain size value is above this threshold, the region is called core. This identification could provide enough information about the type of correlation , Hall-Petch versus modified Hall-Petch, that can be used to obtain the yield strength of a sample.

For case AM2, for example, the skin region has a thickness of about 48 mm and has a fraction of about δ_t = 0.34 of the total length of the cross section. One can use the combination of average grain size in the skin, $129.92\,MPa$, and the core regions, 112.50 MPa, and Eq. (3-2) to obtain the average yield strength along the centre line of the wedge:

$$\sigma = 0.34 \times 129.92 + 0.66 \times 112.5 = 118.42 MPa \qquad (3\text{-}20)$$

It is evident that if the specimen cut from the centreline goes under the tensile test the core region yields first.

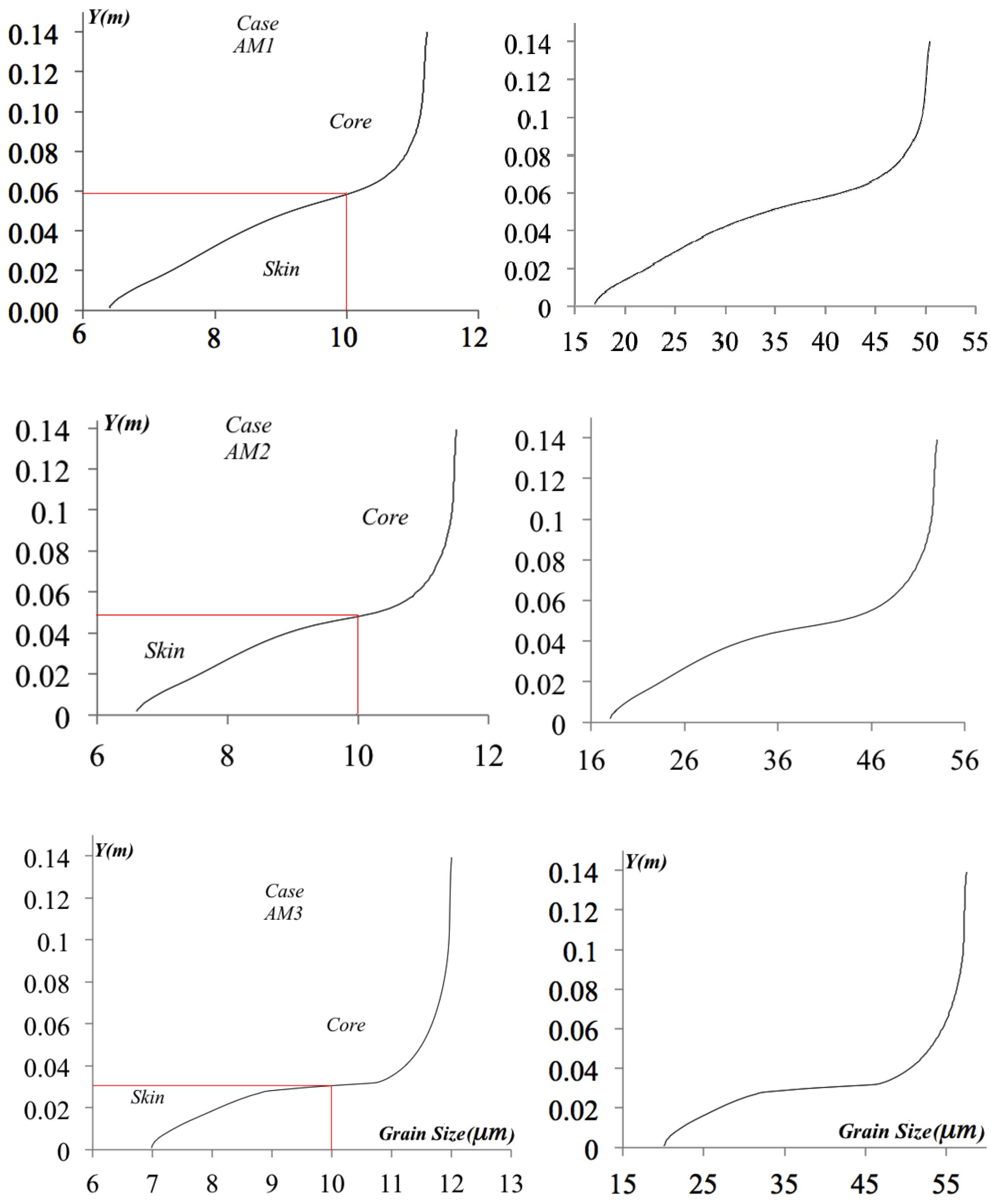

Figure 3-11: Plots of grain size variation at the centerline of the wedge using solidification time (left column) and cooling rate (right column) for the case with transient h and T_∞=25,75 and 150 ^{0}C (top to the bottom)

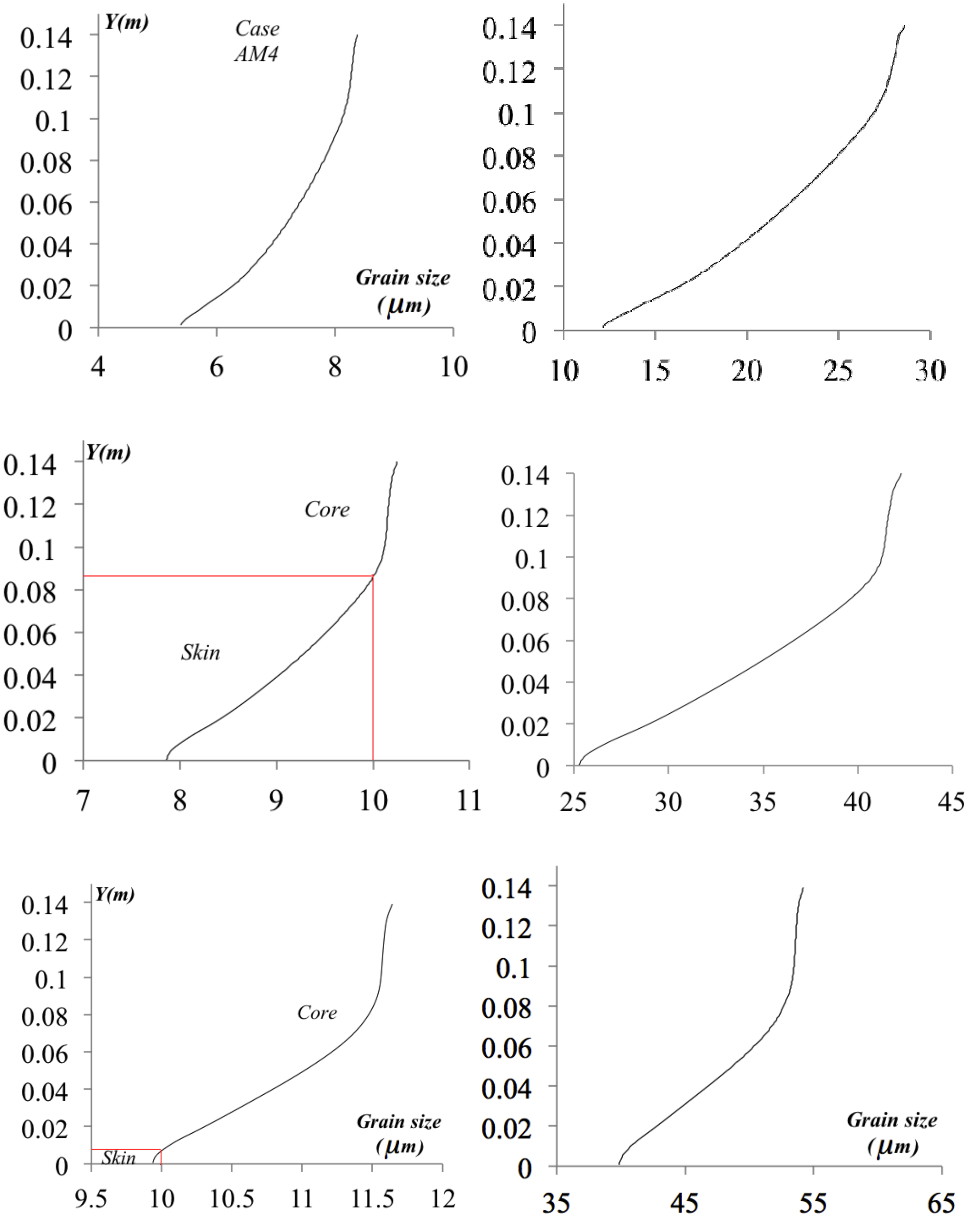

Figure 3-12: Plots of grain size variation at the centerline of the wedge using solidification time (left column) and cooling rate (right column) for the case with h=5000,1000 and 400 W/m^{2}K (top to bottom)

3.4 Summary

In the present work, a general single region volume averaged finite volume formulation has been presented and tested for the solidification of a commercially used magnesium alloy to predict local cooling curves, grain size and yield strength within a wedge shaped casting. While there is good agreement between the result of numerical simulation and experimental data, the result of this comparison emphasizes the importance of the influence of cooling rate on the mechanical properties of castings. It is shown that even for a slightly different boundary condition, which resulted in variation of the cooling rates, various grain size and, hence, various yield strength was obtained.

3.5 References

[1] D.J. Lloyd and S.A. Court, Influence of grain size on tensile properties of Al-Mg alloys, Material Science and Technology, vol.19, pp.1349-1354, 2003

[2] M.S. Dargusch, K. Pettersen, K. Nogita, M.D. Nave, and G.L. Dunlop: The effect of aluminum content on the mechanical properties and microstructure of die cast binary magnesium-aluminum alloys. Materials Transactions. vol.47, PP. 977-982, 2006

[3] P. Andersson, C.H. Caceres, and J. Koike: Hall-Petch Parameters for Tension and Compression in Cast Mg. Materials Science Forum. vol.419, PP.123-128, 2003

[4] E.O. Hall, The Deformation and aging of mild steel III, Proceeding of Physical Society, vol.64B, pp.747-753, 1951

[5] N.J. Petch, The cleavage strength of polycrystals, Journal of Iron and Steel Institute, vol.174, p.25, 1953

[6] T.M. Yue, H.U. Ha, and N.J. Musson: Grain size effects on the mechanical properties of some squeeze cast light alloys. Journal of Materials Science, vol.30, pp.2277-2283, 1995

[7] F.E. Hauser, P.R. Landon, and J.E. Dorn: Fracture of Magnesium Alloys at Low Temperature. Transactions of the American Institute of Mining, Metallurgical and Petroleum Engineers, vol.206, pp.589-593, 1956

[8] J.P. Weiler, The development of comprehensive materials models of the structure-properties relationships for Die-Cast Magnesium alloy AM60B, Ph.D. thesis, The University of Western Ontario, 2009

[9] J.P. Weiler, J.T. Wood, R.J. Klassen, R. Berkmortel and G. Wang, Variability of skin thickness in an AM60B magnesium alloy die-casting, Materials Science and Engineering: A, vol. 419(1) pp. 297-305, 2006

[10] G. Mima, and Y. Tanaka: Grain Size dependence of Yield Stress and Flow Stress in the Age-Hardened Magnesium-Zinc Alloy. Journal of the Japan Institute of Metals, vol.35, pp.317-322, 1971

[11] J.P. Weiler, Structure-property relationships for die-cast Mg alloy AM60B, The University of Western Ontario, M.E.Sc. Thesis, London Ontario, 2005

[12] W.P. Sequeira, G.L. Dunlop, and M.T. Murray: Effect of Section Thickness and Microstructure on the Mechanical Properties of High Pressure Die Cast Magnesium AlloyAZ91D. Proceedings of the 3rd International Magnesium Conference, ed. G.W. Lorimer (Manchester, UK: The Institute of Metals, 1996) pp.63-73, 1996

[13] D.Yin, Microstructural Characterization of a Magnesium Die-Casting, The University of Western Ontario M.E.Sc. Thesis, 2004

[14] A.L. Bowles, J.R. Griffiths, and C.J. Davidson: Ductility and the skin effect in high-pressure die-cast Mg-Al alloys. Magnesium Technology 2001. ed. J. Hryn, pp.161-168, 1971

[15] Y. Unigovski, E. Gutman, A. Eliezer, L. Riber, and Z. Koren: Correlation of mechanical properties of die cast magnesium alloys with processing conditions. Magnesium 2000: Proceedings of the 2nd Israeli International Conference on Magnesium Science and Technology. Eds. E. Aghion and D. Eliezer, pp.105-111, 2000

[16] I. Basu, Effect of process variables on the microstructural features for as-cast magnesium alloys, ME.Sc Thesis, Western University, London, Ontario, 2011

[17] N.H. Pryds and X. Huang, the effect of cooling rate on the microstructure formed during solidification of ferritic steel, Metallurgical and Materials Transactions A, vol. 31A, pp. 3155-3166, 2000

[18] Reed-Hill, Robert E., and Reza Abbaschian. Physical metallurgy principles, vol. 267. No. 725. Princeton: Van Nostrand, 1964

[19] A. Banarje, Process structure relationship of magnesium alloys, M.E.Sc thesis, The University of Western Ontario, 2013

[20] M. Farrokhnejad, A.G. Straatman, J.T. Wood, A volume averaged finite-volume model for solidification of magnesium alloys on a general unstructured collocated grid, Accepted in the Journal of Numerical Heat Transfer, Part A: Application, 2013

[21] S.V. Patankar, Numerical Heat Transfer and Fluid Flow, Hemisphere, New York, 1980

[22] C. M. Rhie and W.L. Chow, Numerical study of the turbulent flow past an airfoil with trailing edge separation, American Institute of Aeronautics and Astronautics Journal, vol.21, pp.1525-1532, 1983

[23] PK. Kholsa and SG. Rubin, A diagonally dominant second order accurate implicit scheme, Computers and Fluids, vol.2, pp.207-209, 1974

[24] L. Betchen, A. Straatman, An accurate gradient and Hessian reconstruction method for cell-centred FV discretizations on general unstructured grids, International Journal for Numerical Methods In Fluids, vol.62, pp.945-962, 2009

[25] M. Farrokhnejad, A.G. Straatman, J. Wood, A Volume-of-Fluid Based Numerical Simulation of Solidification in Binary Alloys on Fixed Non-uniform Co-located grids, ASME International Manufacturing Science and Engineering, USA, West Lafayette, IN, pp. 427-436, 2009

[26] M. Farrokhnejad, A.G. Straatman, Advances on a VOF Based Numerical Simulation of Mg Die-Casting Process on a General Unstructured Grid. 9th International Conference on Mg Alloys & Their Applications, Vancouver, Canada, 2012

[27] M.Farrokhnejad, A.G. Straatman, J.T.Wood, A Finite-Volume Model for Numerical Solidification of Mg Alloys, Materials Science Forum vol. 765, pp 281-285, 2013

[28] V. R. Voller and C. R. Swaminathan, Earl Source-Based Method for solidification phase change, Numerical Heat Transfer, Part B: Fundamentals, vol.19, pp.175-189, 1991

[29] C.J. Vreeman and F.P. Incropera, The effect of free-floating dendrites and convection on macrosegregation in direct chill cast aluminum alloys: Part II: Predictions for Al-Cu and Al-Mg alloys, International Journal of Heat and Mass Transfer, vol.43, pp.687-704, 2000

[30]DR Poirier, EJ Poirier, Heat transfer fundamentals for metal casting, The Minerals, Metals & Materials Society, 1992

[31] D.L. Winterscheidt, G.X. Huang, Fundamentals of Casting Process Modeling in Modeling for casting and solidification processing, Edited by Kuang Oscar Yu, Marcel Dekker Inc. NewYork, Basel, 2002

[32] M. Trovant and S. Argyropoulos, Finding boundary conditions: A coupling Strategy for the modelling of metal casting processes: Part I. Experimental study and correlation development, Metallurgical and Materials transaction B, vol. 31B, pp.75-86, 2000

[33] Y. He, A. Javaid, E. Essadiqi and M. Shehata, Numerical simulation and experimental study of the solidification of a wedge-shaped AZ31 Mg alloy casting, Canadian Metallurgical Quarterly, vol.48, pp. 145-156, 2009

[34] V.R. Voller and C. Prakash, A fixed grid numerical modeling methodology for convection-diffusion mushy region phase-change problems, International Journal of Heat and Mass Transfer, vol.30, (8), pp.1709-1719, 1987

[35] D. R. Poirier, Permeability for flow of interdendritic liquid in columnar-dendritic alloys, Metallurgical and Materials Transactions B, vol.18b, pp.245-256, 1987

Chapter 4

4 Summary

4.1 Contributions

In the present work, a general single region volume averaged finite volume formulation has been presented and tested for the solidification of a commercially available magnesium alloy to predict local cooling curves, grain size and yield strength within a wedge shaped casting.

An additional sink term resulting from the assumption of non-zero gradient of solid fraction is the main difference in the derived momentum equation compared to previously published momentum equations for studying the solidification process in binary alloys. Although the assumption of the non-zero gradient of solid fraction is necessary to be made in the derivation of conservative equations, the extra term will only have a noticeable effect on the velocity field for cases where convection is strong.

The discretization of the equations was carried out for a general unstructured grid using the most modern existing approaches. However, to obtain a correct velocity field in the mushy zone and in control volumes adjacent to mixed control volumes, a special treatment of the pressure gradient is proposed. The special momentum equation for coupling the mass-momentum equation was modified to account for the effect of non-zero solid fraction gradient.

In casting and discretization of the energy equation, a unique derivation approach was chosen that results in a stable temperature-based energy equation with all the essential terms that must be considered in the alloy solidification. For the evolution of solid fraction, contrary to previously published work, no under-over relaxation was considered, yet a smooth, rapid convergence of the temperature field was achieved without oscillation.

The proposed formulation was tested for a wedge-shaped AM60B alloy to first predict the cooling rates at six embedded thermocouples, with results compared against previously reported experimental results. While the results of this study show a good agreement with the experimental data, it was concluded that a better understanding of the boundary condition that existed during the experiment would result in a more agreeable result.

Then, the structure-properties experimental correlations were considered in the in-house code combined with a different set of boundary conditions to predict the variation of local grain size and yield strength within the wedge casting. Based upon previously reported experimental work, the threshold grain size for identification of the skin and core regions was considered to modify the local yield strength. While there is good agreement between the result of numerical simulation and experimental data, the result of this comparison emphasizes the importance of the influence of cooling rate on the mechanical properties of castings. It is shown that even for a slightly different boundary condition, which resulted in variation of the cooling rates, various grain sizes and, hence, various yield strengths were obtained.

It is concluded that the formulation and the numerical treatment presented herein has the ability to relate solidification history to distribution of mechanical properties.

4.2 Recommendation for Future Work

There is a need for further studies to be made. In particular:

- The work presented lacks the heat transfer coefficient for the transient boundary condition at the side wall. Experimental work for this purpose would certainly provide assistance to impose a correct boundary condition, and therefore, a more accurate cooling rate for the process.

- The effects of shrinkage should be considered. As shown previously, shrinkage is an inherent phenomenon of the solidification process that could lead to casting defects. Mass equation should be modified to account for density variations and therefore, mass deficit during the casting process. In addition, being able to predict shrinkage phenomenon would result in predicting the instant when the casting separates from the mold, therefore a correct boundary condition could be achievable.

- Species equation should be added to the formulation to predict solutal-segregation during the process of solidification. Having the composition and temperature at a certain pressure during the process would result in a better understanding of the solidification process.
- Finally, predicting the size and location of defects is crucial to predict the mechanical properties of castings and should be considered in future research works.

Appendices

Appendix A: Field Variable at the Integration Point

The advected value of φ_{ip} is approximated implicitly by a first-order accurate upwind scheme to ensure numerical stability and then a deferred correction procedure is employed to explicitly correct the advected value to higher order:

$$\left(\varphi_{ip}^{HO}\right)^{m} = \left(\varphi_{ip}^{UDS}\right)^{m} + \left(\varphi_{ip}^{HO} - \varphi_{ip}^{UDS}\right)^{m-1} \tag{A-1}$$

where m is the current iteration of linearization loop. Any higher order (HO) schemes including central differencing scheme (CDS), second order upwinding (SOU), etc. can be used.

In this work the CDS was chosen as the second order scheme. Considering α being a weighting factor that dictates the direction of flow and Pe represent Péclet number,

$$\alpha = \frac{\dot{m}}{\left|\dot{m}\right|}\left(\frac{Pe^{2}}{5+Pe^{2}}\right) \tag{A-2}$$

$$\left(\varphi_{ip}^{HO}\right)^{m} = \left(\frac{(1+\alpha)}{2}\varphi_{P} + \frac{(1-\alpha)}{2}\varphi_{nb}\right)^{m} + \beta\left[\varphi_{ip}^{HO} - \varphi_{ip}^{UDS}\right]^{m-1} \tag{A-3}$$

where φ_{ip}^{HO} is calculated in a manner that is explained in the next section and $0 < \beta < 1$ is the blending factor.

Appendix B: Gradient at the Cell Centre and Integration Point

It is necessary to obtain a second-order accurate approximation for the gradient at the integration points to maintain the order of accuracy. Using Gauss' theorem:

$$\int_{V_P} \nabla\varphi \, dV = \int_{A_{ip}} \varphi_{ip} . \hat{n} \, dA_{ip} \tag{B-1}$$

Expanding the L.H.S about x_p:

$$\begin{aligned}&\int_{V_P}\nabla\varphi\, dV = \int_{V_P}\left[\nabla\varphi\big|_P + \nabla\nabla\varphi\big|_P .(x-x_P) + O(\delta^2)\right] = \\ &\left(\nabla\varphi\big|_P + O(\delta^2)\right)V_P\end{aligned} \tag{B-2}$$

Or:

$$\nabla\varphi\big|_P = \frac{1}{V_P}\left[\int_{A_{iP}}\varphi_{ip}\hat{n}\,dA_{ip} + O(\delta^2)\right] = \frac{1}{V_P}\sum_{ip}\int_{A_{iP}}\varphi_{ip}\hat{n}\,dA_{ip} + O(\delta^2) \tag{B-3}$$

The R.H.S of Eq. (B.3) includes face-centred variable, so we expand it about x_{ip}:

$$\varphi_{ip}\hat{n}dA_{ip} = \left[\varphi_{ip} + \nabla\varphi\big|_{ip}(x-x_{ip}) + \frac{1}{2}\nabla\nabla\varphi\big|_{ip}(x-x_{ip})(x-x_{ip}) + O(\delta^3)\right]\hat{n}dA_{ip} \tag{B-4}$$

Substituting back into Eq. (B-3) then:

$$\begin{aligned}&\nabla\varphi\big|_P + O(\delta^2) = \\ &\frac{1}{V_P}\sum_{ip}\left[\varphi_{ip} + O(\delta^3)\right]\hat{n}A_{ip} + \frac{1}{2V_P}\sum_{ip}\left[\nabla\nabla\varphi\big|_{ip} : \int_{A_{ip}}(x-x_{ip})(x-x_{ip})\right]\hat{n}dA_{ip}\end{aligned} \tag{B-5}$$

One must notice that because $\dfrac{A_{ip}}{V_P} = O(\delta^{-1})$ the summation on the R.H.S must be of the order of δ to ensure second order accuracy. For the hessian using the Taylor's series expansion

$$\nabla\nabla\varphi\big|_{ip} = \nabla\nabla\varphi\big|_P + O(\delta) \tag{B-6}$$

Adopting the strategy of explicitly retaining the summation on the R.H.S of Eq. (B-5) then:

$$\begin{aligned}
&\sum\nolimits_{ip}\left[\nabla\nabla\varphi\Big|_{ip} : \int_{A_{ip}} (x-x_{ip})(x-x_{ip})\right]\hat{n}dA_{ip} = \\
&\left[\nabla\nabla\varphi\Big|_{P} + O(\delta)\right] : \sum\nolimits_{ip}\int_{A_{ip}} (x-x_{ip})(x-x_{ip})\hat{n}dA_{ip} = \\
&\nabla\nabla\varphi\Big|_{P} : \left(\int_{A_{ip}} xxn\,dA_{ip} - \sum\nolimits_{ip} x_{ip}x_{ip}ndA_{ip}\right) + O(\delta^5) = \\
&\nabla\nabla\varphi\Big|_{P} : \underbrace{\int_{A_{ip}} xxn\,dA_{ip}}_{\int_{V_P}\nabla x^2\,dV_P = 2V_P x_P} - \nabla\nabla\varphi\Big|_{P} : \sum\nolimits_{ip} x_{ip}x_{ip}ndA_{ip} + O(\delta^5) = \\
&2V_P.\nabla\nabla\varphi\Big|_{P}.x_P - \nabla\nabla\varphi\Big|_{P} : \sum\nolimits_{ip} x_{ip}x_{ip}ndA_{ip} + O(\delta^5)
\end{aligned} \tag{B-7}$$

Substituting Eq. (B-7) into Eq. (B-5) then:

$$\begin{aligned}
&\nabla\varphi\Big|_{P} + O(\delta^2) = \\
&\frac{1}{V_P}\sum\nolimits_{ip}\varphi_{ip}\hat{n}A_{ip} + \nabla\nabla\varphi\Big|_{P}.x_P - \frac{1}{2V_P}\nabla\nabla\varphi\Big|_{P} : \sum\nolimits_{ip} x_{ip}x_{ip}ndA_{ip} + O(\delta^2) = \\
&\frac{1}{V_P}\sum\nolimits_{ip}\left[\varphi_{ip} - \frac{1}{2}\nabla\nabla\varphi\Big|_{P} : x_{ip}x_{ip}\right]ndA_{ip} + \nabla\nabla\varphi\Big|_{P}.x_P + O(\delta^2)
\end{aligned} \tag{B-8}$$

Now, to be able to approximate the second order gradient at the cell centre using Eq. (B-8), the φ_{ip} must be evaluated up to $O(\delta^3)$ based on knowledge of the cell-centred quantities.

For this, the quantity of interest and its derivative is first interpolated to some point lying a fraction R_{ip}, see Fig. (2-3), of the distance along the vector that connects node P to its neighbor, $\vec{s}$, then extrapolated from this point to the integration point:

$$\begin{cases}
\varphi_P = \varphi_{R_{ip}} + \nabla\varphi\Big|_{R_{ip}} \bullet R_{ip}\vec{s} + \frac{1}{2}\nabla\nabla\varphi\Big|_{R_{ip}} R_{ip}\vec{s}.R_{ip}\vec{s} + O(\delta^3) \\
\varphi_{nb} = \varphi_{R_{ip}} - \nabla\varphi\Big|_{R_{ip}} \bullet (1-R_{ip})\vec{s} + \frac{1}{2}\nabla\nabla\varphi\Big|_{R_{ip}} (1-R_{ip})\vec{s}.(1-R_{ip})\vec{s} + O(\delta^3)
\end{cases} \tag{B-9}$$

Adding these two results in:

$$(1-R_{ip})\varphi_P + R_{ip}\varphi_{nb} = \\ \varphi_{R_{ip}} + \frac{1}{2}\nabla\nabla\varphi\Big|_{R_{ip}} R_{ip}(1-R_{ip})\Big[R_{ip}\vec{s}.\vec{s} + (1-R_{ip})\vec{s}.\vec{s}\Big] + O(\delta^3) \tag{B-10}$$

or

$$\varphi_{R_{ip}} = (1-R_{ip})\varphi_P + R_{ip}\varphi_{nb} \\ -\frac{1}{2}\nabla\nabla\varphi\Big|_{R_{ip}} R_{ip}(1-R_{ip}) : \vec{s}.\vec{s} + O(\delta^3) \tag{B-11}$$

In this work we have taken R_{ip} such that $\vec{s}.\Delta\vec{R}_{ip} = 0$ to minimize the size of the explicit correction:

$$\vec{s}\bullet\Big[\vec{x}_{ip} - \left(\vec{x}_p + R_{ip}\vec{s}\right)\Big] = 0, \\ R_{ip} = \frac{1}{\left|\vec{s}\right|^2}\left(\vec{x}_{ip} - \vec{x}_p\right).\vec{s} \tag{B-12}$$

Now we can extrapolate this to the integration point:

$$\varphi_{ip} = \varphi_{R_{ip}} + \underbrace{\nabla\varphi\Big|_{R_{ip}}}_{o(\delta^2)}.\Delta R_{ip} + \frac{1}{2}\underbrace{\nabla\nabla\varphi\Big|_{R_{ip}}}_{o(\delta)}\Delta R_{ip}.\Delta R_{ip} + O(\delta^3) = \\ (1-R_{ip})\varphi_P + R_{ip}\varphi_{nb} - \frac{1}{2}\nabla\nabla\varphi\Big|_{R_{ip}} R_{ip}(1-R_{ip}) : \vec{s}.\vec{s} + \\ \Big[(1-R_{ip})\nabla\varphi\Big|_P + R_{ip}\nabla\varphi\Big|_{nb} + \Delta R_{ip}\Big[(1-R_{ip})\nabla\nabla\varphi\Big|_P + R_{ip}\nabla\nabla\varphi\Big|_{nb}\Big]\Big]\Delta R_{ip} \\ +\frac{1}{2}\Delta R_{ip}.\Delta R_{ip}\Big[(1-R_{ip})\nabla\nabla\varphi\Big|_P + R_{ip}\nabla\nabla\varphi\Big|_{nb}\Big] \tag{B-13}$$

knowing that $\nabla\nabla\varphi\Big|_P = \nabla\nabla\varphi\Big|_{nb} + O(\delta)$ then

$$\begin{aligned}\varphi_{ip} &= (1-R_{ip})\varphi_{P} + R_{ip}\varphi_{nb} \\ &-\frac{1}{2}\left[(1-R_{ip})\nabla\nabla\varphi\big|_{P} + R_{ip}\nabla\nabla\varphi\big|_{nb}\right]R_{ip}(1-R_{ip}) : \vec{s}.\vec{s} \\ &+\left[(1-R_{ip})\nabla\varphi\big|_{P} + R_{ip}\nabla\varphi\big|_{nb}\right]\Delta R_{ip} + \frac{1}{2}\Delta R_{ip}.\Delta R_{ip}\left[(1-R_{ip})\nabla\nabla\varphi\big|_{P} + R_{ip}\nabla\nabla\varphi\big|_{nb}\right]\end{aligned} \qquad \text{(B-14)}$$

$$\begin{aligned}\varphi_{ip} &= (1-R_{ip})\varphi_{P} + R_{ip}\varphi_{nb} + \Delta R_{ip}\left[(1-R_{ip})\nabla\varphi\big|_{P} + R_{ip}\nabla\varphi\big|_{nb}\right] \\ &+\left[(1-R_{ip})\nabla\nabla\varphi\big|_{P} + R_{ip}\nabla\nabla\varphi\big|_{nb}\right] : \frac{1}{2}\left[\Delta R_{ip}.\Delta R_{ip} - (1-R_{ip})R_{ip}\vec{s}.\vec{s}\right]\end{aligned} \qquad \text{(B-15)}$$

To complete a linear system representing the gradient and hessian requires evaluating the hessian at the cell-centre and gradient at the integration point. Using the simplified form of Eq. (B-5) and Eq. (B-15) yields to:

$$\nabla\nabla\varphi\big|_{P} = \frac{1}{V_{p}}\sum_{ip}\nabla\varphi\big|_{ip}A_{ip}\hat{n} \qquad \text{(B-16)}$$

$$\nabla\varphi\big|_{ip} = (1-R_{ip})\nabla\varphi_{P} + R_{ip}\nabla\varphi_{nb} + \Delta R_{ip}\left[(1-R_{ip})\nabla\varphi\big|_{P} + R_{ip}\nabla\varphi\big|_{nb}\right] \qquad \text{(B-17)}$$

It is worth mentioning that it was found that, in this particular work, using lower order accuracy also leads to a fairly accurate result.

The interpolation must be implemented implicitly and the order of accuracy should be improved, if necessary, with explicit deferred-corrections.

Dependency of a term on the cell-centred values guarantees its implicit implementation. Direct substitution of Eq. (B-17) into Eq. (2-57) would result in a purely explicit formulation and may result in numerical instability. Thus, the diffusion term should be treated more carefully so it can be considered implicitly and also not impairing the accuracy of the diffusion term. An implicit correction in the integration point gradients is used to approximate the diffusion term. More specifically:

$$\nabla\varphi\big|_{ip}^{m} \approx \overline{\nabla\varphi}\big|_{ip}^{m-1} + \frac{1}{\vec{s}.\hat{n}_{ip}}\left[\left(\varphi_{nb}^{m} - \varphi_{p}^{m}\right) - \frac{1}{2}\left(\nabla\varphi\big|_{p}^{m-1} + \nabla\varphi\big|_{nb}^{m-1}\right)\bullet\vec{s}\right]\hat{n}_{ip} \qquad \text{(B-18)}$$

where $\overline{\nabla\varphi}\Big|_{ip}^{m-1}$ is calculated using Eq. (B-17) at the previous iteration, $m-1$.

Gradient at the Boundary Node

At the boundary nodes, the node and integration points coincid and if it is assumed that the domain boundary is a Robin boundary condition, then, the general form of the equation is given as:

$$a\frac{\partial\varphi}{\partial n}\Big|_{bnd}+b\varphi_{bnd}+c=0 \tag{B-19}$$

in which a, b and c are constants. To develop an approximation for the normal component of the gradient at the boundary node, consider Figure (0-1) as a boundary control volume. Point P' is the intersection of the continuation of normal to the boundary face at the integration point and the perpendicular line that is drawn from cell centre is defined as below:

$$\overrightarrow{PP'}=\vec{s}-\vec{s}.\hat{n} \tag{B-20}$$

Using Taylor's series for field variable along the line that connects P' to the integration point results:

$$\frac{\partial\varphi}{\partial n}\Big|_{ip,bnd}=\frac{\varphi_{ip}-\varphi_{P'}}{\vec{s}.\hat{n}} \tag{B-21}$$

Also:

$$\varphi_{P'}=\varphi_P+\nabla\varphi\Big|_P.\overrightarrow{PP'} \tag{B-22}$$

Substituting back into Eq. (B-21):

$$\frac{\partial\varphi}{\partial n}\Big|_{bnd}=\frac{\varphi_{bnd}-\left[\varphi_P+\nabla\varphi\Big|_P.\left(\vec{s}-\vec{s}.\hat{n}\right)\right]}{\vec{s}.\hat{n}} \tag{B-23}$$

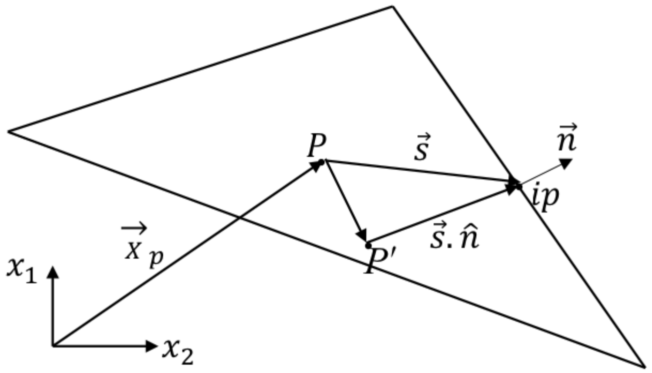

Figure 0-1: The incorrect velocity field adjacent to an interface

Gradient Reconstruction

To approximate gradient at the integration point, gradient at the centre of control volume is required. Here the idea that has been used in reference [39] of chapter 2 is simplified and explained for the purpose of clarification for a first order approximation only.

Using Taylor's series expansion for any field variable:

$$\varphi_{nb} = \varphi_P + \vec{s}\nabla\varphi\Big|_P \tag{B-24}$$

For directional derivative of gradient at the centre of control volume:

$$\hat{s}_i.\nabla\varphi\Big|_P = \frac{\varphi_{nb} - \varphi_P}{\left|\vec{s}_i\right|} \tag{B-25}$$

in which $\hat{s}_i = \frac{\vec{s}_i}{\left|\vec{s}_i\right|}$.

So, a linear system for the gradient at the cell-centered node P may be written in the form:

$$A_P.\nabla\varphi\Big|_P = b_P \tag{B-26}$$

For control volumes that have more than three faces the above system is overdetermind for Hessian calculation and generally there is no exact solution. However, least square gives the closest solution. Then,

$$A_P^T A_P . \nabla \varphi \Big|_P = A_P^T b_P \qquad \text{(B-27)}$$

Because A_P depend only on the geometry, for a fixed grid the $\left(A_P^T A_P\right)^{-1}$ must be found only once.

Appendix C: Case Study For the Result of Pressure Correction

Simulating a flow problem without considering special treatment for the interface yields unreasonable results, Fig. (0-2).

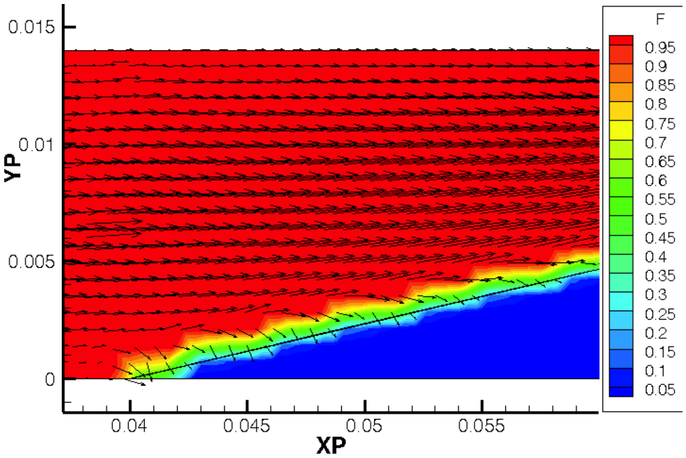

Figure 0-2:The incorrect velocity field adjacent to an interface

To remove all “spurious currents” resulting from the jump condition, at the interface between solid-liquid-mushy, special care is taken in obtaining approximations for pressure and pressure gradient.

To demonstrate the effect of proposed correction, a rectangular geometry with the dimension of 0.014 by 0.07 (m) filled with triangular mesh is chosen.

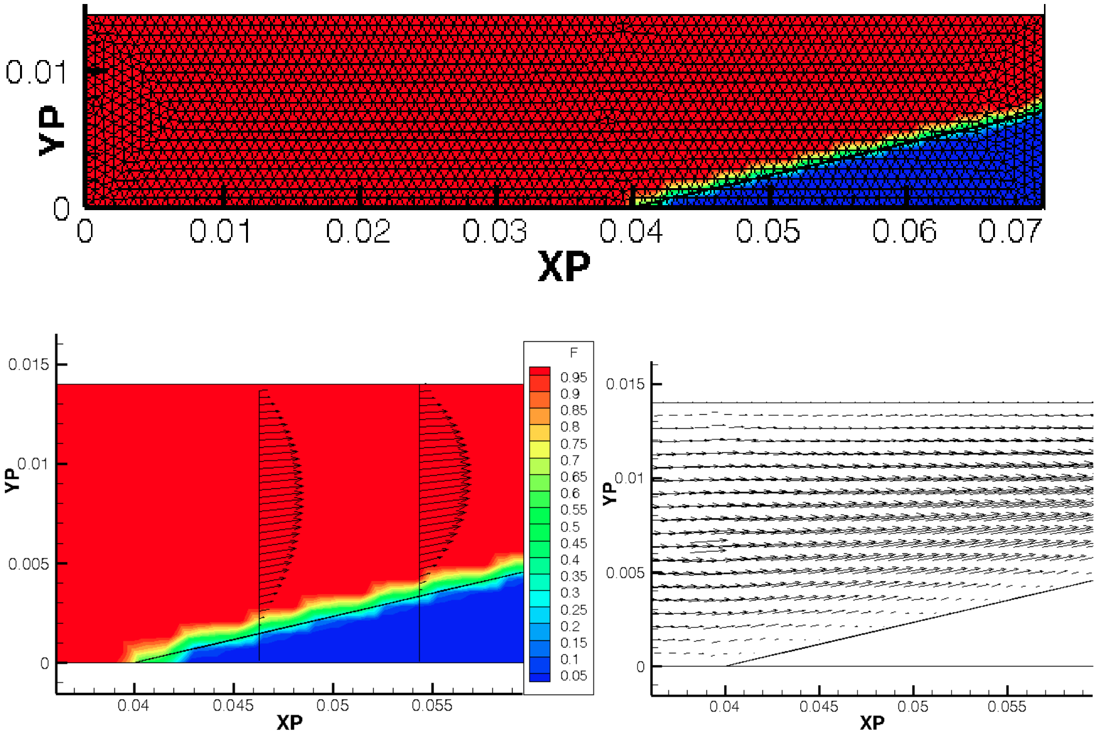

Figure 0-3: ***(Top): mesh, (Bottom): Results adjacent to the interface***

A pre-defined inclined interface is drawn in the lower right corner of this geometry and a fully developed flow of water is imposed as the boundary condition at the inlet (left). As the interface cuts through C.Vs, it creates C.Vs that are partially liquid and partially solid. Adjacent to these C.Vs pure liquid and solid exist. The mesh and result of this study is illustrated in (Fig. 0-3). It is interesting to note that the velocity vectors in the vicinity of the interface are turning from the interface due to the pressure correction. Overall, the result of this simulation is quite reasonable.

Appendix D: Coefficient Matrices for Conservation Equations

Since this work deals with the two-dimensional cases the coefficient matrices for the coupled mass-momentum equations have a dimension of 3X3 and each element of the matrix corresponds to the discretized terms of the governing equations:

$$\begin{array}{r} Mass \rightarrow \\ x-Mom \rightarrow \\ y-Mom \rightarrow \end{array}\left(\begin{array}{ccc} \overbrace{AUP_{1\times1}}^{\Pr essure} & \overbrace{AUP_{1\times2}}^{x-velocity} & \overbrace{AUP_{1\times3}}^{y-velocity} \\ AUP_{2\times1} & AUP_{2\times2} & AUP_{2\times3} \\ AUP_{3\times1} & AUP_{3\times2} & AUP_{3\times3} \end{array}\right)\begin{pmatrix} P \\ u \\ v \end{pmatrix} =$$

$$\begin{pmatrix} AUNB_{1\times1} & AUNB_{1\times2} & AUNB_{1\times3} \\ AUNB_{2\times1} & AUNB_{2\times2} & AUNB_{2\times3} \\ AUP_{3\times1} & AUNB_{3\times2} & AUNB_{3\times3} \end{pmatrix}\begin{pmatrix} P \\ u \\ v \end{pmatrix} + \begin{pmatrix} Bu_{1\times1} \\ Bu_{1\times1} \\ Bu_{1\times1} \end{pmatrix} \qquad \text{(D-1)}$$

in which,

$$\begin{aligned} AUP_{1\times1} &= -\hat{d}_{ip} \times \frac{1}{\vec{s}.\hat{n}_{ip}} \rho A_{ip} \\ AUP_{1\times2,1\times3} &= -(1-R_{ip})\rho A_{ip}.\hat{n}_{ip} \\ AUP_{2\times2,3\times3} &= \frac{\rho V_P}{\Delta t} - \sum\nolimits_{ip}^{n_{ip}} \frac{\dot{m}_{ip}}{f_l}\left(\frac{1-\alpha}{2}\right) + \sum\nolimits_{ip}^{n_{ip}} \frac{\mu_l}{\vec{s}.\hat{n}_{ip}} A_{ip}\hat{n}_{ip} + \frac{f_l \mu_l}{K} V_P \\ AUP_{2\times1,3\times1} &= (1-R_{ip})\left\langle P_l \right\rangle_P^l f_l A_{ip}\hat{n}_{ip} \\ AUP_{2\times3,3\times2} &= 0 \end{aligned} \qquad \text{(D-2)}$$

and,

$$\begin{aligned} AUNB_{1\times1} &= -\hat{d}_{ip} \times \frac{1}{\vec{s}.\hat{n}_{ip}} \rho A_{ip} \\ AUNB_{2\times2,3\times3} &= -\sum\nolimits_{ip}^{n_{ip}} \frac{\dot{m}_{ip}}{f_l}\left(\frac{1-\alpha}{2}\right) + \sum\nolimits_{ip}^{n_{ip}} \frac{\mu_l}{\vec{s}.\hat{n}_{ip}} A_{ip}\hat{n}_{ip} \\ AUNB_{2\times1,3\times1} &= -R_{ip}\left\langle P_l \right\rangle_{nb}^l f_l A_{ip}\hat{n}_{ip} \\ AUNB_{1\times2,1\times3} &= R_{ip}\rho A_{ip}.\hat{n}_{ip} \end{aligned} \qquad \text{(D-3)}$$

$$
\begin{aligned}
Bu_{1\times1} &= \left[\overline{\left\langle v_l \right\rangle}_{ip} - \left((1-R_{ip})\left\langle \vec{v}_l \right\rangle_P + R_{ip}\left\langle \vec{v}_l \right\rangle_{nb}\right)\right]\rho A_{ip}.\hat{n}_{ip} + \\
&\quad \hat{d}_{ip} \times \frac{\frac{1}{2}\left(\nabla\left\langle P_l \right\rangle^l\Big|_P + \nabla\left\langle P_l \right\rangle^l\Big|_{nb}\right).\vec{s}}{\vec{s}.\hat{n}_{ip}} + \\
Bu_{2\times1} &= \left[\frac{\rho V_P}{\Delta t}\left\langle \vec{v}_l \right\rangle_P\right]^{old} + f_l A_{ip}\hat{n}_{ip}\left[(1-R_{ip})\nabla f_l\Big|_P + R_{ip}\nabla f_l\Big|_{nb}\right].\Delta\vec{R}_{ip} + \\
&\quad DCDiff - DCConv \\
Bu_{3\times1} &= \left[\frac{\rho V_P}{\Delta t}\left\langle \vec{v}_l \right\rangle_P\right]^{old} + f_l A_{ip}\hat{n}_{ip}\left[(1-R_{ip})\nabla f_l\Big|_P + R_{ip}\nabla f_l\Big|_{nb}\right].\Delta\vec{R}_{ip} + \\
&\quad DCDiff - DCConv + Bouss.
\end{aligned}
\tag{D-4}
$$

For the energy equation the coefficients can be written as:

$$
\begin{aligned}
ATP &= \frac{\rho Cp_m V_P}{\Delta t} - \sum_{ip}^{n_{ip}} \dot{m}_{ip} Cp_l \left(\frac{1-\alpha}{2}\right) + \\
&\quad \sum_{ip}^{n_{ip}} \frac{k_m}{\vec{s}.\hat{n}_{ip}} A_{ip}\hat{n}_{ip} + \frac{\delta H_P V_P}{\Delta t}\left(\frac{dF}{dT}\Big|_{f_P^m}\right) \\
ATNB &= -\sum_{ip}^{n_{ip}} \dot{m}_{ip} Cp_l \left(\frac{1-\alpha}{2}\right) + \sum_{ip}^{n_{ip}} \frac{k_m}{\vec{s}.\hat{n}_{ip}} A_{ip}\hat{n}_{ip} \\
BT &= \frac{\delta H_P V_P}{\Delta t}\left[\left(f_P^{old} - f_P^m\right) + \frac{dF}{dT}\Big|_{f_P^m} \times F^{-1}\left(f_P^m\right)\right] + \\
&\quad \left[\frac{\rho Cp_m V_P}{\Delta t}\left\langle T \right\rangle_P\right]^{old} + DCDiff - DCConv
\end{aligned}
\tag{D-5}
$$

Curriculum Vitae

Name:	Mehdi Farrokhnejad
Post-secondary Education and Degrees:	Iran University of Science & Technology Iran 1999-2003 B.Eng. The University of Western Ontario London, Ontario, Canada 2007-2009 M.E.Sc The University of Western Ontario London, Ontario, Canada 2009-2013 Ph.D.
Honours and Awards:	Queen Elizabeth II Graduate Scholarship (QEII) 2010-2011 Ontario Graduate Scholarship (OGS) 2011-2012 Province of Ontario Graduate Scholarship (OGS) 2012-2013
Related Work Experience	Teaching Assistant The University of Western Ontario 2007-2013

Publications:

Farrokhnejad Mehdi, Straatman Anthony G., Wood Jeffrey T. (2013). A volume averaged finite-volume model for solidification of magnesium alloys on a general unstructured colocated grid. Accepted in Numerical Heat and Mass Transfer Part A: Application, August 2013

Farrokhnejad Mehdi, Straatman Anthony G., Wood Jeffrey T. (2013). Numerical simulation of solidification and prediction of mechanical properties in magnesium alloy, Submitted to Metallurgical and Materials Transactions B, July 2013

Farrokhnejad Mehdi, Straatman Anthony G., Wood Jeffrey T. (2013) A Finite-Volume Model For Numerical Solidification of Mg Alloys, Materials Science Forum 765, 281-285

Farrokhnejad Mehdi, Straatman Anthony G. (2012) Advances on a VOF Based Numerical Simulation of Mg Die-Casting Process on a General Unstructured Grid. Mg Alloys and Their Applications

Farrokhnejad Mehdi, Straatman Anthony G., Wood Jeffrey T. (2009), A Volume-of-Fluid Based Numerical Simulation of Solidification in Binary Alloys on Fixed Non-uniform Co-located Grids, ASME International Manufacturing Science and Engineering vol. (1) pp. 427-436, 2009